Theoretically probing structural and electronic properties of Pr-based crystals for energy applications

Francisca Queirós
Master in Physics
Department of Physics and Astronomy
Faculty of Sciences of the University of Porto
2024

Theoretically probing structural and electronic properties of Pr-based crystals for energy applications

Francisca Queirós

Dissertation carried out as part of the Master in Physics

Department of Physics and Astronomy

2024

Supervisor
Estelina Silva, Researcher, Faculty of Sciences of the University of Porto

Co-supervisor
Vitor Pereira, Associate professor, Faculty of Sciences of the University of Porto

Acknowledgements

Regarding the numerical portion of this thesis, I am very grateful to the computational facilities and I would like to acknowledge the funding from FCT through the PTDC/EME-REN/1497/2021 project (Power Phoenix Battery-A Full Solid State Grid-scale Storage Solution), the CEEC individual fellowship 5th edition with Reference 2022.00082. CEECIND, and IFIMUP with projects UIDB/04968/2020 (https://doi.org/10.54499/UIDB/04968/2020) and UIDP/04968/2020 (https://doi.org/10.54499/UIDP/04968/2020); and the High Performance Computing Chair - a R&D infrastructure (based at the University of Évora; PI: M. Avillez), endorsed by Hewlett Packard Enterprise, and involving a consortium of higher education institutions, research centers, enterprises, and public/private organizations. Computational resources are acknowledged through the 2022.15832.CPCA.A2 project at University of Évora – Oblivion.

Resumo

Células de Combustível de Óxido Sólido têm sido um foco de pesquisa e investigação para aplicações em armazenamento de energia, pois conseguem eficazmente converter energia química diretamente em eletricidade através da oxidação de combustíveis tal como H_2 ou mesmo hidrocarbonetos, e além disso, fazem-no com o mínimo de poluição. A funcionalidade requerida para a operação das SOFCs depende da mesma propriedade exigida para o armazenamento eficiente de oxigênio: óxidos em estado sólido capazes de capturar, libertar e transportar oxigênio de maneira controlada. Tecnicamente, o cátodo é uma componente functional crítica cujas caracterísitcas determinam a eficácia, a capacidade cíclica e, ao fim e ao cabo, a viabilidade tecnológica do conceito das células de combustível de óxido sólido. Compostos de cátodos baseados em sulfatos de óxido com a capacidade de armazenar oxigénio são um conceito atrativo exatamente por essa razão.

Um caso específico de interesse, está, ultimamente a ser ativamente estudado por experimentalistas, que exploram o potencial e as vantagens do uso de oxisulfatos/oxisulfitos contendo praseodímio $Pr_2O_2SO_4$/Pr_2O_2S como um composto de cátodo de células de combustível de óxido sólido. Esta dissertação aborda esta mesma questão, mas de uma perspetiva teórica, fornecendo resultados estruturais, eletrónicos, magnéticos e algumas características químicas dos dois compostos $Pr_2O_2SO_4$ e Pr_2O_2S, que são conhecidos no presente. Os cálculos são baseados em teorias do Funcional da Densidade, implementada no software open-source gratuito, Quatum Espresso (QE). Visto que o óxido utilizado inclui o lantanídeo Pr (um elemento pesado com orbitais f desocupadas e fortemente localizadas), é necessário ter mais atenção para o grau de impacto que estas correlações têm na natureza do seu estado fundamental. Para alcançar isto, nós realizamos cálculos de teoria do Funcional da Densidade usando os convencionais funcionais de troca e de correlação, tal como as correções de Hubbard.

Concluímos que, dentro do conjunto de estruturas consideradas, $Pr_2O_2SO_4$ totalmente relaxado, tem como espaço de grupo de simetria o $C2/c$ (#15), que pertence ao sistema cristalino monoclínico; Pr_2O_2S apresenta o espaço de grupo de simetria $P\bar{3}m1$ (#164), que pertence ao sistema cristalino trigonal. Os nossos resultados estabeleceram que o efeito das interações de Coulomb entre os eletrões f é forte. Isto é revelado, por um lado, pelo valor do parâmetro de interação de hubbard obtido de forma auto-consistente ($U \simeq 2.1013$ eV); por outro lado, os efeitos são também evidentes na estrutura de banda, de natureza

semicondutora, com amplitudes de largura de banda e polarizações de spin que são previsto com e sem ter em conta as correções de correlação. Particularmente, estas correlações ultimamente determinam o carácter magnéico do sistema, que encontramos como sendo um antiferromagnético de tipo A com uma energia da banda de viragem do spin de 2.67 eV. A análise de Bader da distribuição de Bader permite-nos concluir que os estados de oxidação do $Pr_2O_2SO_4$ é igual a 4+ e do Pr_2O_2S é de 3+. No entanto, ainda se observa algumas diferenças entre os valores esperados e os nossos resultados devido à natureza covalente das ligações.

Em adição aos resultados originais que permitem a primeira caracterização ab-initio deste par de óxidos, os resultados desta dissertação contribuem também para informar os experimentalistas que têm um trabalho relacionado, interpretar as próximas medições, tal como propor novas funcionalidades e potenciais aplicações baseadas nos nossos resultados: por exemplo, explorar o estado magnético como um parâmetro experimental para otimizar e expandir as aplicações das células de combustível de óxido sólido. **Palavras-chave**: Óxido de Praseodímio, Teoria do Funcional da Densidade, DFT com Hubbard, óxidos magnéticos, armazenamento de oxigénio, células de combistível de óxido sólido, Quantum Espresso

Abstract

Solid Oxide Fuel Cells (SOFCs) are a subject of intense research for applications in energy storage, for they can efficiently convert chemical energy directly to electricity by oxidation of fuels such as H_2 or even hydrocarbons, with minimum pollution and silently. The requisite functionality for the operation of SOFCs relies on the same property demanded for efficient oxygen storage: solid-state oxides amenable to controlled, on-demand capture, release and transport of oxygen. Technically, the cathode is a critical functional component whose characteristics determine the efficiency, cyclability and ultimately the technological viability of a given SOFC concept. Composite cathodes based on oxysulphate oxygen-storage materials are an appealing concept in this regard.

A specific case of interest is being actively explored at this moment by experimental collaborators, who are probing the potential and advantages of using the Pr-based oxysulfate/oxysulfide pair $Pr_2O_2SO_4$/Pr_2O_2S in the composite cathode of SOFCs. This dissertation tackles the same questions from the theoretical perspective, providing results for the structural, electronic, magnetic and some chemical characteristics of the two compounds Pr2O2SO4 and Pr2O2S, which are presently unknown. The calculations are based on Density Functional Theory (DFT), as implemented in the free, open-source Quantum Espresso (QE) software suite. Since our target oxide includes the lanthanoid Pr (a heavy element with unfilled, tightly localized f orbitals), special care must be taken in the DFT implementation to assess the degree to which correlations impact the nature of the ground state. To address this, we perform DFT calculations with conventional exchange-correlation functionals, as well as Hubbard-corrected DFT (DFT+U).

We find that, among the subset of structures considered, fully relaxed $Pr_2O_2SO_4$ has the space group symmetry $C2/c$ (#15), which belongs to the monoclinic crystal system; the counterpart Pr_2O_2S has the space group symmetry $P\bar{3}m1$ (#164), which belongs to the trigonal crystal system. Our results establish that the effect of Coulomb interactions among f-electrons is strong. This is revealed, on the one hand, by the value obtained self-consistently for the Hubbard interaction parameter ($U \simeq 2.1013$ eV); on the other hand, the effects are also evident in the bandstructure, semiconducting nature, bandgap magnitudes and spin polarization that are predicted with and without accounting for correlation corrections. Most notably, these correlations ultimately determine the magnetic character of the system, which we find to be a robust A-type antiferromagnet with a spin-flip energy gap of 2.67 eV. A Bader analysis of the charge distribution allows us to conclude that the

oxidation state of $Pr_2O_2SO_4$ is equal to 4+ and of Pr_2O_2S is of 3+. However, there is still some differences between the results and the results expected because of the covalent nature of the bonds .

In addition to original results that allow the first ab-initio characterization of this pair of oxides, the work in this dissertation contributes to inform the related experimental work under way, interpret the forthcoming measurements, as well as propose new functionalities and potential applications based on our results: namely exploiting the underlying magnetic state as a new experimental handle to tune and/or expand their functionality in SOFC applications.

Keywords: Praseodymium oxides, density functional theory, Hubbard-corrected DFT, magnetic oxides, oxygen storage, solid oxide fuel cells, Quantum Espresso.

Table of Contents

List of Abbreviations **xi**

1 Introduction **1**

1.1 Fuel cells and oxygen storage 2
1.2 Materials challenges for SOFC engineering 3
1.3 The candidate oxide Pr2O2SO4 5
1.4 Theoretically modeling interacting electrons and nuclei 8
1.5 Objectives of this dissertation and thesis outline 11

2 Theoretical methods **12**

2.1 Density Functional Theory 12
2.1.1 The variational principle for the density 12
2.1.2 The Hohenberg-Kohn theorem 13
2.1.3 The Kohn-Sham equations 14
2.1.4 Local Density Approximation and Generalized Gradient Approximation 16
2.1.5 Advantages and Disadvantages 17
2.2 Hubbard-extended DFT 18
2.2.1 Extended DFT+U+V with on-site and intersite electronic interactions 20
2.2.2 Hubbard projectors 24
2.2.3 Computing U from linear-response 25
2.2.4 Hubbard parameters from DFPT 27
2.2.5 From localized perturbations in supercells to monochromatic perturbations in primitive unit cells 30
2.2.6 Monochromatic perturbations in DFPT 31
2.2.6.1 Other methods 33
2.3 Structural, electronic and magnetic properties 33
2.3.1 Magnetic Properties of Pr2O2SO4 33
2.3.2 Bader charge analysis 35

3 Computational Implementation **37**
3.1 The Quantum Espresso software 37
3.2 Computational Details 39
3.2.1 Cell parameters 40
3.2.2 Metal and Insulator Systems 40
3.2.3 Geometry and Structural Relaxation 42
3.2.4 Non-Self-Consistent Field Calculation 43
3.2.5 Hubbard parameters 43

4 Results **47**
4.1 Structural parameters and energetical stability 47
4.2 Band Structure and Density of States of Pr2O2SO4 49
4.3 Bader Charge Analysis 55
4.4 Reaction between oxysulfate/oxysulfide 56
4.5 Discussion of some results 56

5 Conclusion **58**
5.1 Future work 59

Bibliography **59**

A Coulomb interaction regularization **69**
A.1 Construction of the second-quantized hamiltonian 70

B DFT+U calculation using pw.x **73**

C Birch Murnaghan's equation of state **76**

List of Tables

4.1 Atomic positions grouped by Wyckoff positions of $Pr_2O_2SO_4$ with the monoclinic structure, $C2/c$ (#15). Coordinates are dimensionless, given in terms of the conventional unit cell defined in International Tables of Crystallography 48

4.2 Atomic positions grouped by Wyckoff position of Pr_2O_2S with the trigonal structure, $P\bar{3}m1$ (#164). Coordinates are dimensionless, given in terms of the conventional unit cell defined in International Tables of Crystallography. .48
4.3 Lattice parameters (a, b, c) and volume (V), from the DFT-PBE and DFT-PBE+U calculations, both for the monoclinic (^{M}) and tetragonal(^{T}) structures of $Pr_2O_2SO_4$, and for the trigonal structure ^{P} of Pr_2O_2S. Comparison with experimental results are shown for the lattice parameters for the different systems. 49
4.4 Magnetic Moment (MM) per site (integrated at the atomic sphere of radius, R, computed using DFT) for the ferromagnetic ordering of the monoclinic structure $C2/c$ (#15). 54
4.5 Relative energy, in units of eV, between the different antiferromagnetic ordering of $Pr_2O_2SO_4$ for the $C2/c$ structural compound, when employinh DFT+U=2.1013 eV. 54

List of Figures

1.1 Crystal structure of the $Pr_2O_2SO_4$ and Pr_2O_2S. This figure has been taken from Ref [4]. 7
1.2 Crystal structure of $Pr_2O_2SO_4$ and Pr_2O_2S. The figures were reproduced with the VESTA visualization software [20]. The large yellow spheres represent praseodymium (Pr), the small yellow sulphur (S) and red represents the oxygen (O) atoms. 8

2.1 Sketch of the total energy profile as a function of the number of electrons in a generic atomic system in contact with a reservoir. The bottom curve is simply the difference between the other two (the LDA energy and the "exact" result for an open system). This figure has been taken from Ref. [37]. 27
2.2 Three types of antiferromagnetic (AF) structures, A- AF, C- AF, and G-AF. 35

3.1 Comparison of the density of states of TiNiSn calculated via the tetrahedron method using a $21 \times 21 \times 21$ **k**-point mesh (red) and the Gaussian smearing method with $3 \times 3 \times 3$(orange) and $21 \times 21 \times 21$(blue) **k**-point meshes. The smearing width is set to 0.05 eV for calculations using Gaussian smearing methods. This figure has been adapted from Ref. [76] 42
3.2 Flowchart of the process of computing the valued of the Hubbard parameter U adn V self-consistently. 46
3.3 Convergence of the Hubbard parameter U during the self-consistent evaluation from DFPT calculations based on DFT+U. All calculations are based on a basis set of orthogonalized atomic orbitals for the Hubbard manifold. 46

4.1 DFT electronic band structure (top) and PDOS (bottom) (without including the Hubbard term) for the monoclinic structure $C2/c$ (#15) of $Pr_2O_2SO_4$ for the ferromagnetic order. 49
4.2 DFT electronic band structure and total DOS (top) and PDOS (bottom) (without the Hubbard term) for the tetragonal structure $I\bar{4}2m$ (#121) of $Pr_2O_2SO_4$. 50
4.3 DFT electronic PDOS (bottom) (without considering the Hubbard term) for the trigonal structure $P\bar{3}m1$ (#164) of Pr_2O_2S. 50
4.4 DFT electronic and structure and DOS (top) and PDOS (bottom) with the Hubbard term equal to 2.1013 eV for the monoclinic structure $C2/c$ (#15) of $Pr_2O_2SO_4$. 51
4.5 DFT electronic PDOS with the Hubbard term equal to 2.1013 eV for the tetragonal structure $I\bar{4}2m$ (#121) of $Pr_2O_2SO_4$. 52
4.6 DFT electronic band structure and DOS (top) and PDOS (bottom) with the Hubbard term equal to 2.1013 eV for the trigonal structure $P\bar{3}m1$ (#164) of Pr_2O_2S. 52
4.7 DFT electronic band structure and DOS (top) and PDOS (bottom) with the Hubbard term equal to 4.0 eV for the monoclinic structure $C2/c$ (#15) of Pr_2O_2S. 53
4.8 DFT electronic band structure and DOS (top) and PDOS (bottom) with the Hubbard term equal to 4.0 eV for the trigonal structure $P\bar{3}m1$ (#164) of Pr_2O_2S. 53

4.9 DFT+U electronic band structure and DOS (top) and PDOS (bottom) of the monoclinic structure $C2/c$ (#15) of $Pr_2O_2SO_4$, by considering the antiferromagnetic ordering of A-type. 55

C.1 Relation between the energy of the tetragonal structure, $I\overline{4}2m$ (#121) of $Pr_2O_2SO_4$ and the respective volume obtained using the function ev .x from QE that fits our values to a Birch Murnagham equation of state in order to obtain the volume that minimizes the energy. 77

List of Abbreviations

AF antiferromagnetic.

BZ Brillouin Zone.

DFPT Density functional perturbation theory.

DFT Density Functional Theory.

DOS density of states.

EOS Equation of State.

F ferromagnetic.

FLL “fully localized limit”.

GGA generalized gradient approximation.

HF Hartree-Fock.

HTFCs High-temperature fuel cells.

KS Kohn-Sham.

LDA local density approximation.

LR linear-response.

NSCF non-self-consistent field.

OSC oxygen storage capacity.

OSMs Oxygen Storage Materials.

PAW Projector augmented-wave.

PBE Perdew-Burke-Enzerhof.

PDOS Projected density of states.

QE Quantum Espresso.

SCF self consistent field.

SIE self-interaction errors.

SOC spin-orbit coupling.

SOFC Solid Oxid Fuel Cells.

TWC “three-way catalyst”.

xc exchange-correlation.

1. Introduction

This dissertation aims to theoretically study the structural, electronic and magnetic properties of the Pr-based crystal $Pr_2O_2SO_4$. The parent compound of the oxysulfate/oxysulfide pair $Pr_2O_2SO_4$/Pr_2O_2S, has recently attracted experimental interest for its potential as a high-quality cathode in solid-state fuel cells, but remains very much unexplored theoretically.

We will use first-principles techniques to compute and characterize the stable crystal structures and possible metastable polymorphs, because slight morphology differences can have critical impact in the structural and electronic properties, and therefore respective energy and storage-and-release performance for practical application. Another performance-determining factor are the oxidation states of the different elements within the crystal unit cell, since these influence the chemistry related to the oxygen capture, release and transport within the material. We will compute such features by analyzing the structural and electronic properties, which will be complemented with established techniques to obtain the real-space charge distribution within the unit cell.

Our calculations will be based on Density Functional Theory (DFT) as implemented in the Quantum Espresso (QE) software package. We will employ exchange-correlation (xc) functionals based on the generalized gradient approximation (GGA) within the Perdew-Burke-Enzerhof (PBE) scheme for DFT, and will also assess the effect of correlations in the form to the Hubbard U parameter, within a DFT+U scheme.

As a member of the lanthanoid series, Pr is a heavy element with unfilled f orbitals, which means that special care must be taken to assess possible magnetic ground-states, as well as effects of spin-orbit coupling (SOC). Since f orbitals are too strongly bound, Coulomb interactions are in-principle a concern that should be carefully investigated beyond the xc functional, because the latter captures interactions only in an effective way, known to often fail in predicting the character of the ground state in f-orbital systems. This is why, in addition to conventional DFT calculations, we have also performed DFT+U calculations, which add a Hubbard term to the density functional to better capture the strong correlations among the f-electrons of Pr. The goal here is, on the one hand, to assess the possibility of magnetic ground-states and, if so, how significant is the influence of such f-states in defining the nature of $Pr_2O_2SO_4$. On the other hand, if magnetism is present, it could

offer a route to externally tune (with magnetic fields) the oxygen storage parameters on-demand, opening a new functional capability to SOFCs and other oxygen-storage-based applications.

The detailed information about the structural, electronic and magnetic properties that we should obtain from these calculations will allow us to elucidate if this material is a good candidate for Solid Oxid Fuel Cells (SOFC) and oxygen storage, which, so far, has been suggested only on an empirical basis, while also giving us the opportunity to assess whether this material has other potential applications. Furthermore, our results will be of value to an ongoing collaboration with an experimental group at the University of Aveiro [Centro de Tecnologia Mecânica e Automação (TEMA)] that has been synthesizing and experimentally probing these and related classes of materials for SOFC applications. This type of synergy between experimental and theoretical work is essential to accelerate discovery, optimize parameters, and understand the physics underlying the intended functionality of this material.

1.1. Fuel cells and oxygen storage

There is an increasing concern over the provision of future energy and solutions for energy storage. Searching and developing alternative energy sources has both significant interest as well as environmental urgency. During the past years, various energy storage applications have been developed, such as: electrochemical energy storage including lead-acid, lithium-ion, sodium-sulphur; pumped storage; electromagnetic energy storage like superconducting energy storage; phase change energy storage including thermal and cold energy storage, etc. Among the promising candidates for future clean energy generation and storage are SOFC, which convert an oxide-based fuel to electricity and the reverse: store electrical energy back into oxide fuel. The central role for this functionality lies in so-called Oxygen Storage Materials (OSMs) which, as their name implies, can either capture or release oxygen on-demand, under well defined, reproducible and cyclable electrochemical conditions. This storage capability is the same that makes OSMs suitable for another well known application: as active materials in emission-control catalysts that reduce the emission of toxic pollutants resulting from engine exhaust gases. These two avenues of application fuel a current search for OSMs with the ability to capture (store) oxygen under an oxidizing atmosphere and release it under reducing conditions. For example, when used in emission-control catalysts, the OSMs regulates oxygen partial pressure whenever there are deviations from the desired stoichiometry of the exhaust

gas mixture, compensating for oscillations between poor (oxidizing) and rich (reducing) exhaust conditions that change momentarily, with the objective of converting NO_x, CO and hydrocarbons to less harmful compounds [1].

SOFCS are electrochemical conversion devices that can efficiently convert chemical energy directly into electricity, by oxidation of fuels such as H_2 or even hydrocarbons, with minimum pollution. They are characterized by the use of solid oxide electrolytes to transport oxygen anions from the cathode to the anode. The anode is where the electrochemical oxidation of the hydrogen, carbon monoxide or other organic intermediates formed through oxygen ions occurs:

$$H_2(g) + O^{2-}(g) \rightarrow H_2O(g) + 2e^- \tag{1.1}$$

The cathode is where an oxide material catalyses the reduction of oxygen:

$$1/2O_2(g) + 2e^- \rightarrow O^{2-}(g) \tag{1.2}$$

and facilitates the transport of the ionic species to the electrolyte [2].

Each individual cell provides a typical power of the order of 1 $W\,cm^{-2}$ and these can be combined to form fuel cell stacks, which size may be adjusted to achieve the required power output for the envisaged application (although such modularity has some trade-offs, like the need for metallic interconnections and an architecture compatible with providing fuel, air and current collection) [3]. This modularity opens a range of potential applications, such as stationary power for isolated areas with outputs from 100 W to 2 MW, public transportation power, auxiliary power units in vehicles and even portable power.

1.2. Materials challenges for SOFC engineering

One of the main challenges of SOFC is to find the best materials that provide the most efficient results. For the cathodes, there are several materials that have been studied, these include: composite materials consisting of $(ZrO_2)_{0.92}(Y_2O_3)_{0.08}$ a classical ionic conductor, and $La_{1-x}Sr_xMnO_{3-\delta}$ an electronic conductor; single phase mixed ionic and electronic conducting (MIECs) materials, such as $La_{0.6}Sr_{0.4}Co_{0.8}Fe_{0.2}O_{3-\delta}$(LSCF), $Sm_{0.5}Sr_{0.5}Co_{0.5}O_{3-\delta}$, and $Ba_{0.5}Sr_{0.5}Co_{0.2}Fe_{0.8}O_{3-\delta}$. There is also the combination of LSCF with $(ZrO_2)_x(Sc_2O_3)_{1-x}$, $La_{1-x}Sr_xGa_{1-y}Mg_yO_{3-(x+y)/2}$ or $(CeO_2)_{1-x}(GdO_{1.5})_x$. The success of these materials depends on several parameters. These should evidence high electronic and ionic kinetic behavior, high chemical compatibility between the materials of the cell, low instability, small polarization resistance and low cost of each component. They are also influenced

by the ratio between each composite (in MIECs), the microstructure and the working temperatures that are exposed [4]. Depending upon the operation temperature, either mixed conducting oxides, electronically conducting oxides or composite cathodes consisting of one ionic and one electronic conducting oxide are used.

High-temperature fuel cells (HTFCs), targeted at working temperatures around 800-1000°C, are promising due to their flexibility to a wide diversity and purity of fuels and the possibility to use affordable catalysts (substances that accelerate a chemical reaction, or reduce the required temperature and/or pressure to initiate a chemical reaction). Nonetheless, more recent work [5, 6] promotes a slight decrease in operation temperature to intermediate value ranges between (600-800°C), to enable a more rapid startup of the system and improve longevity of the devices and to make the overall SOFC technology more affordable, which is essential for the successful commercialization of SOFC technology. As operation temperatures are decreased, there is an associated increase in the specific area resistance, R_p, as a consequence of increased polarization resistance (R_p is defined as the resistance of the specimen to oxidation during the application of an external potential). The transport of the oxide ion and the gas transport also limit the cathode performance, because of the reduced electrolyte conductivity [4]. Hence, one of the key challenges in fuel cell research is the reduction of the cell overpotential in order to increase the efficiency of the system and thus lower costs [7]. The difference between the theoretical and the actual achieved cell voltage is due to irreversible losses: activation losses/polarization, fuel crossover and internal currents, ohmic losses and mass transport/concentration losses. To minimize all these factors, the choice of an appropriate electrode composition and microstructure become critical at intermediate temperatures to maximize the kinetics of the oxygen exchange and diffusion [2].

We will now provide an overview regarding the oxygen storage systems, and why these are important. CeO_2–ZrO_2 is an example of a sole component for the exhaust system applications due to its reversible and rapid release and sorption of oxygen at relatively low temperatures (less or equal to 400°C) [8]. Since the reaction is based on the redox between Ce^{4+} and Ce^{3+} and corresponding solid gas oxygen equilibrium, the oxygen storage capacity can therefore not exceed $0.25\,(\text{mol of } O_2).\text{mol}^{-1}$.

The emission control catalysts are primarily used to reduce harmful emissions from the fossil fuel run engines employed in the mobile/stationary sectors. Incomplete fuel combustion in gasoline engines generates toxic gases like CO, unburnt hydrocarbons and

NO_x composed of NO, NO_2 and N_2O. All these pollutants have harmful effects on the environment and human health. In gasoline engines, a "three-way catalyst" (TWC) is used to control the toxicity level of the emissions. High oxygen storage capacity (OSC) of the catalytic material usually ensures high conversion. The rare earth metal oxide, CeO_2, exhibits OSC properties due to its reversible redox capability. The redox conversion is carried out by the participation of the lattice oxygen and adsorbed active oxygen species present on the CeO_2 surface. During the redox process, oxygen vacancies are generated on the catalyst surface, which consequently act as the active centers for the next catalytic cycle. Thus, the ease of oxygen vacancy formation along with other factors, like the preparation/post-preparation treatment of the catalysts, presence of dopants or impurities, thermal treatment/ageing conditions, etc., strongly influence the OSC of CeO_2. To broaden and accelerate the industrial deployment of applications that exploit the mechanism of on-demand oxygen storage+release, a larger storage capacity per unit solid volume is highly desirable [9, 10].

1.3. The candidate oxide $Pr_2O_2SO_4$

Given the above motivation and background, the potential and urgency for applications, as well as the underlying challenges and desirable control of the material properties, this dissertation will theoretically explore the structural and electronic properties of a specific lanthanide oxysulfate/oxysulfide ($Ln_2O_2SO_4/Ln_2O_2S$) system, where Ln stands for an element of the Lanthanoid series (typically, Ln=La,Pr,Nd and Sm). This is the first example of oxygen storage that uses non-metallic elements as a redox site. We will concentrate, specifically, in three crystalline structural phases of $Pr_2O_2SO_4$, which relative stability will be assessed, and correspondingly its oxysulfide counterpart Pr_2O_2S.

The crystal $Pr_2O_2SO_4$ occurs as individual bladed crystals up to 0.4 mm long and elongated along the c axis. Crystals of $Pr_2O_2SO_4$ have two equally abundant morphologies, both tabular to the (010) crystallographic plane, however one type is terminated by a (011) prism, and the other by (101). Indices were obtained by goniometric measurements that characterize the angles of the crystals [11]. Mohs hardness is approximately $2^{1/2}$, and the crystals are brittle with a well developed (010) cleavage. There has been ongoing discussions regarding the space group that characterizes the most stable crystal structure. $Pr_2O_2SO_4$ should crystallize in the orthorhombic $Imm2$ (#44) space group (however, there has been no experimental evidence that such a phase exists) or $I222$(#23) (Fig. 1.2c) [11]. Another polymorph that $Pr_2O_2SO_4$ has shown to evidence is the $C2/c$(#15) , a monoclinic

space group symmetry (presented in Fig. 1.2a) , which has been referenced in literature (Refs. [4, 12]), and also theoretically screened and available in the Materials Project database [13]. For the present study, we have also considered the isostructural form to $Nd_2O_2SO_4$, which is the tetragonal $I\overline{4}2m$ (#121) form (Fig. 1.2b), in order to compare the energetic stabilities, since Nd has only an extra electron when compared to Pr. There had been stated a $I222$(#23) symmetry, where the unit-cell parameters (obtained through Weissenberg photographs using CuKα (1.54 Å) radiation) with estimated standard deviations in parentheses were of $a = 4.139(5)$ Å, $b = 4.243(5)$ Å, $c = 13.431(15)$ Å, resulting in a volume of $V = 235.87$ Å^3 [11]. However, and according to Ref. [12] a $C2/c$(#15) space group symmetry had been observed, where the lattice parameters were found to be $a = 8.281(1)$ Å, $b = 4.244(1)$ Å, $c = 14.046(1)$ Å.

In terms of the synthetization process of $Pr_2O_2SO_4$, this is possible when applying the surfactant-assisted synthesis of layered mesophases consisting of Pr hydroxide and dodecyl sulfate (DS = $C_{12}H_{25}OSO_3^-$) that, in fact, originates pores of 2-3 nm (small pores) in size and a large surface area of 28 m^2g^{-1}. Additionally, the Ln oxysulfate materials (Ln=La,Pr,Nd and Sm) have high specific surface area, uniform mesoporosity (molecular scaled pores) and redox ability of sulphur due to the microstructural modifications by means of template synthesis. The creation of pores to increase the specific surface is essential to reduce the redox temperature because it makes it easy for the gas diffusion and solid-gas reaction in the redox cycles. In terms of the dynamic redox behavior, the microstructure of $Pr_2O_2SO_4$ is very effective in accelerating the solid-gas reaction in oxygen release as well as storage processes, which enables working temperatures $\leq 600°$C, compared to $\geq 700°$C required for $Pr_2O_2SO_4$ prepared from $Pr_2(SO_4)_3$ [14]. Other than that, among Ln-based oxysulfates, the Pr system has the lowest operational temperature (around 600°C). Around this temperature, the additional redox couple between Pr^{3+} and Pr^{4+} at the surface promotes the redox of sulphur, facilitating Pr_2O_2S formation. This prevents the charge transfer and dissociative adsorption of oxygen on the electrode surface. Now, in terms of oxygen storage, the redox between $Ln_2O_2SO_4(S^{6+})$ and $Ln_2O_2S(S^{2-})$ achieve a oxygen storage capacity of 2 (mol of O_2)mol^{-1}, which is eight times larger that that of CeO_2-ZrO_2 [15–17].

Moreover it is important to pay attention to the structure of the material. $Pr_2O_2SO_4$ is associated with a structural distortion of an $(SO_4)^{2-}$unit. In oxidizing conditions, $Pr_2O_2SO_4$ is composed of alternative stacks of $Pr_2O_2^{2+}$ and SO_4^{2-} units (Fig. 1.1), while upon reduction, sulphur is reduced, with loss of oxygen from the sulphate layers. The structure in the

oxidizing conditions is similar to the one of Pr_2O_2S that also consists of stacking of $Pr_2O_2^{2+}$ but the latter with S^{2-} layers. The structural similarity would be one of the reasons for the reversible and stable redox cycles. Because $Pr_2O_2SO_4$ phases are stoichiometric and iso-

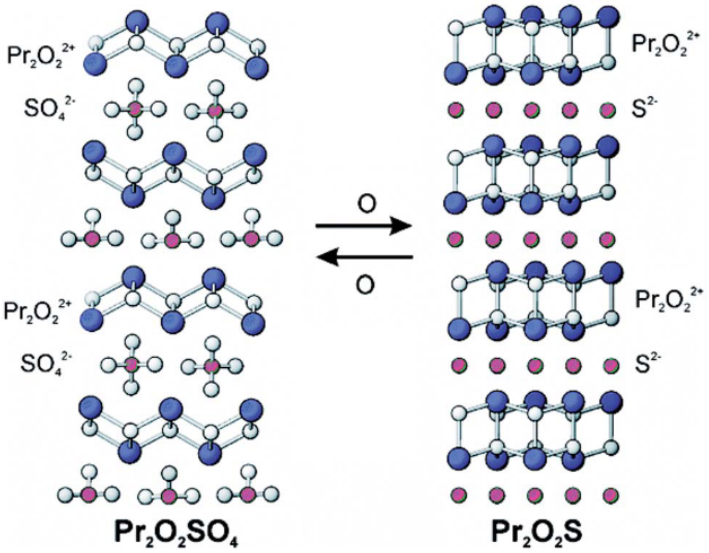

Figure 1.1: Crystal structure of the $Pr_2O_2SO_4$ and Pr_2O_2S. This figure has been taken from Ref [4].

morphous, the formal charge on Pr should commonly be 3+. Similarly, a series of Pr_2O_2S compounds should contain Pr in the 3+ oxidation state. However, as it can be seen in Pr 3d XPS spectra in the Ref. [12] Pr has peaks due to Pr $3d_{5/2}$ and Pr $3d_{3/2}$ for $Pr_2O_2SO_4$ that can be decomposed into two components, 953.8/949.3 eV and 933.5/929.3 eV, respectively. Judging from a simple comparison with a spectrum of Pr_6O_{11}, these signals at lower binding energies agreed with Pr^{3+}, whereas those at higher energies was assigned to Pr^{4+}. The Pr^{4+} species were also detected on Pr_2O_2S, which was synthesized by heating $Pr_2O_2SO_4$. These results suggest that the surfaces of $Pr_2O_2SO_4$ as well as Pr_2O_2S are easily oxidized to yield a considerable amount of Pr^{4+}. On the basis of the intensity of each XPS signals, the fraction of Pr^{4+} was calculated to be 64% for $Pr_2O_2SO_4$ and 50% for Pr_2O_2S. However, the concentration of Pr^{4+} should be negligible when all of the bulk Pr is taken into consideration, because as it was proved in the Ref. [12] the oxygen storage in the present system is determined only by sulphur redox. It is assumed that the redox of Pr on the surface would affect the reduction/reoxidation of bulk oxysulfate. As a result of charge compensation accompanied by the creation of Pr^{4+}, oxygen would be adsorbed as negatively charged species onto the surface and may thus promote the oxidation of S^{2-} to SO_4^{2-}. In Ref. [12], the oxidation state of Pr^{3+} can promote the reduction of SO_4^{2-} to S^{2-}, and in a similar way, Pr^{4+} can promote the reoxidation of S^{2-} to SO_4^{2-}.

These results may imply that the redox between Pr^{3+} and Pr^{4+} on the surface should play a key role as a mediator for the reduction/reoxidation between S^{2-} and SO_4^{2-} in the Pr system.

The oxygen storage/release by oxysulfate/oxysulfite is given by the chemical reaction [1]:

$$Pr_2O_2SO_4 \rightleftharpoons Pr_2O_2S + 2O_2 \tag{1.3}$$

Furthermore there is some preliminary theoretical work for the oxysulfate Pr_2O_2S using the local density approximation (LDA) in DFT. Calculated properties related to the ground state appear consistent with the experimental results [18]. The optimized structural parameters along with experimental values, shown in parentheses are: $a = 3.93(3.98)$ Å, $c = 6.75(6.83)$ Å, $B = 119$ GPa (Bulk modulus), strength of the cohesive (atomization) energy = 42.0 eV [18, 19] . According to the Materials Project database, calculations using an xc functional based on GGA has the following characteristics: $a = 4.01$ Å, $c = 6.88$ Å, $V = 95.71$ Å^3 , band gap = 2.86 eV and the space group is trigonal $P\bar{3}m1$ (#164) (Fig. 1.2d)[13].

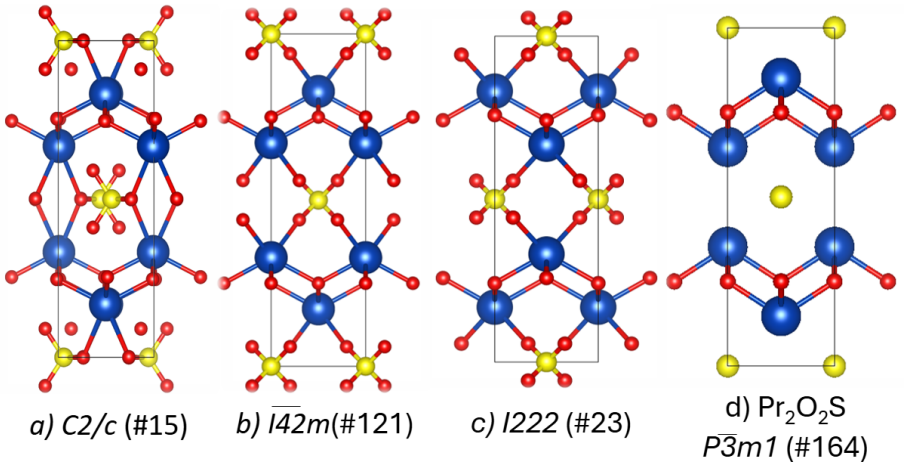

Figure 1.2: Crystal structure of $Pr_2O_2SO_4$ and Pr_2O_2S. The figures were reproduced with the VESTA visualization software [20]. The large yellow spheres represent praseodymium (Pr), the small yellow sulphur (S) and red represents the oxygen (O) atoms.

1.4. Theoretically modeling interacting electrons and nuclei

To describe the complete quantum mechanical behaviour of electrons in solids it is strictly necessary to calculate the many-electron wavefunction of the system. In principle, this may be obtained from the time-independent Schrödinger equation, but in practice the potential effectively experienced by each electron is dictated by the behaviour of all the other electrons in the solid.

To start from a general point of view for a system of electrons and nuclei, we consider the Hamiltonian:

$$\hat{H} = -\frac{\hbar^2}{2m_e}\sum_i \nabla_i^2 - \sum_{i,I}\frac{Z_I e^2}{|r_i - R_I|} + \frac{1}{2}\sum_{i\neq j}\frac{e^2}{|r_i - r_j|} - \sum_I \frac{\hbar^2}{2M_I}\nabla_I^2 + \frac{1}{2}\sum_{I\neq J}\frac{Z_I Z_J e^2}{|R_I - R_J|}, \quad (1.4)$$

where r_i is the coordinate of the i-th electron and the nuclei, with charge Z_I, mass M_I and position R_I, being denoted by the upper subscripts. This Hamiltonian captures the kinetic energy of the electrons, the interactions between nuclei and electrons, electron-electron interactions, kinetic energy of the nuclei and interactions between the nuclei, respectively. It is essential to include the many-body terms, namely the electron-electron Coulomb interactions and the complex interactions among nuclei. However, the central issue to the theory of electronic structure is the development of methods to treat electronic correlations with sufficient accuracy that one can predict the diverse array of phenomena exhibited by matter.

One of the first assumptions to deal with the many-body problem is to consider that the mass of the nuclei are much larger than that of the electrons, so that the kinetic energy of the nuclei can be ignored. This is the Born-Oppenheimer or adiabatic approximation [21]. In this way, we can focus on the Hamiltonian for the electrons, in which the positions of the nuclei are fixed parameters, and therefore we can approach the solution of the many-body electronic problem resorting to the following expression:

$$\hat{H} = \sum_i \frac{\hat{p}_i^2}{2m} + \frac{1}{2}\sum_{i\neq j}\frac{e^2}{|\hat{\mathbf{r}}_i - \hat{\mathbf{r}}_j|} + \hat{H}_{e-b} + \hat{H}_{b-b}, \quad (1.5)$$

where $\hat{\mathbf{r}}_i$ and $\hat{\mathbf{p}}_i$ are the quantum mechanical operators of the coordinate and the momentum of the i-th electron, m is the electron mass and e is the magnitude of the electron charge. The last two terms of the Eq. 1.5 represent the electron-background (mainly the potential acting on the electrons due to the nuclei) and background-background interactions (interaction of nuclei with one another and any other terms that contribute to the total energy of the system but are not germane to the problem of describing the electrons) and are given by [22]:

$$\hat{H}_{e-b} = -e^2\int d\mathbf{r}\int d\mathbf{r}'\frac{\hat{n}(\mathbf{r})n_b(\mathbf{r}')}{|\mathbf{r}-\mathbf{r}'|}, \quad (1.6)$$

$$\hat{H}_{b-b} = \frac{e^2}{2}\int d\mathbf{r}\int d\mathbf{r}'\frac{n_b(\mathbf{r})n_b(\mathbf{r}')}{|\mathbf{r}-\mathbf{r}'|}, \quad (1.7)$$

where $\hat{n}(\mathbf{r}) = \sum_{i=1}^{N}\delta(\mathbf{r}-\mathbf{r}_i)$ is the electron number density operator and $en_b(\mathbf{r}) = en$ is the (uniform) charge density of the background. With this last expression, we have replaced

the actual structure of the background (the atomic lattice) by an homogeneous jelly-like continuum of positive charge: and that is why this model is called “jellium model”. The main idea is to get rid of the complications associated with the structure of the host material, while focusing on the distinctive effects of the electron–electron interaction. Although this simplification is probably too drastic in traditional metallic systems, it is quite realistic in the semiconductor systems. For example, in Appendix A we describe how this exchange energy arises from this model.

Another important attempt to solve the many-body problem was made by D. R. Hartree [23] with the assumption that the many-electron wavefunction was formed by the product of a set of single-electron wavefunctions. Having made this assumption it was possible to proceed using the variational principle. This principle states that if a given system may be described by a set of unknown parameters, then the set of parameter values which most correctly describes the ground state of the system (i.e. the state in which the system exists when not perturbed by outside influences) is just that set of values which minimises the total energy. After using this method, one manages to obtain a set of N equations (being N the number of electrons) that look like the time-independent Schrödinger equation, with a Hartree potential that depends on the time-averaged electron distribution of the system. Consequently, the Hartree approximation allows us to calculate approximate single-particle wavefunctions for the electrons in crystals , but unfortunately, it does not provide particularly good results. The problem appears in the assumption of a product wavefunction. By being a symmetrical function, it stays exactly the same after interchanging two fermions. For the Pauli exclusion principle to be taken into consideration, the process of exchange interaction between fermions should leave the wavefunction unaltered except for a change of sign. Any wavefunction possessing that property will tend to zero (indicating zero probability) for any pair of fermions with the same quantum numbers that approach each other. Therefore the Hartree Approximation ignores the electron spin and does not satisfy the Pauli Exclusion Principle.

The Hartree-Fock (HF) approach is an improvement to the former method, since it writes the many-electron wavefunction as a Slater determinant of the single-electron wavefunction, that by principle defines the antisymmetry property. Now, instead of just having the Hartree potential that depends on the average electron distribution, we also have the exchange potential that arises from the use of an antisymmetric wavefunction. The HF approach yields quite credible results for molecules and finite systems, but typically fails for solids. It does not account for the correlation interaction, with consequences such

as predicting band-gaps that may be considerably larger than the experimental values in semiconductors [24].

In 1964, Hohenberg and Kohn pointed out that the prohibitive challenge in accurately obtaining the many-electron wavefunction was the fact it depends on $3N$ parameters (the 3D degrees of freedom of the electrons) and has both a magnitude and a complex phase. To overcome this, they chose the electron density as their fundamental variable and considered the ground state of the system to be defined by the electron density distribution which minimises the total energy. This paradigm shift introduced the notion of energy functional and the problem of finding the ground state of the many-electron system becomes formulated variationally in terms of the total electron density. This reformulation immensely simplifies its numerical solution, since the target to compute is now a single real function of three parameters, rather than a complex function of $3N$ coordinates. For many years now, DFT has been used with great success to investigate the ground state properties of solids, both in the bulk form, at surfaces and at interfaces.

1.5. Objectives of this dissertation and thesis outline

By using first-principles techniques, we want to compute and characterize the different polymorphs [orthorhombic $I222$(#23), monoclinic $C2/c$ (#15) and tetragonal $I\overline{4}2m$ (#121)] and define respective energetic stability. Additionally we will compute the electronic band structures as well as the total and projected density of states. It is also important to assess the possibility of magnetic ground-states and the influence of the f-states in the electronic nature of $Pr_2O_2SO_4$. During this dissertation we would also like to conclude the influence of the addition of the Hubbard term in our system, which will correctly treat the strongly correlated f-states of Pr. Finally we will analyse the efficiency of the redox equation between the praseodymium oxysulfate/oxysulfide.

The dissertation is organized as follows. Chapter 2 summarizes the formulation of DFT, DFT+U+V, DFPT and some characteristics of the magnetism of the material ; whereas chapter 3 will present the applied software suites and the considered parameters for the calculations. Chapter 4 summarizes the obtained results throughout the dissertation project that will be further discussed in section 4.5; and finally in chapter 5, we provide the conclusions of this work and future perspectives.

2. Theoretical methods

In this chapter we will detail the employed theoretical methodologies considered during the dissertation project. We will provide an overview of DFT, used primarily to compute the ground state energies, and the theory of DFT+U considered to assess the effects of the f orbitals in the characteristics of the material. Then, it will be briefly discussed the possible magnetic orders and the energetic results of each one of the studied polymorphs.

2.1. Density Functional Theory

The basic idea, introduced by Hohenberg, Kohn and Sham [25, 26] is to describe the system in terms of the total electronic density, $n(\mathbf{r})$, without explicit reference to the many-body wavefunction of the 3N electronic degrees of freedom, where N is the number of electrons. The ground-state energy of a quantum system can then be determined by minimizing the energy, expressed as a functional of the density. The implementation of the Hohenberg-Kohn minimum principle leads to mean-field-like equations, known as the Kohn-Sham (KS) equations. The key advantage of this approach is that the KS equations can be numerically solved within a time-scale that grows as a power of the number of electrons [22].

2.1.1 The variational principle for the density

Consider an N-electron system described by the Hamiltonian $\hat{H} = \hat{T} + \hat{H}_{e-e} + \hat{V}$, where $\hat{T}$ and $\hat{H}_{e-e}$ are the kinetic energy and the electron-electron interaction, respectively, and $\hat{V}$ is the potential energy associated with an external local potential $V(\mathbf{r})$. This term can be written as:

$$\hat{V} = \int V(\mathbf{r}) n(\mathbf{r}) dr \quad ; \quad \hat{n}(\mathbf{r}) = \sum_{i=1}^{N} \delta(\mathbf{r} - \hat{r}_i) \tag{2.1}$$

where $\hat{n}(\mathbf{r})$ is the density operator. When the actual structure of the background on which the electrons roam (e.g., the atomic lattice) is replaced by a homogeneous jelly-like continuum of positive charge we get rid of the complications associated with the structure of the host material, while focusing on the distinctive effects of the electron–electron interaction. This is called the “jellium model” [22]. According to the Rayleigh-Ritz principle, the ground-state energy (E) is found by minimizing the expectation value of the Hamiltonian (H) with respect to the wavefunction ψ, where ψ must be antisymmetric under interchange

of two electron orbital and spin coordinates, and these must satisfy the boundary conditions appropriate to the system. To search for this wavefunction, first, a guess density n(**r**) is chosen, and the equation is minimized within the subset of wavefunctions that yield that density:

$$E_V[n] = \min_{\psi \to n(\mathbf{r})} \langle \psi | \hat{H} | \psi \rangle = F[n] + \int V(\mathbf{r}) n(\mathbf{r}) dr \tag{2.2}$$

$$F[n] = \min_{\psi \to n(\mathbf{r})} \langle \psi | \hat{T} + \hat{H}_{e-e} | \psi \rangle. \tag{2.3}$$

Second, $E_V[n]$ is minimized with respect to the density. This leads to the desired variational principle of the density [22]:

$$E = \min_{n(\mathbf{r})} \left\{ F[n] + \int V(\mathbf{r}) n(\mathbf{r}) dr \right\}. \tag{2.4}$$

The functional F is universal in the sense that it is an intrinsic property of the inhomogeneous electron liquid, being the same for all systems regardless of $V(\mathbf{r})$. It is now important to state some definitions related to functionals. A functional, $F[f]$, is defined as a mapping of an entire function f to a number $F[f]$. A functional derivative is then defined by a variation of the functional $\delta F[f] = F[f + \delta f] - F[f] = \int_{x_{min}}^{x_{max}} \frac{\delta F}{\delta f(x)} \delta f(x) dx$ where the quantity $\delta F / \delta f(x)$ is the functional derivative of F with respect to variation of $f(x)$ at the point x. An example of a functional is a definite integral of $w(x)f(x)$, $F_w[f] = \int_{x_{min}}^{x_{max}} w(x) f(x) dx$ where $\frac{\delta F_w}{\delta f(x)} = w(x)$ and $w(x)$ is some fixed weighting function [21].

Let us now come back to the energy functional $E_V[n]$. Due to an infinitesimal variation of the density and assuming that the functional derivative of $F[n]$ exists it can be written:

$$E_V[n + \delta n] - E_V[n] = \int \left[\frac{\delta F[n]}{\delta n(\mathbf{r})} + V(\mathbf{r}) \right] \delta n(\mathbf{r}) dr. \tag{2.5}$$

It follows from the minimum condition, in Eq. (2.4), that the quantity in the square brackets must vanish at the ground-state density. Therefore, the ground-state density must satisfy the relation:

$$\frac{\delta F[n]}{\delta n(\mathbf{r})} = -V(\mathbf{r}). \tag{2.6}$$

2.1.2 The Hohenberg-Kohn theorem

The electronic density $n(\mathbf{r})$ is said to be V-representable if it can occur in the ground-state of $\hat{H}$ with a suitable local potential $V(\mathbf{r})$. A given potential can yield degenerate ground-states and multiple densities associated with them, but two different potentials will never yield the same density. This statement is known as the *first Hohenberg-Kohn*

theorem and it proves that, for any system of interacting particles in a external potential $V(\mathbf{r})$, if one knows the ground-state density it is possible to determine the Hamiltonian, the ground-state wavefunction and all the ground-state properties of a many-body system. In conclusion, the ground-state density uniquely determines (up to a constant) the local external potential $V(\mathbf{r})$, that gives rise to it. Hohenberg and Kohn also stated another theorem related to the energy functional $E[n]$. The *second Hohenberg-Kohn theorem* states that a universal functional for the energy $E[n]$ in terms of the density, can be defined for any external potential $V(\mathbf{r})$. For any particular $V(\mathbf{r})$, the exact ground state energy of the system is the global minimum value of this functional, and the density that minimizes the functional is the exact ground state density $n(\mathbf{r})$ [21].

2.1.3 The Kohn-Sham equations

The main problem is that the form of the functional $F[n]$ is not known. Since in a non-interacting system, the density can be calculated exactly, Kohn and Sham came up with a strategy to solve this problem. The strategy lies in the affirmation that the ground-state density of the interacting system can be represented as the ground-state density of a non-interacting system in some local external potential $V_{KS}(\mathbf{r})$ (where the subscript KS refers to the KS theory). In other words, DFT will take the term $\hat{H}_{e-e}$ of the Hamiltonian and include it in the potential so that one has an effective Hamiltonian for a non-interacting single electron. Then, according to the general density-functional formalism, the ground-state density can be obtained by minimizing the non-interacting energy functional [22]:

$$E^{(0)}_{V_{KS}}[n] = T_s[n] + \int V_{KS}(\mathbf{r})n(\mathbf{r})dr \quad ; \quad T_s[n] = \min_{\psi \to n(\mathbf{r})} \langle \psi | \hat{T} | \psi \rangle \tag{2.7}$$

where $T_s[n]$ is the non-interacting kinetic energy functional, i.e, the kinetic energy of a non-interacting system with ground-state density $n(\mathbf{r})$ and the superscript $^{(0)}$ refers to the fact that the energy functional is of a non-interacting system. The stationary condition for the non-interacting energy functional has the form:

$$\frac{\delta T_s[n]}{\delta n(\mathbf{r})} = -V_{KS}(\mathbf{r}), \tag{2.8}$$

where $V_{KS}(\mathbf{r})$ is defined formally as a functional of the density. Now, following Kohn and Sham, we decompose $F[n]$ as follows:

$$F[n] = T_s[n] + E_H[n] + E_{xc}[n], \tag{2.9}$$

where $E_H[n]$ is the Hartree energy functional:

$$E_H[n] = \frac{e^2}{2} \int dr \int dr' \frac{n(\mathbf{r})n(\mathbf{r}')}{|\mathbf{r} - \mathbf{r}'|} \tag{2.10}$$

and $E_{xc}[n]$ is the xc energy functional (for more information see the appendix (A.1)). All many-body effects of exchange and correlation are grouped into the xc energy E_{xc}. Comparing to the Hohenber-Kohn Eq. (2.3) and the KS Eq. (2.7), we can re-write E_{xc} as [21]:

$$E_{xc}[n] = \langle \vec{T} \rangle - T_s[n] + \langle \vec{V} \rangle - E_H[n]. \tag{2.11}$$

It is important to note the difference between the non-interacting kinetic energy $T_s[n]$ and $T[n]$. The latter is defined as the expectation value of $\hat{T}$ in the state that has density $n(\mathbf{r})$ and minimizes the expectation value of $\hat{T} + \hat{H}_{e-e}$ (where $T[n] \geq T_s[n]$ for every n). The extra kinetic energy in the interacting system arises from correlations in the ground state wavefunction.

Replacing the decomposition into the stationary condition, we obtain:

$$\frac{\delta T_s[n]}{\delta n(\mathbf{r})} = -V(\mathbf{r}) - V_H(\mathbf{r}) - V_{xc}(\mathbf{r}), \tag{2.12}$$

where $V_H(\mathbf{r}) = e^2 \int \frac{n(\mathbf{r}')}{|\mathbf{r}-\mathbf{r}'|} d\mathbf{r}' = \frac{\delta E_H[n]}{\delta n}$ is the Hartree potential and $V_{xc}(\mathbf{r}) = \frac{\delta E_{xc}[n]}{\delta n(\mathbf{r})}$ is the xc potential, obtained as a functional of the density. The expression of the KS potential is hence defined as a contribution of three terms:

$$V_{KS}(\mathbf{r}) = V(\mathbf{r}) + V_H(\mathbf{r}) + V_{xc}(\mathbf{r}). \tag{2.13}$$

Now it can be concluded that minimizing $E^{(0)}_{V_{KS}}[n]$ is equivalent to finding the ground-state density of an non-interacting electron system in the presence of the KS potential $V_{KS}(\mathbf{r})$. To calculate the ground-state density one just needs to solve the KS equations [22]:

$$\left[-\frac{\hbar^2}{2m}\nabla^2 + V(\mathbf{r}) + V_H(\mathbf{r}) + V_{xc}(\mathbf{r}) \right] \psi_\alpha(\mathbf{r}) = \varepsilon_\alpha \psi_\alpha(\mathbf{r}), \tag{2.14}$$

and the ground-state density is given by:

$$n(\mathbf{r}) = \sum_{\alpha=1}^{N} \sum_{s} |\psi_\alpha(\mathbf{r})|^2, \tag{2.15}$$

where the summation over α is over all occupied electron states. The two equations, (2.13) and (2.14), describe a self-consistent procedure. One makes an initial guess at the density $n(\mathbf{r})$ and uses it to find the eigenfunctions $\psi_\alpha(\mathbf{r})$. These eigenfunctions are then used to obtain a more refined and accurate density. The self-consistent cycle is repeated

until the initially defined convergence threshold is reached.

Although the KS method provides reasonable results when compared to experimental data, being computationally more efficient when compared to other theoretical frameworks (i.e. HF), it carries inherent implications. Primarily, the effective potential that appears in the KS equations, though local in space (in the sense that it acts on the wavefunction as a simple multiplication), has a nonlocal dependence on the density, and can only be approximately described. Secondly, the wavefunction obtained from the solution of the KS equations, while giving (in principle) the exact ground-state density, is by no means a good approximation to the true ground-state wavefunction. Finally, the universality of the effective potential, while unifying the treatment of many different systems, tends to obscure the physical peculiarities of each one [22].

2.1.4 Local Density Approximation and Generalized Gradient Approximation

Solids can often be considered as close to the limit of the homogeneous electron gas. In that limit, it is known that the effects of exchange and correlation are local in character, so the simplest approximation developed to describe the xc potential is the LDA [or more generally the local spin density approximation (LSDA)], in which the xc energy density at each point assumed to be the same as in a homogeneous electron gas with that density [21],

$$\begin{aligned} E_{xc}^{\mathrm{LSDA}}[n^{\uparrow}, n^{\downarrow}] &= \int d^3r\, n(\mathbf{r}) \varepsilon_{xc}^{hom}(n^{\uparrow}(\mathbf{r}), n^{\downarrow}(\mathbf{r})) \\ &= \int d^3r\, n(\mathbf{r}) [\varepsilon_{x}^{hom}(n^{\uparrow}(\mathbf{r}), n^{\downarrow}(\mathbf{r})) + \varepsilon_{c}^{hom}(n^{\uparrow}(\mathbf{r}), n^{\downarrow}(\mathbf{r}))], \end{aligned} \tag{2.16}$$

where the ε_{xc}^{hom} is the xc energy per unit volume of an electron gas of uniform spin densities $n_{\uparrow}$ and $n_{\downarrow}$. The exchange energy of the homogeneous electron gas, ε_{x}^{hom}, can be analytically calculated from this expression [27]:

$$E_{x}^{\mathrm{LDA}}[n] = -\frac{3}{4}\left(\frac{3}{\pi}\right)^{1/3} \int n(\mathbf{r})^{4/3} dr. \tag{2.17}$$

The correlation energy of the homogeneous electron gas, ε_{c}^{hom} is obtained by parametrizing the results for several densities originally obtained using Monte Carlo methods by Ceperley and Alder [28]. Currently, there exist several parametrized forms for this functional, e.g. PZ81 [29], PW92 [30].

Another option for the xc potential is the generalized-gradient approximation, which is a simple extension of the LSDA. This approximation is defined by including a gradient

correction to the density, thus incorporating the effects of inhomogenities to the electron density (semi-local method). It is convenient to define the functional as generalized form of Eq. (2.16),

$$\begin{aligned} E_{xc}^{GGA}[n^{\uparrow}, n^{\downarrow}] &= \int d^3 r n(\mathbf{r}) \varepsilon_{xc}(n^{\uparrow}, n^{\downarrow}, |\nabla n^{\uparrow}|, |\nabla n^{\downarrow}|, ...) \\ &= \int d^3 r n(\mathbf{r}) \varepsilon_x^{hom}(n) F_{xc}(n^{\uparrow}, n^{\downarrow}, |\nabla n^{\uparrow}|, |\nabla n^{\downarrow}|, ...), \end{aligned} \tag{2.18}$$

where F_{xc} is dimensionless and $\varepsilon_x^{hom}(n)$ is the exchange energy of the unpolarized gas. Several options for the factor F_{xc} are used like Becke(B88) [31], Perdew Wang (PW91) [32] and Perdew, Burke, and Enzerhof (PBE) [33].

2.1.5 Advantages and Disadvantages

One advantage of employing DFT is the possibility of increasing the chemical accuracy without the additional increase in computational time and memory requirements, when compared to previous and/or alternative computational chemical methods. Perhaps most importantly, DFT has and continues to play a crucial role in scientific progress by predicting and/or validating the discovery of novel phenomena in solid-state systems. It also helps guiding the quantitative optimization of parameters for all kinds of technological applications and helps accelerating materials discovery (examples of that include the Materials Project database [34] and the Open Quantum Materials Database [35]).

Nevertheless, one of the main drawbacks of the DFT framework is the challenge in determining the approximation scheme to the xc functional that can provide the most reliable results for a particular class of materials. Besides that, as a variational approach, conventional DFT cannot reliably be used to provide information about excited properties of the systems (e.g. optical properties).

Lastly, its is well established that DFT relying on conventional xc functionals, can fail notoriously when applied to systems which ground state carries partially-filled $d-$ and $f-$ orbitals. The challenge here is a fundamental one, since such systems generically involve strong Coulomb-induced correlations between the electrons in such narrow-orbital states/bands. The situation is such that even basic qualitative features such as determining whether the ground state is metallic or insulating, magnetic or non-magnetic can be severely missed in the results. This particular drawback is going to be studied in the next

subsection, where we shall discuss an extension to DFT known as DFT+U, that attempts to capture the leading effect of strong correlations, when these are relevant.

2.2. Hubbard-extended DFT

In this section we will begin to summarise the formulation of DFT+U+V and illustrate the linear-response (LR) approach to perform the calculation of the Hubbard parameters, U and V, starting from a real-space formulation, and reviewing its recent reciprocal-space implementation based on Density functional perturbation theory (DFPT).

The KS approach has led to very useful approximations that are now the basis of most calculations that attempt to make "first-principles" or "*ab initio*" predictions for the properties of condensed matter and large molecular systems. However, systems with electronic properties that are controlled by many-body electronic interactions (correlated systems) are poorly described with the classic DFT approach. In particular, difficulties arise when a conventional DFT approach is applied to the treatment of the electronic structure of the material where some of the ions contain partially filled valence d- or f-shells. It was shown in Ref. [36] that for many of the transition metal oxides, TMO, (which contain partly filled d-states in comparison to the conventional oxides with filled d-states), both the different parametrization of LSDA and GGA fail in predicting the insulating behavior of many simple TMO, by severely underestimating their electronic band gap, and, in most cases, incorrectly predicting the ground-state to be metallic [37, 38].

This failure comes primarily from an incorrect description of the strong Coulomb repulsion of the filled and empty d- and f-states localized on the metal ions. Since the strength of the effective on-site Coulomb interaction, between d-electrons and also f-electrons, is comparable with the valence bandwidth, the processes associated with electron transfer between two metal ions (or resulting from addition or removal of d- and f-electrons) give rise to large fluctuations of the energy of the system, leading to the localization of charge carriers and to the formation of energy band gaps [39].

Such discrepancies reflect the limitations of the approximations used in parametrizing electronic interactions at the level of a xc energy, E_{xc} (for example LDA, GGA) that suffer from self-interaction errors (SIE) since they cannot properly capture the electron-electron repulsion effects. The inability of the E_{xc} term to completely cancel out the electronic self-interaction contained in the Hartree term leads to a remaining "fragment" of the same

electron that is still there and can induce added self-interaction, consequently inducing an overdelocalization of the wavefunctions.

As a result, DFT often fails significantly in predicting the properties of systems which ground state is characterized by a more pronounced localization of electrons.

We are aware that electrons in molecules or solids are often delocalized, meaning they are not confined to a single atom but instead are spread over multiple atoms or regions of space. In systems with strongly localized d- and f-states, the electronic wavefunctions (seen at an effective single-particle level) are diffuse and exhibit complex shapes compared to s and p orbitals, leading to a great spatial extent. However, these evidence regions of high electron density close to the nucleus as well, contributing to their localization. In terms of the inner electrons, they shield the outer d and f-electrons from the full nuclear charge, reducing the effective nuclear charge experienced by these electrons, confining respective states closer to the nucleus. Such a feature also contributes to DFT not performing well for these strongly correlated systems.

A proposal to minimize such errors is to add a so-called Hubbard U correction to the DFT energy. The Hubbard U parameter, present in this method, represents the effective strength of the on-site Coulomb repulsion between electrons at the same atomic orbitals, enabling the inclusion of the so-called “on-site repulsion”. It is important to note that this Hubbard correction is applied only to the strongly correlated electronic states (d- and f-orbitals), while treating the rest of the valence electrons of the system through the conventional DFT approximations.

An extended formulation of this approach is called DFT+U+V and it takes into account intersite Hubbard interactions through the parameter V, allowing an improved description of the localized electrons, even in the presence of significant hybridization with neighbouring atoms.

In these extensions to DFT, a small number of localized orbitals is selected and the electronic correlation associated to these is treated in a special manner. The obtained results strongly depend on the definition of the localized orbitals and on the choice of the interaction parameters applied in the calculation, which should be determined in an internally consistent way [37].

2.2.1 Extended DFT+U+V with on-site and intersite electronic interactions

This section presents an overview of the DFT+U+V following reference [40]. For the sake of simplicity, the formalism is presented in the framework of norm-conserving (NC) pseudopotentials (PPs), for non-metallic ground states, in the collinear spin-polarized case.

DFT+U+V consists of a simple corrective Hamiltonian, added to the (approximate) DFT energy functional, that is shaped on the Hubbard model. In its single-band formulation the Hubbard Hamiltonian can be written as follows:

$$H_{Hub} = t \sum_{\langle i,j\rangle,\sigma} (c^{\dagger}_{i,\sigma} c_{j,\sigma} + h.c) + U \sum_{i} n_{i,\uparrow} n_{i,\downarrow} + V \sum_{<i,j>} n_i n_j, \tag{2.19}$$

where $\langle i, j\rangle$ denotes nearest-neighbor sites, $c^{\dagger}_{i,\sigma} c_{j,\sigma}$ and $n_{i,\sigma}$ are electronic creation, annihilation and number operators for electrons of spin σ on site i. The factor U represents the effective strength of the "on-site" Coulomb repulsion and V refers to the strength of the interaction between electrons on neighbor sites i and j.

When electrons are strongly localized, their motion becomes 'correlated' and their wavefunction acquires a marked many-body character. Capturing all the features of a strongly correlated ground state, by considering effective electronic interaction potentials that are constructed as functionals of the charge density, is a considerable task. Within these conditions, the motion of electrons is described by a "hopping" process from one atomic site to its neighbors (first term of the equation), the amplitude of which t is proportional to the bandwith of the system and thus represents the single-particle term of the total energy. The Coulomb repulsion, instead, is only accounted for between electrons, of the same atomic site, through a term proportional to the product of the occupation numbers of atomic states on the same site. The explicit account for on-site electronic repulsions is ideally suited to study Mott insulators. Mott insulators are a class of materials that are expected to conduct electricity according to conventional band theories, but instead act as insulators (particularly at low temperatures) because of their strong electron-electron interactions, which are not considered in conventional band theory. In fact, in these systems the insulating character of the ground state stems from the dominance of short-range Coulomb interactions (the energy cost of double occupancy of the same site) over single-particle terms of the energy (generally minimized by electronic delocalization) that leads to the localization of electrons on atomic orbitals ($t \ll U$).

Generally, the correction of the Hubbard energy terms to the DFT energy functional is written as follows [37, 41, 42]:

$$E_{DFT+U+V}[n(\mathbf{r})] = E_{DFT}[n(\mathbf{r})] + E_{UV}[n(\mathbf{r})] = E_{DFT}[n(\mathbf{r})] + E_U[n_m^{I\sigma}] + E_V[n_m^{I\sigma}] - E_{dc}[n^{I\sigma}], \tag{2.20}$$

where E_{DFT} represents the approximate DFT energy (constructed, e.g., within the LSDA or the GGA), while E_{UV} contains the additional Hubbard term.

In its original definition, the functional defined in Eq. (2.20) was not invariant under rotation of the atomic-orbital basis set used to define the occupancies $n_m^{I\sigma}$. We can use a mean-field approximation of the electronic interaction energy expressed in terms of atomic orbitals to obtain a rotationally invariant formulation, which is a formulation borrowed from the HF method with renormalized Slater integrals [43]:

$$\begin{aligned} E_{int} &= \frac{1}{2} \sum_{I,J,K,L} \sum_{i,j,k,l} \sum_{\sigma\sigma'} \langle \phi_i^I \phi_j^J | \, V_{ee} \, | \phi_k^K \phi_l^L \rangle \\ &\times \; (n_{k,i}^{KI\sigma} n_{l,j}^{LJ\sigma'} - \delta_{\sigma\sigma'} n_{kj}^{KJ\sigma} n_{li}^{LI\sigma'}). \end{aligned} \tag{2.21}$$

In this equation the atomic orbitals are classified by a site index (upper case letter) and a state index (lower case letter) that runs over specific manifolds of states of the atom labeled with the same letter (e.g. i indicates atomic orbitals of the atom I). The quantities $\langle \phi_i^I \phi_j^J | \, V_{ee} \, | \phi_k^K \phi_l^L \rangle$ represent the effective Coulomb interactions between the indicated atomic orbitals and $n_{k,i}^{KI\sigma}$ are the mean-field averages of creation and annihilation operators, $\langle c_i^{I\sigma\dagger} c_k^{K\sigma} \rangle$. The on-site E_U term of the corrective functional in Eq. 2.20 can be formally obtained from the expression in Eq. 2.21 neglecting all the interactions but the Hartree and Fock couplings between orbitals on the same site. Due to the localization of atomic states it is further assumed that the effective interactions are all equal to their atomic averages: $\langle \phi_i^I \phi_j^J | \, V_{ee} \, | \phi_k^K \phi_l^L \rangle \rightarrow \delta_{IK}\delta_{JL}\delta_{IJ}\delta_{ik}\delta_{jl} U^I = \frac{\delta_{IK}\delta_{JL}\delta_{IJ}\delta_{ik}\delta_{jl}}{(2l_I+1)^2} \sum_{i',i''} \langle \phi_{i'}^I \phi_{i''}^I | \, V_{ee} \, | \phi_{i'}^I \phi_{i''}^I \rangle$. Within this approximation one easily obtains:

$$E_U = \sum_I \frac{U^I}{2} \left[(n^I)^2 - \sum_\sigma Tr[(\mathbf{n}^{I\sigma})^2] \right], \tag{2.22}$$

where n^I is the total number of electrons on the atomic states of atom I: $n^I = \sum_\sigma Tr\, \mathbf{n}^{I\sigma}$. We can obtain the corrective functional $E_U - E_{dc}$ presented in Eq. (2.20) using the so called "fully localized limit" (FLL), according to which the double-counting term E_{dc} is the mean-field approximation of E_U (Eq. (2.22)) in the limit where atomic orbitals are either

fully occupied or empty. This double-counting functional has the following expression:

$$E_{dc} = \sum_I \frac{U^I}{2} n^I (n^I - 1). \tag{2.23}$$

Subtracting Eq. (2.23) from (2.22) we obtain (see also Eq. (A.10)):

$$E_U - E_{dc} = \sum_{I,\sigma} \frac{U^I}{2} Tr[\mathbf{n}^{I\sigma}(\mathbf{1} - \mathbf{n}^{I\sigma})]. \tag{2.24}$$

In this equation the trace operator indicates the sum over the diagonal elements of the matrix it acts on: $Tr\mathcal{O} = \sum_m \mathcal{O}_{m,m}$. $\mathbf{n}^{I,\sigma}$ is the "on-site" occupation matrix that is defined by the projection of the occupied KS orbitals of the spin σ on the localized (atomic) states of orbital quantum number l (typically of d or f kind) ϕ^I_m:

In Eq. (2.24), $\mathbf{n}^{I\sigma}$ are matrices which measure the occupation of localized orbitals $\phi^I_m(\mathbf{r}) = \phi^{\gamma(I)}_m(\mathbf{r} - \mathbf{R}_I)$ centered on the I-th atomic site in the cell $\mathbf{R}_I$ ($\gamma(I)$ is the atomic type of the I-th atom). If we consider a periodic insulating crystal, these occupation matrices can be computed as [44]:

$$n^{I\sigma}_{m_1,m_2} = \sum_{k,\nu} f^\sigma_{k\nu} \left\langle \psi^\circ_{\nu k\sigma} \right| \hat{P}^I_{m_2,m_1} \left| \psi^\circ_{\nu k\sigma} \right\rangle, \tag{2.25}$$

$$P^{I\sigma}_{m_2,m_1} = \left| \phi^I_{m_2} \right\rangle \left\langle \phi^I_{m_1} \right|, \tag{2.26}$$

where m is the magnetic quantum number associated with l ($-l \leq m \leq l$), while $f^\sigma_{k\nu}$ are the occupations of the KS orbitals $\psi_{\nu k\sigma}$ based on the distribution of their energies around the Fermi level.

The projector $\hat{P}^I_{m_2 m_1}$ is the key component of Hubbard-corrected functionals, since it defines the Hubbard manifold (typically localized on an atom) upon which the corrections are constructed. It is important to stress that the simplified functional in Eq. (2.24) is rotationally invariance through its dependence on the trace of occupation matrices and of their products. Conversely, the formal resemblance to the xc energy functional is lost in this formulation and only one interaction parameter (U^I) is needed to specify the corrective functional.

Generalizing the approach described above the E_V of DFT+U+V can be obtained from Eq. (2.21) supposing that a significant contribution to the corrective potential also comes from the interactions between orbitals on pairs of distinct sites. Similarly to the on-site

case, the (HF-like) effective inter-site interactions are all assumed to be equal to their atomic averages over the states of the two atoms: $\langle \phi_i^I \phi_j^J |\, V_{ee}\, | \phi_k^K \phi_l^L \rangle \rightarrow \delta_{IK}\delta_{JL}\delta_{IJ}\delta_{ik}\delta_{jl} V^{IJ} = \frac{\delta_{IK}\delta_{JL}\delta_{ik}\delta_{jl}}{(2l_I+1)(2l_J+1)} \sum_{i',j'} \langle \phi_{i'}^I \phi_{j'}^J |\, V_{ee}\, | \phi_{i'}^I \phi_{j'}^J \rangle$. Note that $V^{II} = U^I$. Within this hypothesis it is easy to derive the following expression:

$$\begin{aligned} E_U + E_V o.p = \quad & \sum_I \frac{U^I}{2} \left[(n^I)^2 - \sum_\sigma Tr[(\mathbf{n}^{II\sigma})^2] \right] \\ & - \sum_{IJ}^{*} \frac{V^{IJ}}{2} \left[n^I n^J - \sum_\sigma Tr(\mathbf{n}^{IJ\sigma}\mathbf{n}^{JI\sigma}) \right] \end{aligned} \tag{2.27}$$

where the star in the sum operator denotes that for each atom I , index J covers all its neighbors up to a given distance (or belonging to a given shell). Eq. (2.27) uses a generalized formulation of the occupation matrix (Eq. [2.25)] to allow for the possibility that the two atomic wavefunctions involved in its definition belong to different atoms:

$$n^{IJ\sigma}_{m_1,m_2} = \sum_{k,\nu} f^\sigma_{k\nu} \langle \psi^\circ_{\nu k\sigma} |\, | \phi^J_{m_2} \rangle \langle \phi^I_{m_1} |\, | \psi^\circ_{\nu k\sigma} \rangle \,. \tag{2.28}$$

In Eq. (2.28) the indexes m_1 and m_2 run over the angular momentum manifolds that are subjected to the Hubbard correction on atoms I and J respectively. It is important to notice that the occupation matrix defined in Eq. (2.28) contains information about all the atoms in the same unit cell and the on-site occupations defined in Eq. (2.25) correspond to its diagonal blocks ($\mathbf{n}^{I\sigma} = \mathbf{n}^{II\sigma}$).

For a complete expression of the DFT +U + V corrective functional, a double-counting term needs to be defined as well. Generalizing the FLL expression of the on-site double-counting term, Eq. (2.23), we arrive at the following expression:

$$E_{dc} = \sum_I \frac{U^I}{2} n^I (n^I - 1) + \sum_{I,J}^{*} \frac{V^{IJ}}{2} n^I n^J. \tag{2.29}$$

Subtracting Eq. (2.29) from (2.27) we finally obtain:

$$\begin{aligned} E_{UV} &= E_U + E_V - E_{dc} \\ &= \sum_{I,\sigma} \frac{U^I}{2} Tr[\mathbf{n}^{II\sigma}(\mathbf{1} - \mathbf{n}^{II\sigma})] - \sum_{IJ,\sigma}^{*} \frac{V^{IJ}}{2} Tr[\mathbf{n}^{IJ\sigma}\mathbf{n}^{JI\sigma}]. \end{aligned} \tag{2.30}$$

By looking at the Eq. (2.30) we can see that the two terms in the corrective energy functional, proportional to the on-site (U^I) and inter-site (V^{IJ}) couplings counteract each other.

In fact while the on-site term favors localization on atomic sites (typically suppressing hybridization), the inter-site one favors hybridized states with components on neighbor atoms. Computing the value of the U^I and V^{IJ} effective interaction parameters is thus crucial to determine the degree of atomic localization of d- and/or f-type electrons when the system is in its ground state.

The action of the Hubbard potential on KS wavefunctions can be obtained by taking the functional derivative of $E_{DFT+U+V}$ [see Eq. (2.20)] with respect to the complex conjugate of the same KS wavefunction [45]. The term corresponding to this functional derivative of E_{UV} [see Eq. (2.30)] is:

$$\hat{V}_{Hub,\sigma} = \sum_I \sum_{m_1 m_2} U^I \left(\frac{\delta_{m_1 m_2}}{2} - n^{I\sigma}_{m_1 m_2} \right) \hat{P}^I_{m_1 m_2} - \sum_I \sum_{J(J\neq I)} \sum_{m_1 m_2} V^{IJ} n^{IJ\sigma}_{m_1 m_2} \hat{P}^{IJ}_{m_1 m_2}. \quad (2.31)$$

This Hubbard potential is added to the standard DFT Hamiltonian, and then the modified KS equations are solved self-consistently.

The use of DFT+U+V instead of DFT+U is mainly motivated by the increased flexibility (variational freedom) the former offers compared to the latter. This is particularly important for more covalently-bonded systems where electronic localization occurs on hybridized states with components on neighbor atoms.

2.2.2 Hubbard projectors

The Hubbard projector functions, $\phi^I_{m_1}(\mathbf{r})$, can be constructed using different types of projector functions as a basis set. There are quite many possible projector functions to use as a basis for the Hubbard manifold, for example: nonorthogonalize and orthogonalized Wannier functions, linearized augmented plane-wave approaches, etc.

The most frequently used types of projectors, $P^{I\sigma}_{m_2,m_1}$, are atomic and ortho-atomic. Nevertheless, it is recommended the use of ortho-atomic whenever possible. The advantage of ortho-atomic over atomic is that the Hubbard corrections are applied only once in the former case, while in the latter case they are applied twice in the orbital overlap regions. So generally ortho-atomic Hubbard projectors give more accurate results (e.g. atomic occupations) than those obtained using the atomic Hubbard projectors.

In this work it will be used orthogonalized atomic orbitals. Orthogonalized atomic orbitals are obtained by taking atomic orbitals of each atom and then orthogonalizing them to all

the orbitals of all the atoms in the system. In this work, we will use the Löwdin orthogonalization method [46]. By doing so, a new set of orbitals is obtained that, by virtue of their mutual orthogonalization, provide a more accurate representation of inter-site hybridization. This choice is particularly appealing to define the Hubbard projectors, because it allows us to avoid counting Hubbard corrections twice in the interstitial regions between atoms. As explained in Ref. [47], the orthogonalized atomic orbitals with the Löwdin method are defined as [44]:

$$\phi^I_{m_1}(\mathbf{r}) = \sum_{Jm_2} \left(\langle \varphi^I_{m_1} | \, | \varphi^J_{m_2} \rangle^{-\frac{1}{2}} \right)^{JI}_{m_2 m_1} \varphi^J_{m_2}(\mathbf{r}), \tag{2.32}$$

where $\phi^I_{m_1}(\mathbf{r})$ and $\phi^J_{m_2}(\mathbf{r})$ are the nonorthogonalized atomic orbitals. It is important to orthogonalize not only states that belong to the chosen Hubbard manifolds of each atom (e.g., d or f-states), but also the remaining states, in order to preserve the on-site orthogonality.

2.2.3 Computing U from linear-response

Combining Eq. (2.20) and Eq. (2.30) we obtain [37]:

$$E = E_{DFT} + \frac{1}{2} \sum_{I,\sigma} U^I Tr[(1 - \mathbf{n}^{I\sigma})\mathbf{n}^{I\sigma}] - \frac{1}{2} \sum_{I,J,\sigma} V^{IJ} Tr[\mathbf{n}^{IJ\sigma}\mathbf{n}^{JI\sigma}]. \tag{2.33}$$

By choosing for the localized orbitals those whose representation diagonalizes the occupation matrices and considering only the E_U term we get:

$$\mathbf{n}^{I\sigma}\mathbf{v}^{I\sigma}_i = \lambda^{I\sigma}_i \mathbf{v}^{I\sigma}_i, \tag{2.34}$$

with $0 \leq \lambda^{I\sigma}_i \leq 1$, the energy correction becomes:

$$E_U[\{n^{I\sigma}_{m_1 m_2}\}] = \frac{U}{2} \sum_{I,\sigma} \sum_i \lambda^{I\sigma}_i (1 - \lambda^{I\sigma}_i), \tag{2.35}$$

from where it appears clearly that the energy correction introduces a penalty, tuned by the value of the U parameter, for partial occupation of the localized orbitals and thus favors disproportion in fully occupied ($\lambda \approx 1$) or completely empty ($\lambda \approx 0$) orbitals. This is the basic physical effect built in the DFT+U functional and its meaning can be traced back to known deficiencies of LDA or GGA for periodic systems.

Consistently with the definition and the intent of the Hubbard corrective functional, the U is

calculated from the spurious curvature of the (approximated DFT) total energy of the system as a function of the number of electrons of its localized (atomic) orbitals. Considering an atom in contact with the reservoir of electrons, it can exchange integer numbers of particles with its environment. The intermediate situation with fractional number of electrons in this open atomic system is described not by a pure state wavefunction, but rather by a statistical mixture so that, for instance, the total energy of a system with $N + \omega$ electrons (where N is an integer and $0 \leq \omega \leq 1$) is given by:

$$E_n = (1 - \omega)E_N + \omega E_{N+1}, \tag{2.36}$$

where E_N and E_{N+1} are the energies of the system corresponding to states with N and $N + 1$ particles respectively, while ω represents the statistical weight of the state with $N + 1$ electrons. The total energy of this open atomic system is thus represented by a series of straight-line segments joining states corresponding to integer occupations of the atomic orbitals. In fact, when the localized states exchange electrons with the rest of the crystal (acting like a charge reservoir), the total energy obtained from approximate DFT xc functionals varies in an analytic way and its derivative (the effective potential acting on them) misses or significantly underestimates the discontinuity at integer occupations that corresponds to the fundamental gap of the system. As demonstrated above and by quite abundant literature, Ref. [48, 49], the energy profile should consist, instead, of a series of straight segments joining the energies corresponding to integer occupations. A visual comparison between the exact (piece-wise linear) and the approximate energy (as functions of the localized states occupations) is made in Fig. (2.1) where the latter is modeled by a parabola. If the curvature of the approximate energy profile is assumed to be constant (actually a very good approximation within single intervals between integer occupations), the expression of the additive correction needed to recover the exact behavior [bottom line in the cartoon of Fig. (2.1)] can be easily worked out as the difference between a parabola and a straight line and results to have the same expression of the Hubbard correction in Eq. (2.24), provided the U is equal to the (spurious) curvature of the DFT energy profile. Hence, this addition of the Hubbard term will vanish from integer number of electrons and eliminates curvature of the approximate energy profile in every interval with fractional occupation. Therefore, the main objective of this calculation is to evaluate the second derivative of the total energy of the system with respect to the occupation of the localized states, as defined in Eq. (2.25) [50]. This clarifies the meaning of

the interaction parameter U as the (unphysical) curvature of the DFT energy as a function of N which is associated with the spurious self-interaction of the fractional electron injected into the system.

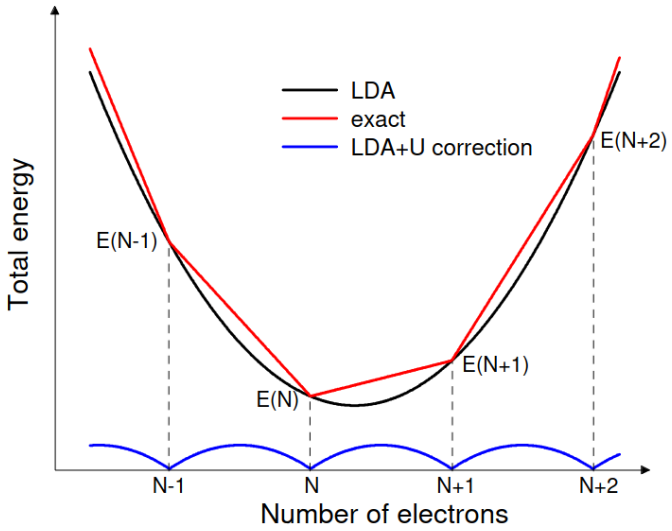

Figure 2.1: Sketch of the total energy profile as a function of the number of electrons in a generic atomic system in contact with a reservoir. The bottom curve is simply the difference between the other two (the LDA energy and the "exact" result for an open system). This figure has been taken from Ref. [37].

2.2.4 Hubbard parameters from DFPT

This section introduces a routine implemented in the DFT software we employed, named HP (Hubbard Parameter), which implements DFPT for the calculation of Hubbard parameters. The particularity of this method (DFPT) is that it constructs the localized perturbations (typically requiring costly calculations in supercells) as a series of independent monochromatic perturbations in the primitive unit cell, which improves the computational efficiency. This success comes from the fact that the perturbations will be expressed in the reciprocal space [44].

Hubbard parameters can be defined as the second derivatives of the total energy with respect to the total occupation of a given atom, i.e, with respect to the trace of the site-diagonal occupation matrix $n^{I\sigma}_{m_1 m_2}$.

In practice, the calculation of the energy second derivative can be achieved by perturbing the system with a shift in the potential acting on the Hubbard states of a given atom J, $\lambda^J \sum_m \hat{P}^J_{mm}$ (λ^J is the strength of the perturbation), and then computing the response of all the atomic occupations. Applying this to all the Hubbard atoms in the system allows to construct the bare and self-consistent susceptibility matrices that are obtained,

respectively, at the beginning of the perturbed run at its self-consistent convergence:

$$(\chi_0)_{IJ} = \frac{dn_0^I}{d\lambda^J}, \quad (\chi)_{IJ} = \frac{dn^I}{d\lambda^J} \tag{2.37}$$

Here, $n^I = \sum_{m\sigma} n^{I\sigma}_{mm}$ and similar definition holds for n^I_0. From these, the effective Hubbard parameters can be readily obtained [45]:

$$U^I = (\chi_0^{-1} - \chi^{-1})_{II} \tag{2.38}$$

$$V^{IJ} = (\chi_0^{-1} - \chi^{-1})_{IJ} \tag{2.39}$$

Within the framework of DFPT, the response of the KS wavefunctions to a small perturbation of the atomic potential:

$$\left(\hat{H}_\sigma + \lambda^J \hat{V}^J_{\text{pert}}\right) |\psi_{\nu\mathbf{k}\sigma}\rangle = \varepsilon_{\nu\mathbf{k}\sigma} |\psi_{\nu\mathbf{k}\sigma}\rangle \tag{2.40}$$

is obtained as the self-consistent solution of the perturbative problem resulting from a first-order perturbation theory of the KS equations in terms of λ^J:

$$(\hat{H}^\circ_\sigma - \varepsilon^\circ_{\nu\mathbf{k}\sigma}) \, |\frac{d\psi_{\nu\mathbf{k}\sigma}}{d\lambda^J}\rangle = -\left(\frac{d\hat{V}_{\nu\mathbf{k}\sigma}}{d\lambda^J} - \frac{d\varepsilon_{\nu\mathbf{k}\sigma}}{d\lambda^J} + \hat{V}^J_{pert}\right) |\psi_{\nu\mathbf{k}\sigma}\rangle \tag{2.41}$$

where $\hat{H}^\circ_\sigma = \hat{H}^\circ_{DFT,\sigma} + \hat{V}^\circ_{Hub,\sigma}$ is the total Hamiltonian of DFT+U+V, where $\hat{H}^\circ_{DFT,\sigma}$ is the Hamiltonian of standard DFT, and $\hat{V}^\circ_{Hub,\sigma}$ is the corrective Hubbard potential. $\varepsilon^\circ_{\nu\mathbf{k}\sigma}$ and $\psi_{\nu\mathbf{k}\sigma}$ are the KS energies and wavefunctions of the unperturbed system in the DFT+U+V framework. In Eq. (2.41) and hereafter, with the superscript "$\circ$" we indicate quantities which refer to the unperturbed ground state of the system. $\hat{V}^J_{\text{pert}} = \sum_m \hat{P}^J_{mm}$ is the perturbing potential; $\frac{d\hat{V}_{\text{Hxc},\sigma}}{d\lambda^J}$, $\frac{d\psi_{\nu\mathbf{k}\sigma}}{d\lambda^J}$ and $\frac{d\varepsilon_{nu\mathbf{k}\sigma}}{d\lambda^J}$ are the response Hartree and xc (Hxc) potential, response KS wavefunctions, and response KS energies. If the LR KS equations [see Eq. (2.41)] are solved starting from the DFT+U+V ground state with U$\neq 0$ and V$\neq 0$, then the response of the Hubbard potential, $\frac{d\hat{V}_{Hub,\sigma}}{d\lambda^J}$ must be set to zero. As a consequence, this term is not present on the right-hand side of Eq. (2.41). The problem has to be solved self-consistently because the response of the KS eigenvalues and of the Hxc potential, appearing on the right-hand side of Eq. (2.41), depend on the response of the KS wavefunctions, obtained from the solution of the perturbative problem of the above mentioned equation. Once convergence is achieved, the variation of the diagonal (with respect to atomic sites) atomic occupation matrices [that define the self-consistent susceptibility matrix in Eq. (2.37)] are obtained:

$$\frac{dn^{I\sigma}_{m_1m_2}}{d\lambda^J} = \sum_{\mathbf{k}}^{N_\mathbf{k}}\sum_{\nu} f_{\nu k\sigma}\left[\langle\psi^\circ_{\nu\mathbf{k}\sigma}|\,\hat{P}^I_{m_2m_1}\,|\frac{d\psi_{\nu\mathbf{k}\sigma}}{d\lambda^J}\rangle + \langle\frac{d\psi_{\nu\mathbf{k}\sigma}}{d\lambda^J}|\,\hat{P}^I_{m_2m_1}\,|\psi^\circ_{\nu\mathbf{k}\sigma}\rangle\right] + \sum_{\mathbf{k}}^{N_\mathbf{k}}\sum_{\nu}\frac{df_{\nu k\sigma}}{d\lambda^J}\,\langle\psi^\circ_{\nu\mathbf{k}\sigma}|\,\hat{P}^I_{m_2m_1}\,|\psi^\circ_{\nu\mathbf{k}\sigma}\rangle \tag{2.42}$$

If the LR KS equations (2.41) are solved starting from the DFT +U ground state with $U \neq 0$, then the response of the Hubbard potential, $\frac{d\hat{V}_{\mathrm{Hub},\sigma}}{d\lambda^J}$ must be set to zero. This is a consequence of the fact that U is defined as the curvature of the DFT part of the total energy as a function of atomic occupations. Keeping $\hat{V}_{\mathrm{Hub},\sigma}$ (the first derivative of the Hubbard energy) fixed to its unperturbed value $\hat{V}^\circ_{\mathrm{Hub},\sigma}$ avoids that the second derivative of the total energy contains a finite contribution from the Hubbard correction. As a consequence, this term is not present on the right-hand side of Eq. (2.41). It is well known in DFPT that only the component of the LR KS wavefunctions obtained by projection on the empty (conduction) states manifold yields a non-zero contribution to the LR spin charge density and LR occupation matrices (2.42). Therefore, it is convenient to work directly with the projection of Eq. (2.41) onto this manifold:

$$(\hat{H}^\circ_\sigma + \alpha\hat{\mathcal{O}}_\sigma - \varepsilon^\circ_{\nu\mathbf{k}\sigma})\left|\frac{d\tilde{\psi}_{\nu\mathbf{k}\sigma}}{d\lambda^J}\right\rangle = -\hat{\mathcal{P}}_\sigma\left(\frac{d\hat{V}_{\mathrm{Hxc},\sigma}}{d\lambda^J} + \hat{V}^J_{\mathrm{pert}}\right)|\psi^\circ_{\nu\mathbf{k}\sigma}\rangle \tag{2.43}$$

In Eq. (2.43), $\hat{\mathcal{O}}_\sigma$ is the projector on the occupied states manifold: $\hat{\mathcal{O}}_\sigma = \sum_{\mathbf{k}'}^{N_\mathbf{k}}\sum_{\nu'}^{N_{\mathrm{occ}}} |\psi^\circ_{\nu'\mathbf{k}'\sigma}\rangle\langle\psi^\circ_{\nu'\mathbf{k}'\sigma}|$, while the operator $\hat{\mathcal{P}}_\sigma$ is the projector on the empty state manifold, and it is expressed using the identity relation $\hat{\mathcal{P}}_\sigma = \hat{\mathcal{O}}_\sigma$, in order to avoid sums over the empty states that would typically. be very slow converging with respect to the number of states. In Eq. (2.43), $|\frac{d\tilde{\psi}_{\nu\mathbf{k}\sigma}}{d\lambda^J}\rangle = \hat{\mathcal{P}}_\sigma\,|\frac{d\psi_{\nu\mathbf{k}\sigma}}{d\lambda^J}\rangle$ is the conduction component of the LR KS wavefunctions. The extra term $\alpha\hat{\mathcal{O}}_\sigma$ on the left-hand side of Eq. (2.43) is not strictly required by the projection on conduction states: Its presence serves the purpose of lifting the singularity of the operator $\hat{H}^\circ_\sigma - \varepsilon^\circ_{\nu\mathbf{k}\sigma}$ on the valence manifold which would create numerical issues when solving it. For this purpose the parameters α is fixed to twice the spread of the unperturbed KS spectrum: $\alpha = 2(\max[\varepsilon^\circ_{\nu\mathbf{k}\sigma}] - \min[\varepsilon^\circ_{\nu\mathbf{k}\sigma}])$, which made the operator on the left-hand side of Eq. (2.43) nonsingular. In practice, if Eq. (2.43) is solved using iterative algorithms and the trial solution is chosen orthogonal to the occupied states manifold, then the orthogonality is preserved during the iteration cycle and there is no need of the extra term $\alpha\hat{\mathcal{O}}_\sigma$ on the left-hand side os Eq. (2.43). In terms of the term $\frac{d\varepsilon_{\nu\mathbf{k}\sigma}}{d\lambda^J}$ appearing in Eq. (2.41), it disappeared from Eq. (2.43) because $\hat{\mathcal{P}}_\sigma\,|\psi^\circ_{\nu\mathbf{k}\sigma}\rangle = 0$ for valence states.

This means that variations of the valence KS energies (due to the perturbation) do not contribute to the conduction component of the LR KS wavefunctions. The expressions for the LR occupation matrices, Eq. (2.42), and spin charge densities remain identical, if we replace $|\frac{d\psi_{v\mathbf{k}\sigma}}{d\lambda^J}\rangle$ by $|\frac{d\tilde{\psi}_{v\mathbf{k}\sigma}}{d\lambda^J}\rangle$.

2.2.5 From localized perturbations in supercells to monochromatic perturbations in primitive unit cells

A supercell of size $L_1 \times L_2 \times L_3$ is defined, having lattice vectors A_i that are integer multiples of those of the primitive unit cell a_i:

$$\mathbf{A}_i = L_i \mathbf{a}_i \tag{2.44}$$

where i=1,2,3. Let $\mathbf{B}_i$ be the reciprocal lattice basis vectors of this supercell. Based on their definition, it is easy to determine the relationship with the reciprocal lattice vectors $\mathbf{b}_i$ of the primitive unit cell:

$$\mathbf{B}_i = 2\pi \frac{\mathbf{A}_j \times \mathbf{A}_k}{V} = 2\pi \frac{\mathbf{a}_j \times \mathbf{a}_k}{L_i v} = \frac{\mathbf{b}_i}{L_i} \tag{2.45}$$

$$\mathbf{G}_{klm} = k\mathbf{B}_1 + l\mathbf{B}_2 + m\mathbf{B}_3 \tag{2.46}$$

$$\mathbf{G}_{klm} = \frac{k}{L_1}\mathbf{b}_1 + \frac{l}{L_2}\mathbf{b}_2 + \frac{m}{L_3}\mathbf{b}_3 + \tag{2.47}$$

$$k = k' L_1 + \bar{k} \tag{2.48}$$

$$l = l' L_2 + \bar{l} \tag{2.49}$$

$$m = m' L_3 + \bar{m} \tag{2.50}$$

$$\mathbf{G}_{klm} = \mathbf{g}_{k'l'm'} + \mathbf{q}_{\bar{k}\bar{l}\bar{m}} \tag{2.51}$$

$$\mathbf{g}_{k'l'm'} = k'\mathbf{b}_1 + l'\mathbf{b}_2 + m'\mathbf{b}_3 \tag{2.52}$$

$$\mathbf{q}_{\bar{k}\bar{l}\bar{m}} = \frac{\bar{k}}{L_1}\mathbf{b}_1 + \frac{\bar{l}}{L_2}\mathbf{b}_2 + \frac{\bar{m}}{L_3}\mathbf{b}_3 \tag{2.53}$$

Fourier expansion of the perturbing localized potential in a supercell:

$$V(\mathbf{r}) = \sum_{\mathbf{G}} e^{i\mathbf{G}\cdot\mathbf{r}} V(\mathbf{G}) \tag{2.54}$$

$$= \sum_{klm} e^{i\mathbf{G}_{klm}\cdot\mathbf{r}} V(\mathbf{G}_{klm}) \tag{2.55}$$

We can rewrite this potential as a sum of monochromatic perturbations ($\mathbf{G} = \mathbf{g} + \mathbf{q}$):

$$V(\mathbf{r}) = \sum_{\bar{k}\bar{l}\bar{m}} \sum_{k'l'm'} e^{i(\mathbf{g}_{k'l'm'} + \mathbf{q}_{\bar{k}\bar{l}\bar{m}}]\cdot\mathbf{r}} V(\mathbf{g}_{k'l'm'} + \mathbf{q}_{\bar{k}\bar{l}\bar{m}}) \quad (2.56)$$

$$= \sum_{\mathbf{q}} \sum_{\mathbf{g}} e^{i(\mathbf{q}+\mathbf{q})\cdot\mathbf{r}} V(\mathbf{q}+\mathbf{q}) \quad (2.57)$$

$$= \sum_{\mathbf{q}} e^{i\mathbf{q}\cdot\mathbf{r}} \bar{V}_{\mathbf{q}}(\mathbf{r}) \quad (2.58)$$

$$\bar{V}_{\mathbf{q}}(\mathbf{r}) = \sum_{\mathbf{r}} e^{i\mathbf{g}\cdot\mathbf{r}} V(\mathbf{g}+\mathbf{q}) \quad (2.59)$$

2.2.6 Monochromatic perturbations in DFPT

The major advantage offered by the DFPT consists in the possibility to obtain the variation of atomic occupations as a sum of wavevector-specific contributions that can be computed independently from one another (thus leading to a more efficient computation) using the primitive unit cell of the system. In fact, the Fourier spectrum of a perturbation that has the periodicity of a supercell (as needed to eliminate the interactions with periodic replicas) only contains fundamental vectors of its reciprocal lattice that map into a corresponding q points grid within the Brillouin Zone (BZ) corresponding to the primitive cell. The total response of atomic occupations can thus be written as [51]:

$$\frac{dn^{sl\sigma}_{m_1m_2}}{d\lambda^{s'l'}} = \frac{1}{N_{\mathbf{q}}} \sum_{\mathbf{q}}^{N_{\mathbf{q}}} e^{i\mathbf{q}\cdot(\mathbf{R}_l - \mathbf{R}_{l'})} \Delta^{s'}_{\mathbf{q}} \bar{n}^{s\sigma}_{m_1m_2} \quad (2.60)$$

where the atomic site indices I and J have been decomposed as $I = (l, s)$ and $J = (l', s')$ indicating, respectively, the cell the atom belongs to (l and l') and its position within the cell (s and s'). Here, N_q is the number of $\mathbf{q}$ points in the first BZ (note that the dimension of the q points grid reflects directly that of the supercell it is the reciprocal-space image of). Hereafter, we use the over-bar to indicate lattice-periodic parts of the ground-state and response quantities. $\Delta^{s'}_{\mathbf{q}} \bar{n}^{s\sigma}_{m_1m_2}$ represents the lattice-periodic response of the occupation matrix to a monochromatic perturbation with a wavevector $\mathbf{q}$, and it can be linked to the lattice-periodic variations of the KS wavefunctions as follows [44]:

$$\Delta^{s'}_{\mathbf{q}} \bar{n}^{s\omega}_{m_1m_2} = \frac{1}{N_{\mathbf{k}}} \sum_{\mathbf{k}}^{N_{\mathbf{k}}} \sum_{\nu}^{N_{\text{occ}}} [\langle \bar{u}^{\circ}_{\nu\mathbf{k}\sigma} | \hat{\bar{P}}^{s}_{m_2,m_1,\mathbf{k},\mathbf{k+q}} | \Delta^{s'}_{\mathbf{q}} \bar{u}_{\nu\mathbf{k}\sigma} \rangle + \langle \bar{u}^{\circ}_{\nu\mathbf{k}\sigma} | \hat{\bar{P}}^{s}_{m_1,m_2,\mathbf{k},\mathbf{k+q}} | \Delta^{s'}_{\mathbf{q}} \bar{u}_{\nu\mathbf{k}\sigma} \rangle] \quad (2.61)$$

Here, $\bar{u}^{\circ}_{\nu\mathbf{k}\sigma}$ and $\Delta^{s'}_{\mathbf{q}} \bar{u}_{\nu\mathbf{k}\sigma}$ are the lattice-periodic parts of the unperturbed and LR monochromatic $\mathbf{q}$ component on the KS wavefunctions, respectively. The lattice-periodic part of the projector on the Hubbard manifold, which appears in Eq. (2.61), reads:

$$\hat{\bar{P}}^{s}_{m_2,m_1,\mathbf{k},\mathbf{k+q}} = |\bar{\varphi}^{s}_{m_2,\mathbf{k}}\rangle \langle \bar{\varphi}^{s}_{m_1,\mathbf{k+q}}| \quad (2.62)$$

The two terms on the right-hand side of Eq. (2.61) were made look similar (except for the inversion in the order of indices m_1 and m_2) but the use of time-reversal symmetry. In DFPT, the composition of LR KS wavefunctions obtained by projection on the empty (conduction) states manifold gives a non-zero contribution to the LR spin charge density and LR occupation matrices [see Eq. (2.42)]. Therefore, it is convenient to work directly with the projection of Eq. (2.41) onto this manifold [45, 52]:

$$(\hat{\hat{H}}^{\circ}_{\mathbf{k+q},\sigma} + \alpha\hat{\hat{O}}_{\mathbf{k+q},\sigma} - \varepsilon^{\circ}_{\nu\mathbf{k}\sigma})\,|\Delta^{s'}_{\mathbf{q}}\bar{u}_{\nu\mathbf{k}\sigma}\rangle = -\hat{\hat{\mathcal{P}}}_{\mathbf{k+q},\sigma}(\Delta^{s'}_{\mathbf{q}}\hat{\hat{V}}_{H_{xc},\sigma} + \hat{\hat{V}}^{s}_{\text{pert},\mathbf{k+q},\mathbf{k}})\,|\bar{u}^{\circ}_{\nu\mathbf{k}\sigma}\rangle\,, \tag{2.63}$$

where the perturbing potential reads:

$$\hat{\hat{V}}^{s}_{\text{pert},\mathbf{k+q},\mathbf{k}} = \sum_{m}\hat{\hat{P}}^{s}_{m,m,\mathbf{k+q},\mathbf{k}} \tag{2.64}$$

The quantities $\hat{\hat{H}}^{\circ}_{\mathbf{k+q},\sigma}$ and $\Delta^{s'}_{\mathbf{q}}\hat{\hat{V}}_{H_{xc},\sigma}$ are, respectively, the lattice-periodic parts of the unperturbed Hamiltonian $\hat{H}^{\circ}_{\sigma}$ (which contains the Hubbard corrective potential with on-site U and inter-site V) and response H_{xc} potential for a specific **q**. The response H_{xc} potential $\Delta^{s'}_{\mathbf{q}}\hat{\hat{V}}_{H_{xc},\sigma}$ depends on the response spin charge density at the same **q**, $\Delta^{s'}_{\mathbf{q}}\bar{\rho}_{\sigma}(\mathbf{r})$, which in turn depends on $\Delta^{s'}_{\mathbf{q}}\bar{u}_{\nu\mathbf{k}\sigma}(\mathbf{r})$. The operators $\hat{\hat{O}}_{\mathbf{k+q},\sigma}$ and $\hat{\hat{\mathcal{P}}}_{\mathbf{k+q},\sigma}$ are the lattice-periodic parts of projectors on the valence and conduction manifolds, respectively:

$$\hat{\hat{O}}_{\mathbf{k+q},\sigma} = \sum_{\nu'}^{N_{\text{occ}}}|\bar{u}^{\circ}_{\nu'\mathbf{k+q}\sigma}\rangle\,\langle\bar{u}^{\circ}_{\nu'\mathbf{k+q}\sigma}| \tag{2.65}$$

$$\hat{\hat{\mathcal{P}}}_{\mathbf{k+q},\sigma} = 1 - \sum_{\nu'}^{N_{\text{occ}}}|\bar{u}^{\circ}_{\nu'\mathbf{k+q}\sigma}\rangle\,\langle\bar{u}^{\circ}_{\nu'\mathbf{k+q}\sigma}| \tag{2.66}$$

The extra term $\alpha\hat{\hat{O}}_{\sigma}$ on the left hand side of Eq. (2.63) is not strictly required by the projection on conduction states. Its presence serves the purpose of lifting the singularity of the operator $\hat{H}^{\circ}_{\sigma} - \varepsilon^{\circ}_{\nu\mathbf{k}\sigma}$ on the valence manifold which would create numerical issues when solving it. In Eq. (2.63) $\alpha$is fixed to twice the spread of the unperturbed KS sprectrum: $\alpha = 2(\max[\varepsilon^{\circ}_{\nu\mathbf{i}\sigma}] - \min[\varepsilon^{\circ}_{\nu\mathbf{i}\sigma}])$, where $\max[\varepsilon^{\circ}_{\nu\mathbf{i}\sigma}]$and $\min[\varepsilon^{\circ}_{\nu\mathbf{i}\sigma}]$ which makes the operator on the left-hand side of Eq. (2.63) non-singular. The operator $\hat{\hat{O}}_{\mathbf{k+q},\sigma}$ is inserted on the left-hand side of Eq. (2.63) in order to avoid singularity issues during the iterative solution at the same time the operator $\hat{\hat{\mathcal{P}}}_{\mathbf{k+q},\sigma}$ avoids sums over empty states that would, typically, be very slow converging with respect to the number of states Note that due to the presence of the projector $\hat{\hat{\mathcal{P}}}_{\mathbf{k+q},\sigma}$ in Eq. (2.63) the derivative of the KS eigenvalues disappears from the right-hand side of Eq. (2.63) in comparison to Eq. (2.41). The KS eigenvalues at **k+q** points, $\bar{u}^{\circ}_{\nu'\mathbf{k+q}\sigma}(\mathbf{r})$ which are present in Eqs. (2.66) and (2.66) are obtained by solving non-self-consistent the KS equations and using the unperturbed ground-state spin

charge density $\bar{\rho}^{\circ}_{\sigma}(\mathbf{r})$. All the operators in Eq. (2.63) appear with a specific **q** component as a result of recasting Eq. (2.41) in reciprocal space through the Bloch sums of all the quantities appearing in there. The potential terms appearing on the right-hand side of Eq. (2.63) represent the lattice-periodic components of the corresponding potential variations at the indicated wavevector **q**. Once these equations are solved self-consistently for all wavevectors, Eqs. (2.60) and (2.61) are used to compute the susceptibility matrices using Eq. (2.37), from which the Hubbard interaction parameters are readily obtained as indicated in Eqs. (2.39) and (2.39).

2.2.6.1 Other methods

Various other more chemically accurate xc functionals have been devised to deal with SIE, in particular through so-called hybrid functionals - such as e.g. B3LYP [53] or HSE06 [54, 55]. Hybrid functionals were formulated to include a linear combination of a number of xc explicit density and HF exact exchange functionals, that is self-interaction free, by eliminating the extra self-interaction of electrons through the explicit introduction of a Fock exchange term. But since the Fock exchange is a non-local integral operator which acts on KS wavefunctions, this approach is computationally more expensive than DFT. Another recent suggestion is the meta - GGA, for example the strongly constrained and appropriately normed semilocal density functional (SCAN) [56], which has shown promising results for many systems. Having a marginal increase in the computational cost, DFT with the SCAN functional uses a xc potential which depends on KS wavefunctions via a kinetic energy density. However, SCAN still contains significant SIE.

2.3. Structural, electronic and magnetic properties

2.3.1 Magnetic Properties of $Pr_2O_2SO_4$

When a material undergoes distortion in its crystal structure, it can impact the properties of the compound, such as changes in exchange interactions, electronic structure change, magnetic frustration, and domain structure. Understanding the interplay between crystal structure, electronic configuration, and magnetic interactions is crucial for predicting and controlling the magnetization properties of materials in distorted systems.

Little is yet known about the crystalline ground-state symmetry of $Pr_2O_2SO_4$. Moreover, since the magnetic states have not been experimentally analysed, one needs to perform spin-polarized calculations to assess the ground-state magnetic ordering. We will therefore compute, analyse and compare the energies of the antiferromagnetic (AF) and

ferromagnetic (F) states of the different crystalline structures, in order to assess whether there is any magnetic ordering and, if so, which will be the most stable ordering.

Atoms with partially filled d- or f-states are magnetic, and the method of DFT is less accurate. In this case, one defines separate densities for spin-up and spin-down electrons, and writes coupled equations to relate these two densities. The exchange energy is only between electrons of the same spin polarization.

According to this, praseodymium is known to exhibit a magnetic moment due to its partially filled $4f$-electron shell. The magnetic moment of Pr depends on the valence state of Pr (2+, 3+ or 4+). The largest (theoretical) value obtained for Pr(3+) is 3.87. In terms of the experimental value, it is generally lower than this [57].

By default, a QE calculation is spin-unpolarized (non-magnetic). It means that every KS orbital is occupied by two electrons, one with spin-up and one with spin-down. Therefore, the total spin moment for the crystal is necessarily zero. To do spin-polarized (with magnetic ordering) calculations we have to change the method. In terms of the input file, the parameters that control the magnetization are nspin and $\mathrm{starting\_magnetization(i)}$. The default value for nspin is 1 and correspond to a non-polarized calculation. However, when it takes the value 2 it corresponds to a spin-polarized calculation, with magnetization along z axis. In a crystal with more than one type of atoms in the unit cell, it is possible to control which elements are spin-polarized and which are not. The variable i in $\mathrm{starting\_magnetization(i)}$ can have an absolute value greater than or equal to 1 and will be interpreted as the site's magnetic moment, while the value of the parameter can range between -1 and 1, is interpreted as the initial site magnetization per valence electron at the start of the selfconsitent cycle. A value of +1 means that the spin moment is maximally positive. This parameter $\mathrm{starting\_magnetization(i)}$ is ignored in most, but not all cases of non self consistent field calculations. So it is important to keep this information when it is expected a nonzero magnetization in the ground state. After the spin-polarized calculation, we can find in the output file two important quantities:$\mathrm{total\ magnetization}$ and $\mathrm{absolute\ magnetization}$. The $\mathrm{total\ magnetization}$ is computed as the integral of the absolute value of the magnetization in the cell: $M_{Tot} = \int_{cell} \left(n_{up} - n_{dw} \right) d^3r$ while the $\mathrm{absolute\ magnetization}$ corresponds to the integral of the absolute value of the magnetization in the cell: $M_{Abs} = \int_{cell} |n_{up} - n_{dw}| d^3r$. After realizing the self consistent field (SCF) calculations it is also possible to change the parameter $\mathrm{starting\_magnetization(i)}$ to the parameter

$\mathrm{tot\_magnetization}$ that is used to impose a specific total electronic magnetization determined during the self-consistent cycle, and specifically important for insulating systems. These quantities are computed in Bohr magnetons per cell.

When it comes to the nature of magnetic ordered states of crystals containing magnetic ions, there is a rich variety of in-principle possible ordered states, such as: ferromagnetic, ferrimagnetic, antiferromagnetic, spin spirals, non-collinear magnetism.

In ferromagnetic ordering, we have more electrons in a spin-up or spin-down state which originates a spin magnetic moment in the atom, but all the symmetry equivalent atoms have the same spin magnetic moment. In this case, the value of the $\mathrm{total\ magnetization}$ and the $\mathrm{absolute\ magnetization}$ should be equal after the spin-polarized calculation.

In antiferromagnetic ordering, we have half of the atoms with a spin magnetic moment pointing in one direction while the other half with their spin magnetic moments pointing in the opposite direction. In this case, the value of the $\mathrm{absolute\ magnetization}$ is zero and the value of $\mathrm{total\ magnetization}$ is twice the magnetization of each of the two atoms. Three types of antiferromagnetic order prevalent in oxide crystals, and which we will scrutinize for out target compounds, are shown in Fig. (2.2). The antiferromagnetic interplanar and ferromagnetic intraplanar coupling leads to the A-type, while the opposite situation (AF intraplanar and F interplanar coupling) gives the C-type. When both interactions are antiferromagnetic, it will lead to the G-type [58, 59].

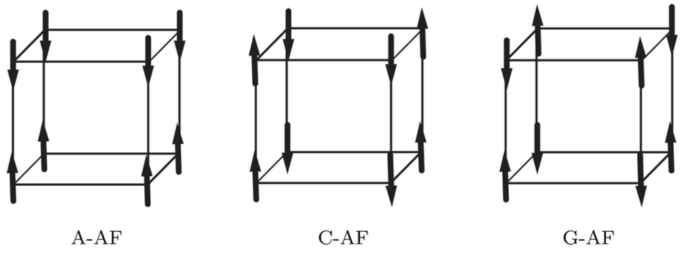

Figure 2.2: Three types of antiferromagnetic (AF) structures, A- AF, C- AF, and G- AF.

2.3.2 Bader charge analysis

Bader's theory of atoms in molecules is often useful for analyse the charge densities and is based on the Quantum Theory of Atoms in Molecules (QTAIM). The charge that is enclosed within the Bader's volume is a good approximation to the total electronic charge of an atom. The charge distribution can be used to determine multipole moments of interacting atoms or molecules. Such an analysis can also be considered to define the hardness of atoms, which can be used to quantify the cost of removing a charge from an

atom (ion). The theory also provides a definition for chemical bonding that gives numerical values for bond strength, such as the bond critical points, which is represented by a scalar field (Bader's topology), or attraction basins of the maxima and respective integrating quantities (Bader's atomic charges) [60, 61].

While partitioning the electronic density into contributions from separate atoms is an arbitrary process, a number of partitioning schemes have been developed that have proved helpful in predicting specific chemical properties of interest, such as nominal oxidation states. One popular method is the Bader partitioning, where the electron density is divided at zero flux surfaces. One of its advantages is that the results depend little on the employed basis set. To perform the Bader partitioning, we need to prepare both the all-electron density and the valence electron density [62, 63].

3. Computational Implementation

This chapter is dedicated to the method and the software used to perform the calculations required and where DFT is implemented. Throughout this chapter it will be explained the development of the input files required for Quantum Espresso to calculate the requested system and respective properties, as well as the several options and choices made in order to calculate numerically meaningful results, rather than random noise and obtain physical correct results. The main choices are related to the cell parameters, the type of material (metal or insulator) and the type of relaxation of the structure. Lastly it was presented the Birch-Murnaghan equation of state to study the relation between the energy and the volume of the crystal, and obtain the Bulk Modulus of the different studied systems.

3.1. The Quantum Espresso software

Some of the most used softwares where DFT is implemented are Quantum ESPRESSO [64], VASP [65], ABINIT [66], SIESTA[67, 68]. The software suit employed throughout this work was Quantum Espresso (QE), therefore will be the only code described here.

QE is an integrated Open-Source software to perform structural and electronic calculations at an atomistic and first principles perspective. It is based on the DFT framework, and uses plane-waves to expand the KS wavefunctions, and pseudopotentials to treat the nuclei and core electrons. The standard QE allows the computation of self-consistent total energies, forces, stresses, KS orbitals, noncollinear magnetism, SOC effects, and much more [64]. For every DFT calculation that is implemented it is important to converge several parameters for each system, to guarantee that we are able to obtain numerically meaningful results.

Pseudopotential type — The Coulomb potential (first term of Eq. (2.13)) can be treated in the form of an effective potential consisting of the inner core electrons and nucleus. These form an inert core region which interact with the valence electrons [69], i.e. those which are mostly responsible for the chemical bonding between atoms.

During this project, it was used the Projector augmented-wave (PAW) method [70]. This method introduces a linear transformation from the pseudo wavefunction to the all-electron wavefunction (KS single particle wavefunction), operating directly on the full

valence and core wavefunctions. PAW can be used to treat first-row and transition-metal elements with affordable basis-sets while providing access to the full all-electron wavefunction, and thus to a higher accuracy for a given level of optimization. The PAW potentials are generally very accurate, not only because the radial cut-offs are small, but also because the PAW potentials reconstruct the exact valence wavefunction with all nodes in the core region.

The concept of augmented-wave methods is to divide the wavefunction into two parts, namely, a partial-wave expansion within an atom-centred sphere and envelope functions outside the spheres. The envelope function is expanded into plane-waves or other types of basis functions (i.e. Hankel functions). Envelope function and partial-wave expansions (and respective derivatives) are then matched at the sphere boundary radius.

Exchange-correlation functional choice — DFT essentially only is approximated in the choice of the xc functional. The choice of this functional will determine, in a rather unpredictable way, how much the final results will deviate from the (unknown) true results. There are several options like: LDA, GGA, meta- GGA, hybrid functionals. To select a functional it is important to search the literature for calculations on similar materials and on properties computed in a way to compare the strengths and weaknesses with respect to the types of calculations we want to compute.

Basis set size choice — The KS wavefunctions can be expanded using different basis-sets. The most natural method to treat periodic systems is by expanding these as plane-waves. Within a numerical implementation, such an infinite basis-set has to be truncated, which limits the precision of the calculation. Ideally, the basis set should be truncated only after the point where adding more basis functions does not notably influence the electronic energy any longer. In QE, the basis set size is specified by the `ecutwfc` keyword in the &SYSTEM block of the input file. In order to describe the density, another parameter has to be set, and determined by the variable `ecutrho`. By default, `ecutrho` is $4\times$ `ectuwfc`. However, this factor 4 might require adjustment depending on the used pseudopotential dataset. This factor 4 might need to be somewhat larger for PAW pseudopotentials, and much larger (8-12) for ultrasoft pseudopotentials. A good strategy is to test which value of `ecutwfc` is needed (keeping `ecutrho` 4 times larger), and afterwards, once the final `ecutwfc` is reached, `ecutrho` can be increased further until the relative energy differences do not show significant variations.

k-mesh — For periodic systems, care must be taken when defining the sampling of the

BZ. In order to numerically solve integration over wavefunctions (**k**-points), we have to define the density of the **k**-point mesh. The more dense these **k**-points are, the better the numerical solution is in terms of the exact one. Therefore, for each crystal structure it is mandatory to verify whether one has a sufficiently adequate sampling mesh. Such a mesh is much more sensitive for low band-gap systems. We can assess the adequate sampling mesh by plotting calculated quantities (like electronic energy) as a function of the number of sampling points, to observe how these evolve as a function of **k**-mesh density. As soon as these properties do not depend any longer on the density of the mesh, we have the result that corresponds to an “infinitely” dense mesh (i.e we have attained a numerically accurate result).

Geometry optimization— In order to obtain the equilibrium properties (volume and lattice parameters, energies, bulk modulus and its pressure derivative), the energy-volume ($E-V$) curves can be fitted to a third-order Birch-Murnaghan equation of state [71] - more details in Appendix C. We have however considered a complete structural relaxation, varying both the atomic positions and lattice constants, directly by using the appropriate algorithm in QE.

3.2. Computational Details

By using first-principles techniques, we want to compute and characterize the different polymorphs [orthorhomic $I222$ (#23), monoclinic $C2/c$ (#15) or tetragonal $I\overline{4}2m$ (#121)] and define respective energetic stability.

Throughout the course of the dissertation project I will be using the GGA [33] with the PBE parametrization [33] as the xc functional.

PAW datasets are applied to treat core electrons interactions with the valence states (O.pbe-n-kjpaw-psl.1.0.0.UPF, Pr.pbe-spdfn-kjpaw-psl.1.0.0.UPF and S.pbe-n-kjpaw-psl.1.0.0.UPF), which yield the following configuration: O ($2s^2\ 2p^4$), Pr ($4f^3\ 6s^2$), S ($3s^2\ 3p^4$).

The energy-cutoff for the expansion of the electronic plane-wave basis sets and for charge density and potential were set to 116 and 696 Ry, respectively.

The **k**-point sampling in the BZ was performed using the centered Monkhorst–Pack scheme [72, 73], and converged according to the symmetry of the systems: $8\times8\times6$ ($C2/c$), $8\times8\times8$ ($I\overline{4}2m$) and $8\times8\times6$ ($I222$) to perform the structural relaxations and $18\times18\times16$ ($C2/c$) $18\times18\times18$ ($I\overline{4}2m$) and $18\times18\times16$ ($I222$) to perform the projected

and total density of states. The number of sampling points is expressed as a three-dimensional grid in reciprocal space ("**k**-mesh"), and is set inside the &ELECTRONS block with the K_POINTS keyword. The labeling of the BZ high-symmetry points were determined using the SEEK-PATH web tool [74].

The property used to check for convergence, was the total electronic energy and it would be considered converged with respect to **k**-mesh density and the cutoff of the basis sets if the difference between two SCF calculations was of the order of $\sim$1 eV.

The total energy was set to be less that 10^{-5} eV/atom for self-consistent convergence (the convergence criterion for ionic minimization is satisfied when the total energy changes less than `etot_conv_thr` between two consecutive SCF steps) and the highest force on the atom was set to be less than 10^{-4} (eV/Å) for ionic minimization (the convergence criterion is satisfied when all components of all forces are smaller than `forc_conv_thr`).

In terms of the Hubbard projectors, we used the orthogonalized atomic orbitals. For more details an example of a input file is detailed in the Appendix B.

3.2.1 Cell parameters

To specify lattice parameters and atomic positions of the crystal, there are several options to proceed. We can use the variable of `ibrav` that specifies the Bravais lattice and then one defines the parameters [`celldm`(1)-`celldm`(6)] or [A, B, C, cosAB, cosAC, cosBC]. The lattice parameter "alat" is set to alat = celldm(1) (in a.u.) or alat = A (in Å). On the other side, we can also set `ibrav`=0 and specify the CELL_PARAMETERS. It is important to notice that with `ibrav`=0, the lattice vectors must be given with a sufficiently large number of digits and with the correct symmetry to prevent problems related to symmetrization. When the CELL_PARAMETERS are set in bohr/angstrom, the lattice parameter is computed as alat$= \sqrt{v_1 \times v_1}$ where v_1 corresponds to the first cell vector. When these parameters are defined as "alat", it means that the lattice vectores are in units of the lattice parameters (either `celldm`(1) or Å). During this dissertation project the `ibrav`=0 and therefore CELL_PARAMETERS were defined.

3.2.2 Metal and Insulator Systems

The variable controlling how metallicity is treated is `occupations` in namelist &SYSTEM. When `occupations`='fixed', it means it will occupy the lowest (N electrons)/2 states and works only for insulators with a wide band gap width. In all other cases we use 'smearing',

except for the DOS calculations, where we should instead employ the tetrahedron method (`occupations`='tetrahedra'). This latter method divides the BZ into tetrahedra, calculating the eigenenergies at the corners of each tetrahedron, and then linearly interpolating the eigenenergies inside of each tetrahedron to perform the integration.

Smearing is a technique used for suppressing unstable electron densities in the calculation of metals. Such a problem occurs in metals (and semimetals) because the valence bands that cross the Fermi energy are partially occupied, so there is a discontinuity of the occupation number for the bands around that energy. Due to numerical accuracy, the electrons may occupy the unoccupied states during some iterations, yielding the algorithm unstable and slower to converge. In order to stabilize the algorithm without using excessive number of **k**-points, the smearing technique should be employed, is used, which replaces the occupation number (either 0 or 1) by a smoothly varying function of the energy. Such a smearing function could, for example be, a Fermi Dirac distribution, which instead of a step function (T = 0 K), we can use the finite temperature form. Adding electronic temperature (degauss) smooth out the abrupt change of the occupation number and as a result total energy converges with fewer number of **k**-points.

The smearing was fixed at 0.01 Ry for $C2/c$, $I\bar{4}2m$ and $I222$ with the Marzari-Vanderbilt smearing scheme [75]. This value is called `degauss` and correspond to the spreading (Ry) for BZ integration in metals. Since the initial magnetism of the system was not known, we chose the smearing technique, since for the input it would only be required the keyword `starting_magnetization`, which determines for each atom the initial spin moment at the start of the selfconsistent cycle.

The DOS calculations allowed us to determine the general distribution of states as a function of energy and can also determine the gap between energy bands in semiconductors [76]. A poorly represented DOS with smeared band edges, which gives rise to a nonzero DOS at the Fermi energy, can incorrectly describe an insulator or semiconductor to have a metal-like character. By observing Fig. (3.1), we can notice that the smearing methods influence the interpretation of the electronic states at the band edges. To calculate an accurate DOS, the linear tetrahedron method for BZ integration with Blöchl corrections [77] renders many salient features of the DOS with exceptional quality compared to the smearing methods. As we can see in Fig. (3.1), the expected $\sqrt{E}$ energy dependence and the sharp drop at the valence band edge is clear from the tetrahedra method, whereas the Gaussian smearing methods smoothens the valence band edge even for dense **k**-point

meshes. Using a coarse **k**-point mesh may show spurious DOS peaks that can be confused as Van Hove singularities (result from a vanishing slope in the E $vs.$ **k** dispersion relation).

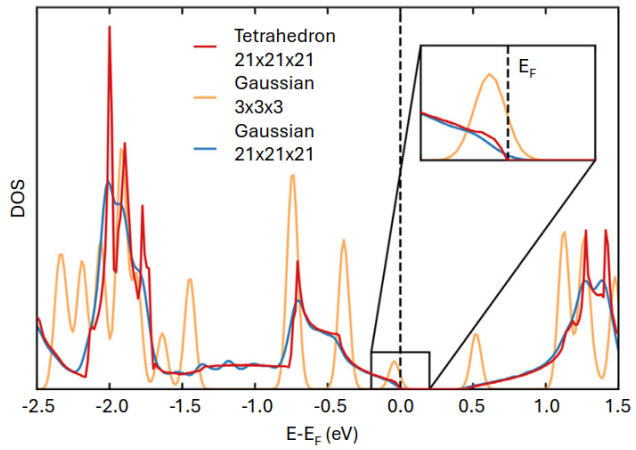

Figure 3.1: Comparison of the density of states of TiNiSn calculated via the tetrahedron method using a $21 \times 21 \times 21$ **k**-point mesh (red) and the Gaussian smearing method with $3 \times 3 \times 3$(orange) and $21 \times 21 \times 21$(blue) **k**-point meshes. The smearing width is set to 0.05 eV for calculations using Gaussian smearing methods. This figure has been adapted from Ref. [76]

3.2.3 Geometry and Structural Relaxation

To specify the geometry and space group of the crystal in the input file, several parameters have to be considered. The Bravais-lattice index (`ibrav`) defines the space group where at each number is associated to a space group. For each one of them, it should also be specified either `celldm(1)-celldm(6)` or `A, B, C cosAB, cosAC, cosBC`. The lattice parameter "alat" is set to alat = `celldm(1)` (in a.u.) or alat = A (in angstrom). For `ibrav=0` the CELL_PARAMETERS need to be specified. In the CELL_PARAMETERS card the lattice vectors can be defined, either in Bohr or angstrom (where the lattice parameters alat can be computed as $\sqrt{v_1 v_1}$ and can also be present in units of lattice parameters).

For the same symmetry group there are different possible positions of the atoms and the interatomic positions are defined when the forces between these are almost zero, and thus minimizing the total electronic energy of the crystal. QE has an automatic procedure to search efficiently for the minimum of this energy function.

There are two types of structural optimization calculations in Quantum espresso: (1) relax: where only the atomic positions are allowed to vary, and (2) vc-relax: which allows to vary both the atomic positions and lattice constants. Vc-relax is a function that minimizes the interatomic forces and stress in the system using a iteration of self-consistent calculations

while adapting the lattice parameters and ion positions, which correspond automatically to a minimal total energy.

To apply the vc-relax algorithm, we need to add the cards of $IONS and $CELL, to chose the minimization algorithm to consider the ionic and cell variation. The structural relaxations were carried out by considering the damped (quick-min Verlet [78]) dynamics, since it was the most appropriate algorithm to structurally minimize the studied systems.

3.2.4 Non-Self-Consistent Field Calculation

In the non-self-consistent field (NSCF) calculations, these are not preformed in a self consistent manner. The latter performs the solution with the objective of minimizing the density charge functional until a predetermined limit in the energy difference between two consecutive steps is achieved. Therefore the SCF calculation should be performed first to ensure the minimum KS energy state that should resemble the system's ground state.

The NSCF calculation will read in the converged charge density to construct the Hamiltonian without any update for the charge density. This should be performed after a SCF, sampling the system to a denser mesh in the reciprocal space, allowing for the aforementioned calculations, such as band structure, density of states and optical property calculations. Depending upon the system and for the DOS calculations, the **k**-point mesh should be considered with a denser **k**-point mesh, when compared to the SCF calculation.

It is also important to specify the number of electronic states (bands) to be calculated, `nbnd`. Note that in the spin-polarized calculations the number of **k**-point, not the number of bands per **k**-point, is doubled. By default, and accordingly to the employed `occupations` tag, for an insulator, `nbnd` is equal to number of valence bands, nbnd = (# of electrons /2) and for a metal is equal to 20% more (minimum 4 more). If we want to compute also the unoccupied states, and to better assess the conduction bands, we can specify a larger number for `nbnd`.

3.2.5 Hubbard parameters

As stated in section 2.2, the DFT semi-local functional (in our case PBE) predicts a metallic behavior and with the characteristics of our material we need to add a Hubbard term to obtain the correct description of our material. It is important to note that a reliable and consistent method to evaluate the Hubbard parameters is essential to achieve quantitative prediction. To compute the U parameter, the self-consistent approach is used

involving cyclic computations of the optimized structures and subsequent recalculation of the Hubbard parameters for each newly optimized crystal structure. This Hubbard correction was applied to the Pr $4f$-states by employing the simplified rotational-invariant formulation. By using DFPT for the calculation of the Hubbard parameters, we are able to calculate this parameter in a self-consistent manner, to make sure that the obtained Hubbard parameters are fully consistent with both the electronic structure of the system and with the crystal structure. The idea is to compute the effective U and V parameters from a DFT+U+V ground state until the values obtained from the DFPT calculation (U_{out} and V_{out}) coincide (within a fixed precision) with those used in determining the ground state that DFPT is based on (U_{in} and V_{in}).

$$|U_{\text{out}} - U_{\text{in}}| < 0.1 \quad |V_{\text{out}} - V_{\text{in}}| < 0.1 \tag{3.1}$$

The procedure to compute U_{scf} and V_{scf} is summarized in the flowchart of Fig. (3.2). Here we also describe the form we have used to treat the system as a magnetic insulator while computing the Hubbard parameters.

1. Set up the initial crystal structure for the system of interest and choose the initial values for U and V (the closest to zero).

2. Perform a SCF calculation by treating the system as a fake magnetic metal. Namely, specify `occupations`= 'smearing' and set up some very small broadening parameter, and set up `nspin`=2 and `starting_magnetization`. Moreover, use the convergence threshold `conv_thr` , which should not be too small, to avoid problems in the convergence of the next SCF cycle.

3. Perform a SCF calculation by treating the system as a magnetic insulator using the total magnetization obtained in the previous step. Extract from the previous calculation the total magnetization and the number of bands (KS states) and use them in this SCF calculation by using the keywords `tot_magnetization` and `nbnd`, respectively. Further details to be considered are:

   - Set up the `occupations` to be fixed;
   - Use `nspin`=2 and `tot_magnetization`, where the total magnetization must be extracted from the previous step. The setup of `tot_magnetization` is required, to allow the code to specify the spin up and down occupations correctly. If

`tot_magnetization` deviates slightly from an integer value then it is neccessary to round it to the integer value, because non-integer `tot_magnetization` cannot be used in the second SCF calculation (the deviation from the integer can be due to numerical noise);

- Set up the number of bands (nbnd) equal to the number of bands in the previous run [without specifying nbnd in this calculation, the code will set it to be equal to half the number of electrons, while in the previous (metallic) calculation the number of bands was determined as half of the number of electrons plus 20% - this mismatch would lead to numerical problems];
- In order to save CPU time in the current SCF calculation, it is recommended to start from the wavefunctions and the potential obtained in the previous step. To do so specify in the input `startingpot`='file' and `startingwfc`='file'. If you ignore this and try to start the SCF calculation from scratch, it may happen that the code will not converge at all (because it would be hard for it to find the ground state and the correct starting magnetization just from the condition of the constrained magnetization).

4. Perform the LR calculation of U using the HP code.
5. Perform a structural optimization using DFT+U+V with the current values of U and V (i.e., U_{out} and V_{out}).
6. Return to Step 2 with updated values of the Hubbard parameters (i.e., $U_{\text{in}} = U_{\text{out}}$ and $V_{\text{in}} = V_{\text{out}}$) and iterate the procedure until the point when the variations of the Hubbard parameters [see Eq. (3.1)] and of the crystal structure are both within fixed thresholds.

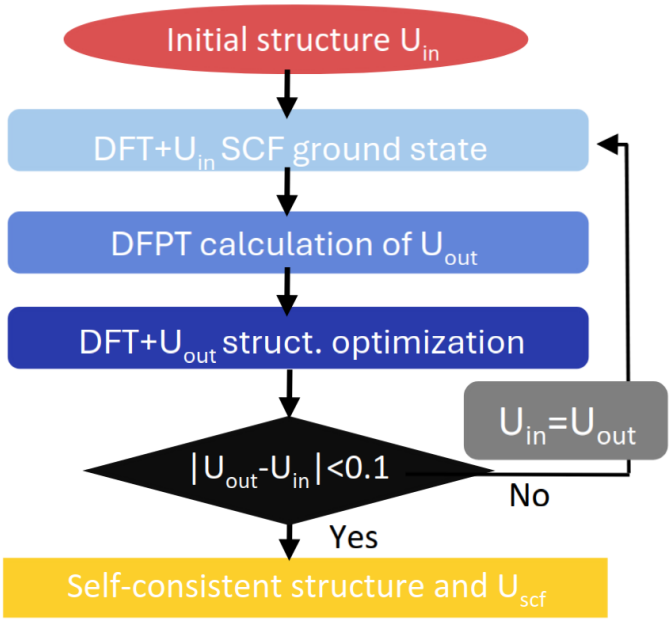

Figure 3.2: Flowchart of the process of computing the valued of the Hubbard parameter U adn V self-consistently.

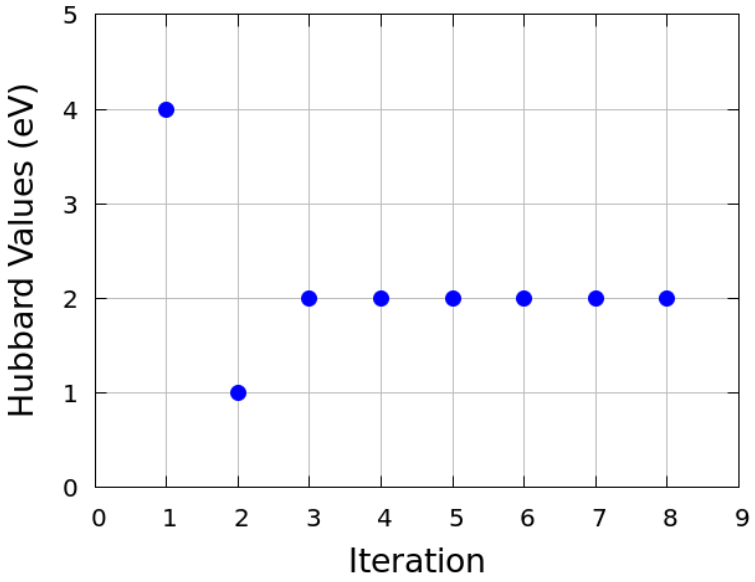

Figure 3.3: Convergence of the Hubbard parameter U during the self-consistent evaluation from DFPT calculations based on DFT+U. All calculations are based on a basis set of orthogonalized atomic orbitals for the Hubbard manifold.

4. Results

Results of the structural, electronic and magnetic properties, obtained from DFT and DFT+U calculations, will be discussed throughout this chapter. These results are compared across the different calculations schemes used, to assess the influence that these terms have in the structural and electronic properties of the crystal. We will also convey the results obtained for the Hubbard parameters and their significance, and finally the results regarding the magnetization of the crystal will be discussed.

4.1. Structural parameters and energetical stability

Our first goal was to assess which would be the most energetically stable structure. The first step was to perform a self-consistent field calculation (as explained in the Section 2.1.3) on the 3 structures we chose to focus on for this project. By resorting to the $\mathrm{pw.x}$) binary, which will compute the n$(\mathbf{r})$ and $\psi_{\mathbf{k},\nu}$, over the irreducible BZ in a way to access the converged values of the **k**-point sampling, energy cut-off for wavefunctions and charge density. Afterwards, a structure relaxation is necessary to obtain reliable equilibrium positions of the electrons and ions.

Comparing the three total electronic energies we have concluded that the most energetically stable structure for the crystal $Pr_2O_2SO_4$ is the monoclinic phase $C2/c$ (#15). The $I\overline{4}2m$ (#121) structural compound was also computed, yielding higher energy than the $C2/c$ (#15) system. As for the $I222$ system, within the timeframe of this dissertation, it was not possible to complete the structural and energetic minimization of respective system; however, it was possible to perform a few convergence cycles, and concluded that the electronic energy was much higher than for the other two studied polymorphs. Since, and being this system computationally more demanding in terms of convergence, we did not continue respective structural or electronic calculations.

After relaxing the atomic positions, we used the FINDSYM [79] on-line tool to obtain the symmetry operations of the underlying crystal lattice and atomic sites. One of the important quantities are the Wyckoff positions. To compute the Wyckoff positions one must test every symmetry operation of the crystal's point group and keep track of whether the specified point is invariant under that symmetry. The finite list of all symmetry operations which leave the given point invariant taken together make up another group, which is known as

the site symmetry group of that point. All the points with the same site symmetry group, or a conjugate site symmetry group, are assigned the same Wyckoff position.

The Wyckoff positions are designated by a letter, often preceded by the number of positions that are equivalent to a given position with that letter, in other words, the number of equivalent positions in the unit cell that a given starting position covers upon applying all the elements of the space group. The letters are assigned in alphabetical order with earlier letters indicating positions with fewer equivalent positions, or in other words with larger site symmetry groups.

For $Pr_2O_2SO_4$ with the space group $C2/c$ we have the following Wyckoff positions:

Wyckoff	Coordinates (x, y, z)		
f (Pr_1)	0.16937	0.50675	0.08447
	0.74619	0.50675	0.41553
	0.74619	0.49325	0.91554
	0.16937	0.49325	0.58447
e (S_1)	0.00000	0.94330	0.25000
	-0.00000	0.05673	0.75000
f (O_1)	0.25381	0.51526	0.37682
	0.74619	0.48474	0.62318
	0.74619	0.51526	0.12318
	0.25381	0.48474	0.87682
f (O_2)	0.99900	0.7358	0.10270
	0.00097	0.26420	0.89720
	0.00097	0.73580	0.39720
	0.99900	0.26420	0.60270
f (O_3)	0.09201	0.1395	0.29495
	0.90790	0.8605	0.70510
	0.90790	0.1395	0.20510
	0.09200	0.8605	0.79490

Table 4.1: Atomic positions grouped by Wyckoff positions of $Pr_2O_2SO_4$ with the monoclinic structure, $C2/c$ (#15). Coordinates are dimensionless, given in terms of the conventional unit cell defined in International Tables of Crystallography.

For the structure of Pr_2O_2S the obtained Wyckoff positions are:

Wyckoff	Coordinates (x, y, z)		
f (Pr_1)	0.33333	0.66667	0.28100
	0.66667	0.33333	0.71900
a (S_1)	0.00000	0.00000	0.00000
d (O_1)	0.33333	0.66667	0.62900
	0.66667	0.33333	0.37100

Table 4.2: Atomic positions grouped by Wyckoff position of Pr_2O_2S with the trigonal structure, $P\bar{3}m1$ (#164). Coordinates are dimensionless, given in terms of the conventional unit cell defined in International Tables of Crystallography.

$Pr_2O_2SO_4$	a (Å)	b (Å)	c (Å)	V(Å^3)
Experimental [12]	8.281(1)	4.244(1)	14.046(1)	–
DFT-PBE^M	7.352	7.352	8.310	474.83
DFT-PBE^T	4.152	4.152	14.649	126.26
DFT-PBE+U^M	4.265	7.375	8.304	238.68
DFT-PBE+U^T	4.168	4.168	7.930	127.88
Pr_2O_2S	a (Å)		c (Å)	V(Å^3)
Experimental [18]	3.980		6.830	95.710
DFT-PBE^P	3.930		6.752	90.316
DFT-PBE+U^P	3.917		6.767	89.899

Table 4.3: Lattice parameters (a, b, c) and volume (V), from the DFT-PBE and DFT-PBE+U calculations, both for the monoclinic (^{M}) and tetragonal(^{T}) structures of $Pr_2O_2SO_4$, and for the trigonal structure ^{P} of Pr_2O_2S. Comparison with experimental results are shown for the lattice parameters for the different systems.

We observe that the energy difference between the *C2/c* and the high-symmetry $I\bar{4}2m$ systems is solely of $\sim$ 37 meV, which results are both evidenced for the DFT and for the DFT+U results.

4.2. Band structure and Density of States of $Pr_2O_2SO_4$

The electronic PDOS and band structure were calculated, to better understand, not only the band gap energy of the materials, but also the composition of the valence and conduction band edges. These properties have been calculated for the $Pr_2O_2SO_4$ material with the monoclinic structure $C2/c$ (#15) and with the tetragonal structure $I\bar{4}2m$ (#121); and also for the trigonal phase ($P\bar{3}m1$) of Pr_2O_2S.

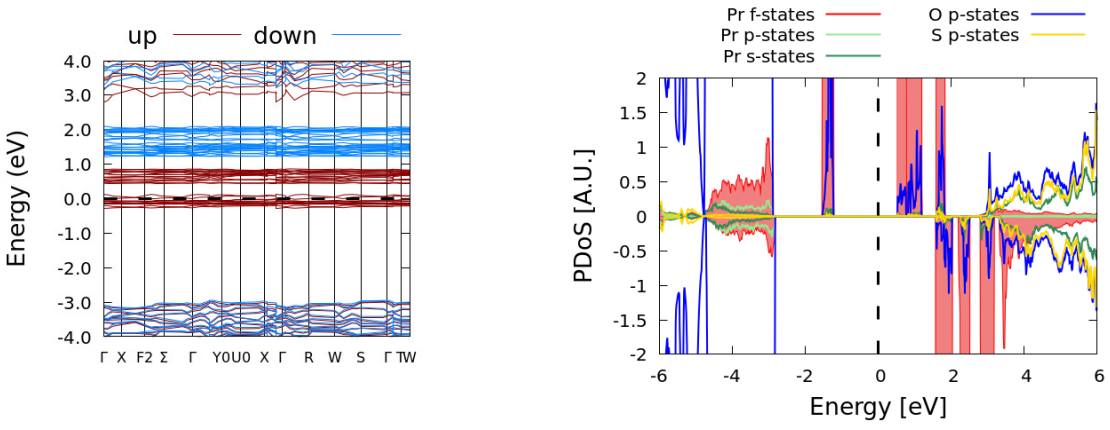

(a) (b)

Figure 4.1: DFT electronic band structure (top) and PDOS (bottom) (without including the Hubbard term) for the monoclinic structure $C2/c$ (#15) of $Pr_2O_2SO_4$ for the ferromagnetic order.

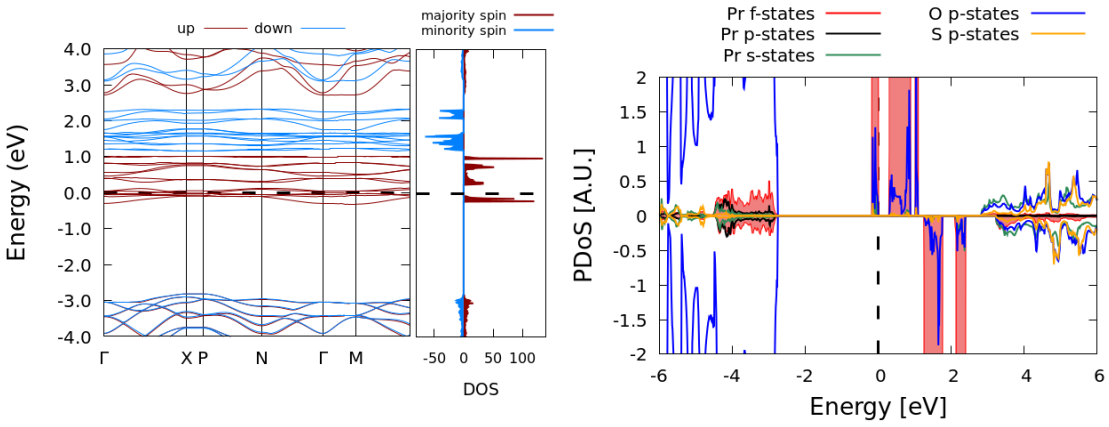

(a) (b)

Figure 4.2: DFT electronic band structure and total DOS (top) and PDOS (bottom) (without the Hubbard term) for the tetragonal structure $I\bar{4}2m$ (#121) of $Pr_2O_2SO_4$.

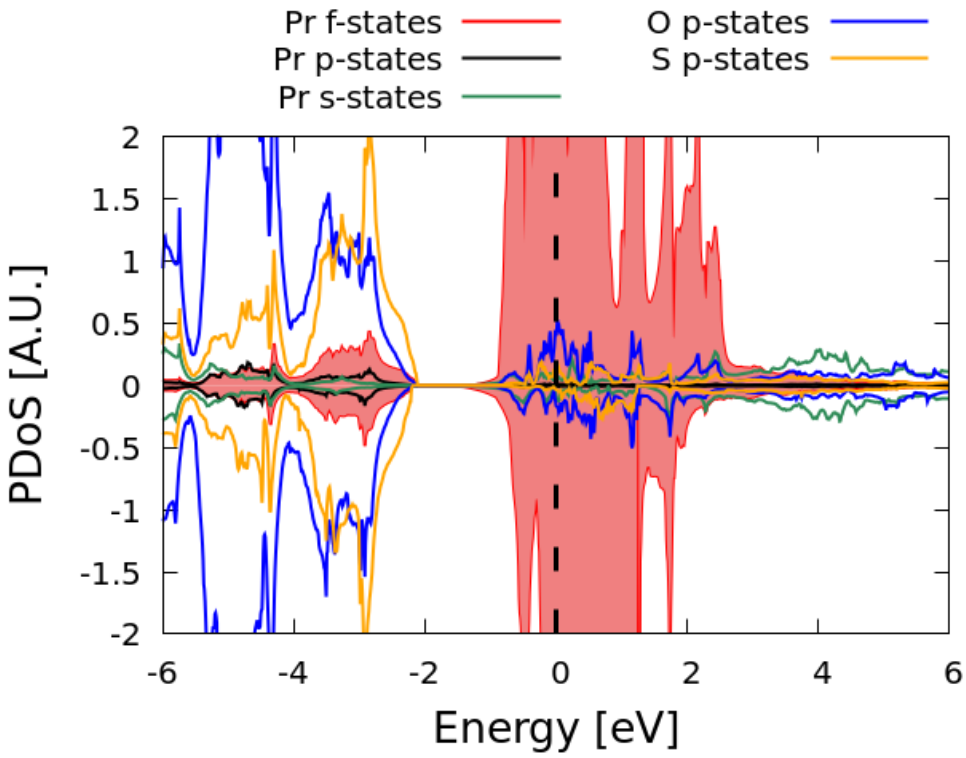

Figure 4.3: DFT electronic PDOS (bottom) (without considering the Hubbard term) for the trigonal structure $P\bar{3}m1$ (#164) of Pr_2O_2S.

The calculated spin polarized total and projected density of states of electrons are presented in Figs. (4.1), (4.2), (4.3), where the Fermi energy was aligned at 0 eV. Theoretically $\int_{E_0}^{E_1} DOS(E)dE$ is equal to the total number of states between a energy range, E_0 and E_1 (adimensional values and defined in the input for the calculation). This is what the $\mathrm{dos.x}$ executable included in QE computes. According to the above definition: DOS(E) $= \sum_n \int \frac{V}{4\pi^3}\delta(E - E_n(k_x, k_y, k_z))dk_x dk_y dk_z$.

It is important to note that the tetrahedron method improves drastically the quality of the DOS compared to the smearing method and that in these figure we can see the ferromagnetic spin alignment ordering imposed. The band gap value is equal to 1.27 eV for the tetragonal structure, $I\bar{4}2m$ (#121). Also, the O-p states are known to be the most energetic of the valence band, while the unoccupied Pr-f states should dominate at the minimum of the conduction band. Since we don't observe specifically this behavior in the PDOS of Figs. (4.1), (4.2), (4.3) we will have to resort to the Hubbard approach, to obtain a better description of the f-states of Pr. By employing the semi-local functional (PBE) we observe for Figs. (4.1), (4.2), (4.3) that the f-states are incorrectly being treated as delocalized states, thus characterizing our system as being a metal. This means that additional care must be taken to obtain the insulator properties that we are aware that this crystal evidences [80].

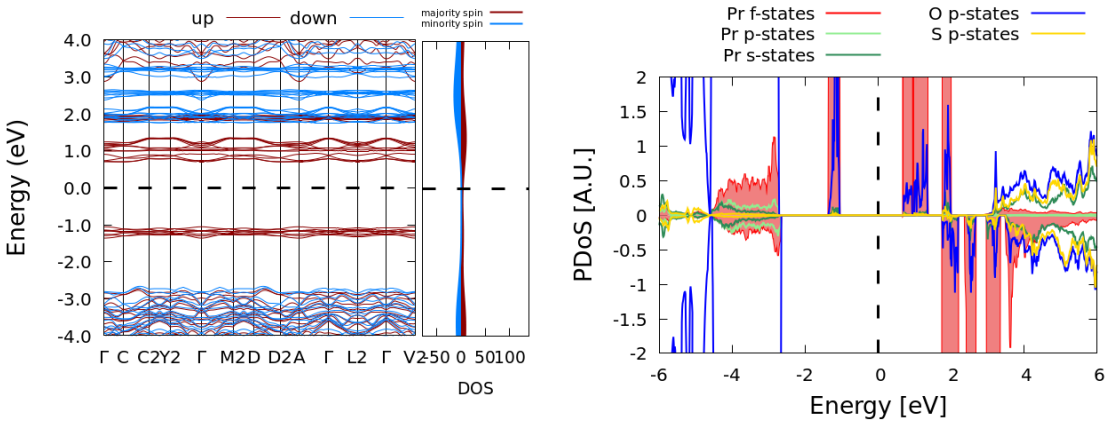

(a) (b)

Figure 4.4: DFT electronic and structure and DOS (top) and PDOS (bottom) with the Hubbard term equal to 2.1013 eV for the monoclinic structure $C2/c$ (#15) of $Pr_2O_2SO_4$.

Hubbard parameters By observing Figs. (4.4), (4.5), (4.6), that when imposing a Hubbard parameter (self-consistente value of U=2.1013 eV obtained for the tetragonal structure), DFT+U leads to a considerable increase in the band gap width. For example, for

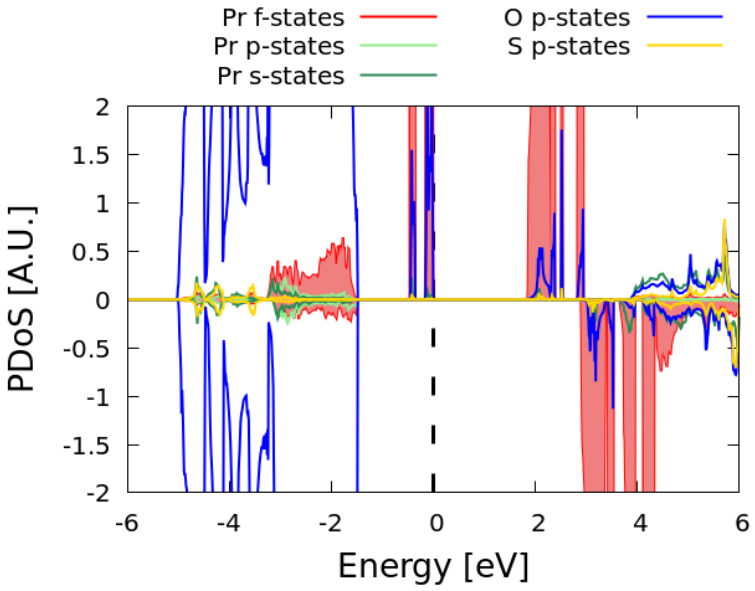

Figure 4.5: DFT electronic PDOS with the Hubbard term equal to 2.1013 eV for the tetragonal structure $I\overline{4}2m$ (#121) of $Pr_2O_2SO_4$.

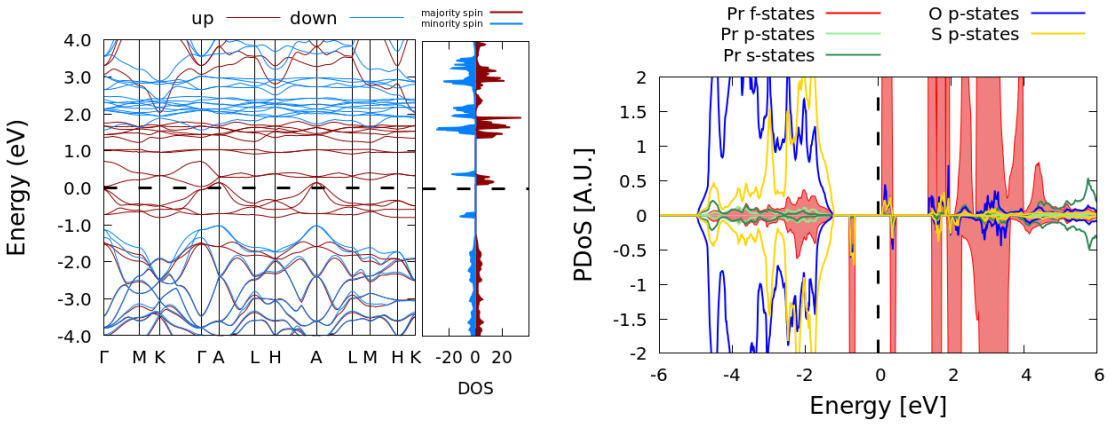

(a) (b)

Figure 4.6: DFT electronic band structure and DOS (top) and PDOS (bottom) with the Hubbard term equal to 2.1013 eV for the trigonal structure $P\overline{3}m1$ (#164) of Pr_2O_2S.

the Tetragonal structure we observe that the gap increase from 2.17 to 4.59 eV). As evident from the mentioned figures, while the DFT functional predicts a metallic behavior, DFT+U is effective in opening a band gap in the KS spectrum of the material resulting in a insulator behavior. This value of the Hubbard term was computed for the tetragonal structure, $I\overline{4}2m$, and we used the same value for the three studied structures and materials to better compare the energies and effect of Hubbard term on the structural, electronic and magnetic properties.

As for the trigonal structure $P\overline{3}m1$, and by comparing the experimental gap value of 2.86 eV, we obtain for the DFT+U a very close result with E_g=2.69 eV.

We would expect, that the valence band maximum should be mostly composed by O-p states. However, and by observing Fig. (4.5), we found that the ab-initio/computed U magnitude still yielded some hybridization of the f-localized states close to the Fermi energy. Therefore we have increased the magnitude of the Hubbard U parameter with the intention of 'pushing" the f-states to lower energies.

This quantity is generally determined semi-empirically (e.g., through fitting of the properties of a large variety of different systems) [81], or through a material-dependent optimization, (e.g. by an iterative procedures, as proposed in Ref [82]) so we can infer a value of U=4 eV.

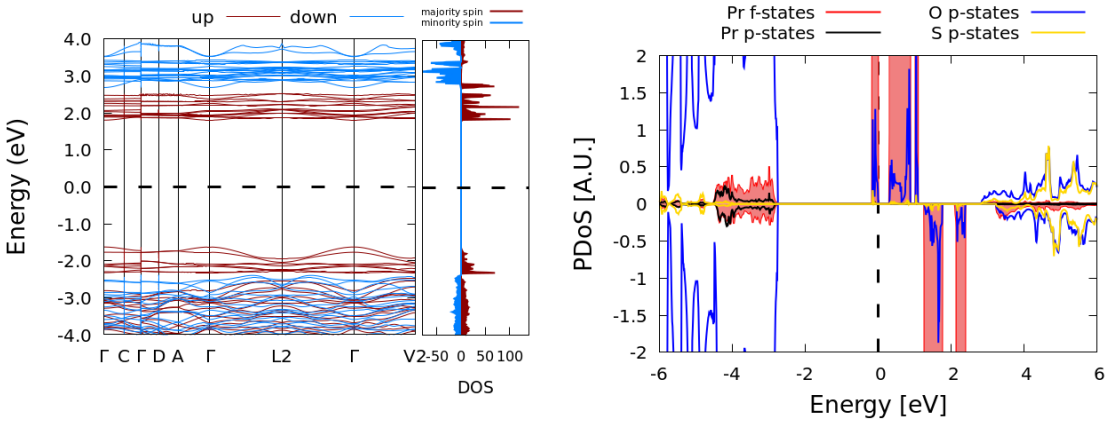

(a) (b)

Figure 4.7: DFT electronic band structure and DOS (top) and PDOS (bottom) with the Hubbard term equal to 4.0 eV for the monoclinic structure $C2/c$ (#15) of Pr_2O_2S.

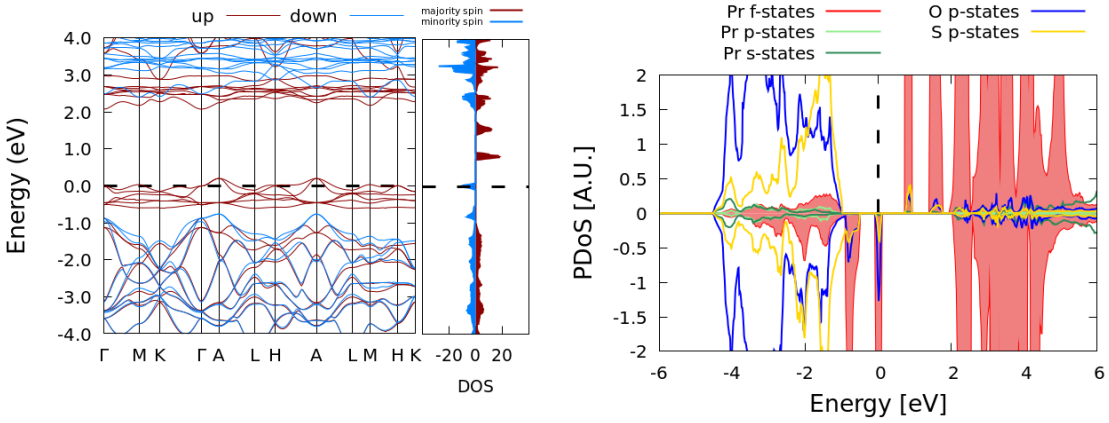

(a) (b)

Figure 4.8: DFT electronic band structure and DOS (top) and PDOS (bottom) with the Hubbard term equal to 4.0 eV for the trigonal structure $P\bar{3}m1$ (#164) of Pr_2O_2S.

Magnetization Each atomic contribution of the magnetic moment is presented in Table 4.4. The calculated net magnetic moment resulted in 4 Bohr mag/cell.

Atom	R	charge	MM
Pr	0.123	18.4252	1.8979
O1	0.078	4.1108	-0.0025
O2	0.078	4.0142	-0.0407
S	0.078	1.3042	0.0008

Table 4.4: Magnetic Moment (MM) per site (integrated at the atomic sphere of radius, R, computed using DFT) for the ferromagnetic ordering of the monoclinic structure $C2/c$ (#15).

The lowest value of magnetic moment of Pr owes to the fact that we did not apply SOC in our calculations. The partially filled Pr atoms have large orbital angular momentum, and hence total angular momentum, so owing to large orbital magnetic moment Pr couples strongly with the lattice via SOC coupling. This in turn may lead to large magnetic moment of Pr and hence of the substituted compounds in supercell as compared to that for free Pr(+3) ion. Besides, the difference may also originate from the DFT methods employed and the fact that calculations were done at 0 K.

We now present the electronic (P)DOS and band structure (Fig. 4.9) for the antiferromagnetic ordering of the A-type (see Fig. 2.2) that evidences to be energetically more stable when compared to other antiferromagnetic ordering states and the ferromagnetic system. We may observe that the C-AF ordering is energetically very close to the A-AF system.

composition	A-AF	C-AF	G-AF
$Pr_2O_2SO_4$	0.80	0.00	2.27

Table 4.5: Relative energy, in units of eV, between the different antiferromagnetic ordering of $Pr_2O_2SO_4$ for the $C2/c$ structural compound, when employinh DFT+U=2.1013 eV.

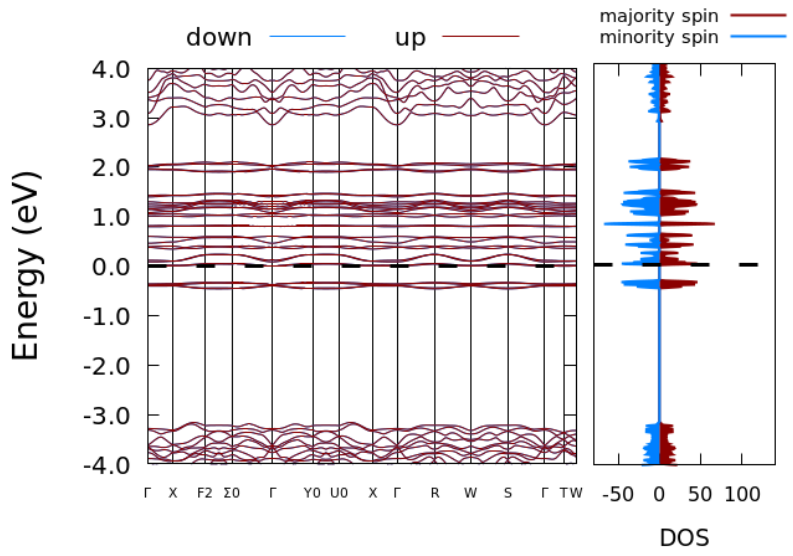

(a)

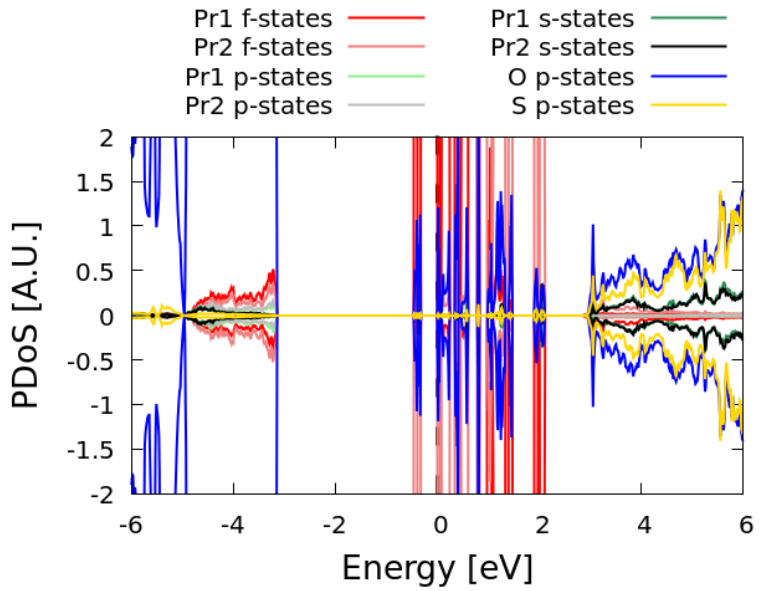

(b)

Figure 4.9: DFT+U electronic band structure and DOS (top) and PDOS (bottom) of the monoclinic structure $C2/c$ (#15) of $Pr_2O_2SO_4$, by considering the antiferromagnetic ordering of A-type.

4.3. Bader Charge Analysis

After performing a Bader Charge Analysis for the crystal $Pr_2O_2SO_4$, we concluded that the total of 87.9974 of defined valency of the unit-cell, 20.91 are assigned to Pr, 7.34 to O and 2.26 to S. To convert this to ionic charge, we will also require the number of electrons that are defined as being core-electrons. From the PAW pseudopotential, we confirm that the electrons with orbitals $5s$, $6s$, $5p$, $4d$ e $4f$ are not fixed to the core and corresponds to twenty three electrons. The O pseudopotential indicates that two $1s$ are core electrons,

while two $2s$ and four $2p$ are valence electrons. The pseudopotential shows that two electrons of the orbital $3s$ and four of the orbital $3p$ are not considered in the core. From this, we can subtract the charge obtained from the Bader analysis from the total value of the valence electrons presented in the employed pseudopotential, arriving at the Bader charge-based states of $Pr^{2.88+}$, $O^{1.34-}$ and $S^{3.74+}$. These values are slightly smaller than the valencies of +4, -2, +6, defined for each element, respectively, indicating that there might be some degree of covalent character.

By comparing to the Löwdin charges, computed directly with QE, we may infer slight differences with the Bader charges.

In terms of Pr_2O_2S, from the 63.9998 valence electrons, 21.08 are assigned to Pr, 7.29 to O and 7.25 to S. By using the same approach as before, we obtain for the Bader charge-based states of $Pr^{1.92+}$, $O^{1.25-}$ and $S^{1.29-}$. Again, these are slightly lower values than the valencies of respective ionic elements, indicating some covalency character as well, or even charge transfer between the ions.

4.4. Reaction between oxysulfate/oxysulfide

To compute the formation energy [83], we used the expression, that is based on the reaction presented in Eq. (1.3):

$$E(Pr_2O_2SO_4) - E(O_2) - E(Pr_2O_2S) \tag{4.1}$$

where $E(Pr_2O_2SO_4)$ and $E(Pr_2O_2S)$ are the total energy of the $Pr_2O_2SO_4$ and Pr_2O_2S, systems respectively; and $E(O_2)$ is the reference energy for oxygen that is given by a O_2 molecule at T = 0.

The energy of the $Pr_2O_2SO_4$ compound was considered in the ground-state form, $C2/c$, and by including U=2.1013 eV. For Pr_2O_2S, we have also considered the energy when applying Hubbard U=2013 eV, and both systems in their ferromagnetic states. We obtained that value of E_F=83.388 eV, meaning that the reaction is endoenergetic, therefore promoting the production of $Pr_2O_2SO_4$.

4.5. Discussion of some results

By characterizing several structural symmetries of $Pr_2O_2SO_4$ it was possible to obtain different properties for the studied systems. The tetragonal structure $I\bar{4}2m$ (#121) was more stable with the ferromagnetic magnetic order, whereas the monoclinic structure

$C2/c$ (#15) is energetically more stable when the antiferromagentic order is taken into account. Not only does this material evidences diferent polymorphs, meaning that there are possible metastable polymorphs, where the possibility of inducing strutural transitions can be possible when applying external perturbation (i.e. temperature, pressure), but also magnetic transitions can also occur. Slight morphology differences can change the energetical stanility of the systems quite drastically.

It is important to note that the states that are treated as being valence electrons in the pseudopotential, correspond to the states of the valence band and below the Fermi energy (in which electrons are normally present at absolute zero temperature); whereas the empty states/orbitals are the conduction band states. As we can see in the PDOS presented in the results, the conduction orbitals correspond to the s- and f-orbitals of praseodymium, p-orbitals of oxygen and p-orbitals of sulphur. This conclusion can be compared to the values of the Bader charge presented in 4.3. We can also see that the d-orbitals of Pr are not present. Because these are completly filled states, respective states would be localized at a very low energy window, well below the range we present in this work, and therefore does not merit further discussion. By using a Hubbard parameter of 4eV, the PDOS obtained was characteristic of an insulator like with the Hubbard parameter obtained self-consistently and the band gap obtained was of the same order. In terms of the f orbitals of the Pr element, we obtained similar characteristics around the Fermi energy, corresponding to the same oxidation states.

5. Conclusion

The motivation for this work was to better understand the crystal structure of $Pr_2O_2SO_4$ and the different polymorphs it may undergoe, together with the different stable magnetic orderings. Our study also considered the Pr_2O_2S crystal, since it is a product of $Pr_2O_2SO_4$, which under ideal conditions can promote oxygen mobilities, enabling this to be a good candidate for SOFC and oxygen storage . Our study will enable direct and important atomistic information to aid works carried out by the experimental group of TEMA.

In terms of the ground state we concluded that the monoclinic structure, $C2/c$ (#15), is the most stable and especially in the A-type antiferromagnetic ordering. The atomistic calculations were computationally very demanding, mainly for the monoclinic space group. In order to obtain accuracies regarding the ground-state system, we had to perform full volume relaxations, and several self-consistent calculations for each structure, and by assessing the different magnetic orderings.

In terms of the Hubbard U parameter, we can say that the influence was the expected in this system with strong correlated atoms and that the result using DFPT in relation to the semi-empirically option gives different characteristic to the crystal. By adding the Hubbard term the crystal turns out to be a insulator as it was expected. The Hubbard value that we computed self-consistently was equal to 2.1013 and, despite the fact of a charactsteristic insulator-like PDOS, when increasing the magnitude of U to 4 eV, we obtained a similar behavior of the different atomic states around the Fermi energy. It would be interesting to also employ other Hubbard projectors to see the influence that it could have on the value of this parameter and on the effect in the band structure and PDOS. By looking at the PDOS of the crystal it was possible to see which orbitals were in the valence band and in the conduction band to better understand the oxidation states of this material and the oxidation easiness between both $Pr_2O_2SO_4$/Pr_2O_2S. It is also important to use the Hubbard term in this systems and to comprove that it is actually a good theory for materials with d- or f- unfilled orbitals.

By computing the Bader charge-based states we could observe how the crystal characteristics influence the charges because it shows a small covalent-like character. It was also interesting to compare the values of the Bader analysis and the PDOS. As it was presented in Section 1.3, the material $Pr_2O_2SO_4$ can have several oxidation states. This

feature would be interesting to pursue further, and observe “numerically” what effect could enable different results for the Bader charges, by analysing the same crystal (for example, with the effect of pressure).

By computing the formation energy, it was possible to conclude that the reactions between $Pr_2O_2SO_4$ and Pr_2O_2S is endoenergetic, meaning that for Pr_2O_2S to be formed, it is necessary to provide energy so that the reaction can occur.

This synergy between experimental and theoretical work was essential to accelerate the understanding of this material and the physics underlying its functionality.

5.1. Future work

Pr couples strongly with the lattice via SOC interactions so it would be beneficial for this project to introduce this term in the calculation and observe if such effect can have a significant influence to the results obtained without including SOC.

We can also agree that the theoretical values related to the structural parameters that we obtain are in good agreement with the values we found in literature. This is good to confirm the quality of our results and our conclusions.

It is important to have a good convergence threshold for selfconsistency. This is applied in a way that the `estimated energy error` < `conv_thr`. Having smaller convergence thresholds is better to have more accurate results but it increases the required computational time. In our case it is possible to decrease this threshold ant it would be interesting to see if it made some influence in the results.

In terms of the results that we obtained with respect to the magnetic characteristics of the material, it is possible to propose new exhange-correlation functionals (i.e. hybrid functionals) and compare results.

In terms of the reaction between oxysulfate/oxysulfite it is interesting to also analise the intermediate steps between the initial state and the final state of the crystals to understand structurally what happens. This can be achieved by considering transition pathways of the reaction, by employing, for example, the Nudge Elastic Band calculation.

References

[1] M. Machida, K. Kawamura, K. Ito, and K. Ikeue, “Large-capacity oxygen storage by lanthanide oxysulfate/oxysulfide systems,” *Chemistry of materials*, vol. 17, no. 6, pp. 1487–1492, 2005. [Cited on pages 3 and 8.]

[2] A. Lashtabeg and S. J. Skinner, “Solid oxide fuel cells—a challenge for materials chemists?” *Journal of Materials Chemistry*, vol. 16, no. 31, pp. 3161–3170, 2006. [Cited on pages 3 and 4.]

[3] W. F. Smith, “The role of fuel cells in energy storage,” *Journal of Power Sources*, vol. 86, no. 1-2, pp. 74–83, 2000. [Cited on page 3.]

[4] F. J. A. Loureiro, T. Yang, D. G. Stroppa, and D. P. Fagg, “Pr2o2so4–la0.6sr0.4co0.2fe0.8o3−δ: a new category of composite cathode for intermediate temperature-solid oxide fuel cells,” *J. Mater. Chem. A*, vol. 3, pp. 12 636–12 641, 2015. [Online]. Available: http://dx.doi.org/10.1039/C4TA06640E [Cited on pages viii, 4, 6, and 7.]

[5] C. Xia and M. Liu, “Novel cathodes for low-temperature solid oxide fuel cells,” *Advanced Materials*, vol. 14, no. 7, pp. 521–523, 2002. [Cited on page 4.]

[6] J. H. Kim and H. Kim, “Ce0. 9gd0. 1o1. 95 supported la0. 6sr0. 4co0. 2fe0. 8o3-δ cathodes for solid oxide fuel cells,” *Ceramics International*, vol. 38, no. 6, pp. 4669–4675, 2012. [Cited on page 4.]

[7] C. Sun, R. Hui, and J. Roller, “Cathode materials for solid oxide fuel cells: a review,” *Journal of Solid State Electrochemistry*, vol. 14, pp. 1125–1144, 2010. [Cited on page 4.]

[8] C. E. Hori, H. Permana, K. S. Ng, A. Brenner, K. More, K. M. Rahmoeller, and D. Belton, “Thermal stability of oxygen storage properties in a mixed ceo2-zro2 system,” *Applied Catalysis B: Environmental*, vol. 16, no. 2, pp. 105–117, 1998. [Cited on page 4.]

[9] K. Ikeue, M. Eto, D.-J. Zhang, T. Kawano, and M. Machida, “Large-capacity oxygen storage of Pd-loaded $pr_2o_2so_4$ applied to anaerobic catalytic CO oxidation,” *Journal of Catalysis*, vol. 248, no. 1, pp. 46–52, 2007. [Cited on page 5.]

[10] M. Machida, K. Kawamura, and K. Ito, “Novel oxygen storage mechanism based on redox of sulfur in lanthanum oxysulfate/oxysulfide,” *Chemical Communications*, no. 6, pp. 662–663, 2004. [Cited on page 5.]

[11] W. W. Crook, “Texasite, a new mineral; the first example of a differentiated rare-earth species,” *American Mineralogist*, vol. 62, no. 9-10, pp. 1006–1008, 1977. [Cited on pages 5 and 6.]

[12] M. Machida, T. Kawano, M. Eto, D. Zhang, and K. Ikeue, “Ln dependence of the large-capacity oxygen storage/release property of ln oxysulfate/oxysulfide systems,” *Chemistry of materials*, vol. 19, no. 4, pp. 954–960, 2007. [Cited on pages 6, 7, and 49.]

[13] A. K. Singh, L. Zhou, A. Shinde, S. K. Suram, J. H. Montoya, D. Winston, J. M. Gregoire, and K. A. Persson, “Electrochemical stability of metastable materials,” *Chemistry of Materials*, vol. 29, no. 23, pp. 10 159–10 167, 2017. [Online]. Available: https://doi.org/10.1021/acs.chemmater.7b03980 [Cited on pages 6 and 8.]

[14] M. Machida, K. Kawamura, T. Kawano, D. Zhang, and K. Ikeue, “Layered Pr-dodecyl sulfate mesophases as precursors of $Pr_2O_2SO_4$ having a large oxygen-storage capacity,” *Journal of Materials Chemistry*, vol. 16, no. 30, pp. 3084–3090, 2006. [Cited on page 6.]

[15] C.-K. Loong, P. Thiyagarajan, J. Richardson Jr, M. Ozawa, and S. Suzuki, “Microstructural evolution of zirconia nanoparticles caused by rare-earth modification and heat treatment,” *Journal of Catalysis*, vol. 171, no. 2, pp. 498–505, 1997. [Cited on page 6.]

[16] F. Zamar, A. Trovarelli, C. de Leitenburg, and G. Dolcetti, “Ceo 2-based solid solutions with the fluorite structure as novel and effective catalysts for methane combustion,” *Journal of the Chemical Society, Chemical Communications*, no. 9, pp. 965–966, 1995.

[17] L. Kundakovic and M. Flytzani-Stephanopoulos, “Cu-and ag-modified cerium oxide catalysts for methane oxidation,” *Journal of Catalysis*, vol. 179, no. 1, pp. 203–221, 1998. [Cited on page 6.]

[18] M. Mikami and S. Nakamura, “Electronic structure of rare-earth sesquioxides and oxysulfides,” *Journal of Alloys and Compounds*, vol. 408, pp. 687–692, 2006. [Cited on pages 8, 49, and 76.]

[19] P. Andreev, E. Sal'nikova, and A. Kislitsyn, "Kinetics of the transformation of ln 2 o 2 so 4 into ln 2 o 2 s (ln= la, pr, nd, and sm) in a hydrogen flow," *Russian Journal of Physical Chemistry A*, vol. 87, pp. 1482–1487, 2013. [Cited on page 8.]

[20] K. Momma and F. Izumi, "Vesta 3 for three-dimensional visualization of crystal, volumetric and morphology data," *Journal of Applied Crystallography*, vol. 44, pp. 1272–1276, 2011. [Online]. Available: https://api.semanticscholar.org/CorpusID:96089398 [Cited on pages viii and 8.]

[21] R. M. Martin, *Electronic structure: basic theory and practical methods*. Cambridge University Press, 2020. [Cited on pages 9, 13, 14, 15, and 16.]

[22] G. Giuliani and G. Vignale, *Quantum Theory of the Electron Liquid*. Cambridge University Press, 2005, ch. 7. [Cited on pages 9, 12, 13, 14, 15, 16, and 69.]

[23] D. R. Hartree, "The wave mechanics of an atom with a non-coulomb central field. part ii. some results and discussion," in *Mathematical Proceedings of the Cambridge Philosophical Society*, vol. 24, no. 1. Cambridge University Press, 1928, pp. 111–132. [Cited on page 10.]

[24] P. Lykos and G. W. Pratt, "Discussion on the hartree-fock approximation," *Rev. Mod. Phys.*, vol. 35, pp. 496–501, Jul 1963. [Online]. Available: https://link.aps.org/doi/10.1103/RevModPhys.35.496 [Cited on page 11.]

[25] P. Hohenberg and W. Kohn, "Inhomogeneous electron gas," *Physical review*, vol. 136, no. 3B, p. B864, 1964. [Cited on page 12.]

[26] W. Kohn and L. J. Sham, "Self-consistent equations including exchange and correlation effects," *Physical review*, vol. 140, no. 4A, p. A1133, 1965. [Cited on page 12.]

[27] R. Parr and Y. Weitao, *Density-Functional Theory of Atoms and Molecules*, ser. International Series of Monographs on Chemistry. Oxford University Press, 1994. [Online]. Available: https://books.google.pt/books?id=mGOpScSIwU4C [Cited on page 16.]

[28] T. Kotani and M. Van Schilfgaarde, "Fusion of the lapw and lmto methods: The augmented plane wave plus muffin-tin orbital method," *Physical Review B—Condensed Matter and Materials Physics*, vol. 81, no. 12, p. 125117, 2010. [Cited on page 16.]

[29] D. M. Ceperley and B. J. Alder, "Ground state of the electron gas by a stochastic method," *Physical review letters*, vol. 45, no. 7, p. 566, 1980. [Cited on page 16.]

[30] J. P. Perdew and A. Zunger, “Self-interaction correction to density-functional approximations for many-electron systems,” *Physical review B*, vol. 23, no. 10, p. 5048, 1981. [Cited on page 16.]

[31] A. D. Becke, “Density-functional exchange-energy approximation with correct asymptotic behavior,” *Physical review A*, vol. 38, no. 6, p. 3098, 1988. [Cited on page 17.]

[32] J. P. Perdew and Y. Wang, “Accurate and simple analytic representation of the electron-gas correlation energy,” *Physical review B*, vol. 45, no. 23, p. 13244, 1992. [Cited on page 17.]

[33] J. P. Perdew, K. Burke, and M. Ernzerhof, “Generalized gradient approximation made simple,” *Physical review letters*, vol. 77, no. 18, p. 3865, 1996. [Cited on pages 17 and 39.]

[34] T. M. Project, “Materials data on Pr_2SO_2 by materials project,” July 2020. [Cited on page 17.]

[35] K.-S. A. M. M. B. Saal, J. E. and C. Wolverton, “Materials design and discovery with high-throughput density functional theory: The open quantum materials database (OQMD),” *JOM*, vol. 65, pp. 1501–1509, 2013. [Cited on page 17.]

[36] K. Terakura, T. Oguchi, A. Williams, and J. Kübler, “Band theory of insulating transition-metal monoxides: Band-structure calculations,” *Physical Review B*, vol. 30, no. 8, p. 4734, 1984. [Cited on page 18.]

[37] M. Cococcioni and S. De Gironcoli, “Linear response approach to the calculation of the effective interaction parameters in the lda+ u method,” *Physical Review B*, vol. 71, no. 3, p. 035105, 2005. [Cited on pages viii, 18, 19, 21, 25, and 27.]

[38] S. A. Tolba, K. M. Gameel, B. A. Ali, H. A. Almossalami, and N. K. Allam, “The dft+ u: Approaches, accuracy, and applications,” *Density Functional Calculations-Recent Progresses of Theory and Application*, vol. 1, p. 5772, 2018. [Cited on page 18.]

[39] S. L. Dudarev, G. A. Botton, S. Y. Savrasov, C. Humphreys, and A. P. Sutton, “Electron-energy-loss spectra and the structural stability of nickel oxide: An lsda+ u study,” *Physical Review B*, vol. 57, no. 3, p. 1505, 1998. [Cited on page 18.]

[40] V. L. Campo and M. Cococcioni, “Extended dft+ u+ v method with on-site and inter-site electronic interactions,” *Journal of Physics: Condensed Matter*, vol. 22, no. 5, p. 055602, 2010. [Cited on page 20.]

[41] A. Belozerov, M. Korotin, V. Anisimov, and A. Poteryaev, “Monoclinic m 1 phase of vo 2: Mott-hubbard versus band insulator,” *Physical Review B—Condensed Matter and Materials Physics*, vol. 85, no. 4, p. 045109, 2012. [Cited on page 21.]

[42] L. Haas, P. Mlkvik, N. A. Spaldin, and C. Ederer, “Incorporating static intersite correlation effects in vanadium dioxide through dft $+v$,” *arXiv preprint arXiv:2406.08947*, 2024. [Cited on page 21.]

[43] A. Liechtenstein, V. I. Anisimov, and J. Zaanen, “Density-functional theory and strong interactions: Orbital ordering in mott-hubbard insulators,” *Physical Review B*, vol. 52, no. 8, p. R5467, 1995. [Cited on page 21.]

[44] I. Timrov, N. Marzari, and M. Cococcioni, “Hp–a code for the calculation of hubbard parameters using density-functional perturbation theory,” *Computer Physics Communications*, vol. 279, p. 108455, 2022. [Cited on pages 22, 25, 27, and 31.]

[45] ——, “Self-consistent hubbard parameters from density-functional perturbation theory in the ultrasoft and projector-augmented wave formulations,” *Physical Review B*, vol. 103, no. 4, p. 045141, 2021. [Cited on pages 24, 28, and 32.]

[46] P.-O. Löwdin, “On the non-orthogonality problem connected with the use of atomic wave functions in the theory of molecules and crystals,” *The Journal of Chemical Physics*, vol. 18, no. 3, pp. 365–375, 1950. [Cited on page 25.]

[47] I. Timrov, F. Aquilante, L. Binci, M. Cococcioni, and N. Marzari, “Pulay forces in density-functional theory with extended hubbard functionals: From nonorthogonalized to orthogonalized manifolds,” *Physical Review B*, vol. 102, no. 23, p. 235159, 2020. [Cited on page 25.]

[48] M. Levy, “Electron densities in search of hamiltonians,” *Physical Review A*, vol. 26, no. 3, p. 1200, 1982. [Cited on page 26.]

[49] J. P. Perdew and M. Levy, “Physical content of the exact kohn-sham orbital energies: band gaps and derivative discontinuities,” *Physical Review Letters*, vol. 51, no. 20, p. 1884, 1983. [Cited on page 26.]

[50] B. Himmetoglu, A. Floris, S. De Gironcoli, and M. Cococcioni, “Hubbard-corrected dft energy functionals: The lda+ u description of correlated systems,” *International Journal of Quantum Chemistry*, vol. 114, no. 1, pp. 14–49, 2014. [Cited on page 26.]

[51] P. Giannozzi, O. Andreussi, T. Brumme, O. Bunau, M. B. Nardelli, M. Calandra, R. Car, C. Cavazzoni, D. Ceresoli, M. Cococcioni, N. Colonna, I. Carnimeo, A. D. Corso, S. de Gironcoli, P. Delugas, R. A. DiStasio, A. Ferretti, A. Floris, G. Fratesi, G. Fugallo, R. Gebauer, U. Gerstmann, F. Giustino, T. Gorni, J. Jia, M. Kawamura, H.-Y. Ko, A. Kokalj, E. Küçükbenli, M. Lazzeri, M. Marsili, N. Marzari, F. Mauri, N. L. Nguyen, H.-V. Nguyen, A. O. de-la Roza, L. Paulatto, S. Poncé, D. Rocca, R. Sabatini, B. Santra, M. Schlipf, A. P. Seitsonen, A. Smogunov, I. Timrov, T. Thonhauser, P. Umari, N. Vast, X. Wu, and S. Baroni, “Advanced capabilities for materials modelling with quantum espresso,” *Journal of Physics: Condensed Matter*, vol. 29, no. 46, p. 465901, oct 2017. [Online]. Available: https://dx.doi.org/10.1088/1361-648X/aa8f79 [Cited on page 31.]

[52] I. Timrov, N. Marzari, and M. Cococcioni, “Hubbard parameters from density-functional perturbation theory,” *Phys. Rev. B*, vol. 98, p. 085127, Aug 2018. [Online]. Available: https://link.aps.org/doi/10.1103/PhysRevB.98.085127 [Cited on page 32.]

[53] J. Paier, M. Marsman, and G. Kresse, “Why does the b3lyp hybrid functional fail for metals?” *The Journal of chemical physics*, vol. 127, no. 2, 2007. [Cited on page 33.]

[54] M. D. Krcha and M. J. Janik, “Examination of oxygen vacancy formation in mn-doped ceo2 (111) using dft+ u and the hybrid functional hse06,” *Langmuir*, vol. 29, no. 32, pp. 10 120–10 131, 2013. [Cited on page 33.]

[55] I. Timrov, F. Aquilante, M. Cococcioni, and N. Marzari, “Accurate electronic properties and intercalation voltages of olivine-type li-ion cathode materials from extended hubbard functionals,” *PRX Energy*, vol. 1, no. 3, p. 033003, 2022. [Cited on page 33.]

[56] J. Sun, R. C. Remsing, Y. Zhang, Z. Sun, A. Ruzsinszky, H. Peng, Z. Yang, A. Paul, U. Waghmare, X. Wu *et al.*, “Scan: An efficient density functional yielding accurate structures and energies of diversely-bonded materials,” *arXiv preprint arXiv:1511.01089*, 2015. [Cited on page 33.]

[57] M. Siddique, A. Ur-Rehman, M. Khan, A. Bashir, Z. M. Elqahtani, N. Alwadai, and S. Azam, “A first-principles theoretical study of structural, electronic, and magnetic

properties of lead-doped alloys of praseodymium bismuth compounds prpb x bi 1-x." *Digest Journal of Nanomaterials & Biostructures (DJNB)*, vol. 19, no. 2, 2024. [Cited on page 34.]

[58] R. Mahajan, I. Timrov, N. Marzari, and A. Kashyap, "Importance of intersite hubbard interactions in $\beta-\mathrm{mno}_2$: A first-principles $\mathrm{DFT}+u+v$ study," *Phys. Rev. Mater.*, vol. 5, p. 104402, Oct 2021. [Online]. Available: https://link.aps.org/doi/10.1103/PhysRevMaterials.5.104402 [Cited on page 35.]

[59] C. Ricca, I. Timrov, M. Cococcioni, N. Marzari, and U. Aschauer, "Self-consistent site-dependent dft+u study of stoichiometric and defective srmno_3," *Phys. Rev. B*, vol. 99, p. 094102, Mar 2019. [Online]. Available: https://link.aps.org/doi/10.1103/PhysRevB.99.094102 [Cited on page 35.]

[60] A. O. de-la Roza, M. Blanco, A. M. Pendás, and V. Luaña, "Critic: a new program for the topological analysis of solid-state electron densities," *Computer Physics Communications*, vol. 180, no. 1, pp. 157–166, 2009. [Online]. Available: https://www.sciencedirect.com/science/article/pii/S0010465508002865 [Cited on page 36.]

[61] A. O. de-la Roza, E. R. Johnson, and V. Luaña, "Critic2: A program for real-space analysis of quantum chemical interactions in solids," *Computer Physics Communications*, vol. 185, no. 3, pp. 1007–1018, 2014. [Online]. Available: https://www.sciencedirect.com/science/article/pii/S0010465513003718 [Cited on page 36.]

[62] "Code: Bader charge analysis," https://theory.cm.utexas.edu/henkelman/code/bader/, 2023, acessed: 5.5.2024. [Cited on page 36.]

[63] "Bader charge analysis of nacl," https://ma.issp.u-tokyo.ac.jp/en/app-post/2320, 2020, acessed: 5.5.2024. [Cited on page 36.]

[64] "Quantum espresso, what can QE do," https://www.quantum-espresso.org/what-can-qe-do/, 2022, acessed: 15.01.2024. [Cited on page 37.]

[65] "VASP - Vienna Ab initio Simulation Package," https://www.vasp.at/, 2023, acessed: 15.01.2024. [Cited on page 37.]

[66] "ABINIT," https://www.abinit.org/, 2024, acessed: 15.01.2024. [Cited on page 37.]

[67] E. Artacho, D. Sánchez-Portal, P. Ordejón, A. Garcia, and J. M. Soler, "Linear-scaling ab-initio calculations for large and complex systems," *Physica Status Solidi (b)*, vol. 215, no. 1, pp. 809–817, 1999. [Cited on page 37.]

[68] "Density functional theory software," https://en.wikipedia.org/wiki/Category:Density_functional_theory_software, 2016, acessed: 17.01.2024. [Cited on page 37.]

[69] F. Nogueira, A. Castro, and M. A. Marques, "A tutorial on density functional theory," *A primer in density functional theory*, pp. 218–256, 2003. [Cited on page 37.]

[70] P. E. Blöchl, "Projector augmented-wave method," *Phys. Rev. B*, vol. 50, pp. 17 953–17 979, Dec 1994. [Online]. Available: https://link.aps.org/doi/10.1103/PhysRevB.50.17953 [Cited on page 37.]

[71] F. D. Murnaghan, "The compressibility of media under extreme pressures," *Proceedings of the National Academy of Sciences*, vol. 30, no. 9, pp. 244–247, 1944. [Cited on page 39.]

[72] H. J. Monkhorst and J. D. Pack, "Special points for brillouin-zone integrations," *Phys. Rev. B*, vol. 13, pp. 5188–5192, Jun 1976. [Online]. Available: https://link.aps.org/doi/10.1103/PhysRevB.13.5188 [Cited on page 39.]

[73] J. D. Pack and H. J. Monkhorst, ""special points for brillouin-zone integrations"—a reply," *Phys. Rev. B*, vol. 16, pp. 1748–1749, Aug 1977. [Online]. Available: https://link.aps.org/doi/10.1103/PhysRevB.16.1748 [Cited on page 39.]

[74] Y. Hinuma, G. Pizzi, Y. Kumagai, F. Oba, and I. Tanaka, "Band structure diagram paths based on crystallography," *Computational Materials Science*, vol. 128, pp. 140–184, 2017. [Online]. Available: https://www.sciencedirect.com/science/article/pii/S0927025616305110 [Cited on page 40.]

[75] N. Marzari, D. Vanderbilt, A. De Vita, and M. C. Payne, "Thermal contraction and disordering of the al(110) surface," *Phys. Rev. Lett.*, vol. 82, pp. 3296–3299, Apr 1999. [Online]. Available: https://link.aps.org/doi/10.1103/PhysRevLett.82.3296 [Cited on page 41.]

[76] M. Y. Toriyama, A. M. Ganose, M. Dylla, S. Anand, J. Park, M. K. Brod, J. M. Munro, K. A. Persson, A. Jain, and G. J. Snyder, "How to analyse a density of states," *Materials Today Electronics*, vol. 1, p. 100002, 2022. [Cited on pages ix, 41, and 42.]

[77] P. E. Blöchl, O. Jepsen, and O. K. Andersen, “Improved tetrahedron method for brillouin-zone integrations,” *Physical Review B*, vol. 49, no. 23, p. 16223, 1994. [Cited on page 41.]

[78] M. Probert, “Improved algorithm for geometry optimisation using damped molecular dynamics,” *Journal of Computational Physics*, vol. 191, no. 1, pp. 130–146, 2003. [Online]. Available: https://www.sciencedirect.com/science/article/pii/S0021999103003085 [Cited on page 43.]

[79] H. T. Stokes and D. M. Hatch, “*FINDSYM*: program for identifying the space-group symmetry of a crystal,” *Journal of Applied Crystallography*, vol. 38, no. 1, pp. 237–238, Feb 2005. [Online]. Available: https://doi.org/10.1107/S0021889804031528 [Cited on page 47.]

[80] K. Shah, A. Ćirić, K. Murthy, and B. Chakrabarty, “Investigation of a new way of synthesis for nano crystallites of la2o2s 1%ln3+ (ln= pr, eu, tb, dy, er) doped la2o2s and study their structural and optical properties,” *Journal of Alloys and Compounds*, vol. 851, p. 156725, 2021. [Online]. Available: https://www.sciencedirect.com/science/article/pii/S0925838820330899 [Cited on page 51.]

[81] X.-B. Feng and N. M. Harrison, “Metal-insulator and magnetic transition of nio at high pressures,” *Phys. Rev. B*, vol. 69, p. 035114, Jan 2004. [Online]. Available: https://link.aps.org/doi/10.1103/PhysRevB.69.035114 [Cited on page 53.]

[82] T. Körzdörfer and N. Marom, “Strategy for finding a reliable starting point for g 0 w 0 demonstrated for molecules,” *Physical Review B—Condensed Matter and Materials Physics*, vol. 86, no. 4, p. 041110, 2012. [Cited on page 53.]

[83] M. Cococcioni and N. Marzari, “Energetics and cathode voltages of li m po 4 olivines (m= fe, mn) from extended hubbard functionals,” *Physical Review Materials*, vol. 3, no. 3, p. 033801, 2019. [Cited on page 56.]

[84] A. L. Fetter and J. D. Walecka, *Quantum theory of many-particle systems*. Courier Corporation, 2012. [Cited on page 70.]

A. Coulomb interaction regularization

In the jellium model, due to the long range of the coulomb interaction, the interactions in Eqs.(1.7) and (1.6) fail to converge in the thermodynamic limit L$\rightarrow \infty$. In this chapter we are going to show how these difficulty is solved by cancelling this terms with an equivalent infinity of opposite sign in the electron-electron part of the Hamiltonian. To explicitly show the cancellation of the infinities in $\hat{H}$ we resort to a mathematical procedure known as coulomb interaction regularization. The idea is to replace the coulomb interaction with one with a very long, yet finite range, and to study the system in the limit in which this range is much larger than any other physical length scale except L. A convenient way to show this is by using a Yukawa interaction which has a characteristic range κ^{-1} that by letting $\kappa \rightarrow 0$ after going to the thermodynamic limit $L \rightarrow \infty$ recover the physical Hamiltonian [22]:

$$v(r,\kappa) = e^2 \frac{e^{-\kappa r}}{r} \tag{A.1}$$

We begin by rewriting the interaction potential in the form:

$$v(r,\kappa) = \frac{1}{L^d} \sum_{\mathbf{q}} v_q(\kappa) e^{i\mathbf{q}.\mathbf{r}} \tag{A.2}$$

where:

$$v_q(\kappa) = \int v(r,\kappa) e^{-i\mathbf{q}.\mathbf{r}} d\mathbf{r} \tag{A.3}$$

is the Fourier transform of the interaction potential. Now we can write the electron-electron interaction presented in Eq. (1.5) in the form:

$$\hat{H}_{e-e} = \frac{1}{2} \sum_{i \neq j} \frac{e^2}{|\hat{\mathbf{r}}_i - \hat{\mathbf{r}}_j|} \tag{A.4}$$

$$= \frac{1}{2L^d} \sum_{\mathbf{q}} v_q(\kappa) [\hat{n}_{-\mathbf{q}} \hat{n}_{\mathbf{q}} - \hat{N}] \tag{A.5}$$

where $\hat{n}_{\mathbf{q}}$ is the Fourier transform of the electronic density operator:

$$\hat{n}_{\mathbf{q}} = \sum_{i=1}^{N} e^{-i\mathbf{q}.\hat{\mathbf{r}}_i} \tag{A.6}$$

and $\hat{n}_{\mathbf{q}=0} = \hat{N}$ is just the number operator $\hat{N}$. Now, by rewriting $\hat{H}_{e-b}$ and $\hat{H}_{b-b}$ in terms of $\hat{N}$, we obtain for the complete hamiltonian the follow equation:

$$\begin{aligned} \hat{H} &= \sum_i \frac{\hat{p}_i^2}{2m} + \frac{1}{2L^d}\sum_{\mathbf{q}} v_q(\kappa)[\hat{n}_{-\mathbf{q}}\hat{n}_{\mathbf{q}} - \hat{N}] \\ &- \nu_{\mathbf{q}=0}(\kappa) n_B \hat{N} + \frac{1}{2}\nu_{\mathbf{q}=0}(\kappa) n_B^2 L^d \end{aligned} \tag{A.7}$$

where the last two terms on the right-hand side describe the electron-background and the background–background interactions respectively. We now observe that the $\mathbf{q} = 0$ contribution to the electron-electron part of the hamiltonian is:

$$(\hat{H}_{e-e})_{\mathbf{q}=0} = \frac{\nu_{\mathbf{q}=0}(\kappa)}{2L^d}(\hat{N}^2 - \hat{N}) \tag{A.8}$$

Combining this with the electron-background and background-background terms, and making use of the fact that in the thermodynamic limit $\hat{N} = nL^d = n_B L^d$ we find that:

$$\frac{(\hat{H}_{e-b})_{\mathbf{q}=0} + (\hat{H}_{b-b})_{\mathbf{q}=0} + (\hat{H}_{e-e})_{\mathbf{q}=0}}{L^d} = -\frac{n v_{\mathbf{q}=0}(\kappa)}{2L^d} \tag{A.9}$$

which tends to zero when L tends to infinity for $\kappa > 0$. Thus, in the thermodynamic limit, all the terms that depend on $\nu_{\mathbf{q}=0}(\kappa)$ cancel out. It is only at this point that we are allowed to take the limit $\kappa \to 0$, which is no longer singular, since $\mathbf{q}$ is never equal to zero. The final expression for the regularized jellium hamiltonian is therefore:

$$\hat{H} = \sum_i \frac{\hat{p}_i^2}{2m} + \frac{1}{2L^d}\sum_{\mathbf{q}\neq 0} v_q[\hat{n}_{-\mathbf{q}}\hat{n}_{\mathbf{q}} - \hat{N}] \tag{A.10}$$

where $v_q = lim_{\kappa\to 0} v_q(\kappa)$ is our operational definition of the Fourier transform of the coulomb interaction.

A.1. Construction of the second-quantized hamiltonian

The expression of the electron-background and background-background interaction can also be written as [84]:

$$H_{b-b} = \frac{1}{2}e^2\frac{N^2}{V}\frac{4\pi}{\kappa^2} \tag{A.11}$$

$$H_{e-b} = -e^2\frac{N^2}{V}\frac{4\pi}{\kappa^2} \tag{A.12}$$

By applying the formalism of second quantization to the construction of the jellium model hamiltonina of Eq. (A.10) we got:

$$\hat{H} = -\frac{1}{2}\frac{e^2N^2}{V}\frac{4\pi}{\mu^2} + \sum_{\mathbf{k}\lambda}\frac{\hbar^2k^2}{2m}a^\dagger_{\mathbf{k}\lambda}a_{\mathbf{k}\lambda} + \frac{e^2}{2V} \tag{A.13}$$

$$\times \sum_{\mathbf{k}_1\lambda_1}\sum_{\mathbf{k}_2\lambda_2}\sum_{\mathbf{k}_3\lambda_3}\sum_{\mathbf{k}_4\lambda_4}\delta_{\lambda_1\lambda_3}\delta_{\lambda_2\lambda_4}\lambda_{\mathbf{k}_1+\mathbf{k}_2,\mathbf{k}_3+\mathbf{k}_4} \tag{A.14}$$

$$\times \frac{4\pi}{(\mathbf{k}_1-\mathbf{k}_3)^2+\mu^2}a^\dagger_{\mathbf{k}_1\lambda_1}a^\dagger_{\mathbf{k}_2\lambda_2}a_{\mathbf{k}_4\lambda_4}a_{\mathbf{k}_3\lambda_3} \tag{A.15}$$

where the first term corresponds to the sum of Eq. (A.11) and Eq. (A.12), the second term corresponds to the electronic kinetic-energy operator and the third term to the potential energy. By applying the conservation of momentum to the last term, we can limit the summation over $\{\mathbf{K}_i\}$ to three independent variables. $\mathbf{k}_1 = \mathbf{k}+\mathbf{q}$, $\mathbf{k}_3 = \mathbf{k}$, $\mathbf{k}_2 = \mathbf{p}-\mathbf{q}$ and $\mathbf{k}_4 = \mathbf{p}$ and by evaluating the spin summations using the Kronecker deltas we obtain:

$$\hat{H} = -\frac{1}{2}\frac{e^2N^2}{V}\frac{4\pi}{\mu^2} + \sum_{\mathbf{k}\lambda}\frac{\hbar^2k^2}{2m}a^\dagger_{\mathbf{k}\lambda}a_{\mathbf{k}\lambda} \tag{A.16}$$

$$+ \frac{e^2}{2V}\sum_{\mathbf{kpq}}\sum_{\lambda_1\lambda_2}\frac{4\pi}{q^2+\mu^2}a^\dagger_{\mathbf{k}+\mathbf{q},\lambda_1}a^\dagger_{\mathbf{p}-\mathbf{q},\lambda_2}a_{\mathbf{p}\lambda_2}a_{\mathbf{k}\lambda_1} \tag{A.17}$$

The last term can be separated in two terms, refering to $\mathbf{q} \neq 0$ and $\mathbf{q} = 0$:

$$\tfrac{e^2}{2V}\quad {\sum_{\mathbf{kpq}}}'\sum_{\lambda_1\lambda_2}\frac{4\pi}{q^2+\mu^2}a^\dagger_{\mathbf{k}+\mathbf{q},\lambda_1}a^\dagger_{\mathbf{p}-\mathbf{q},\lambda_2}a_{\mathbf{p}\lambda_2}a_{\mathbf{k}\lambda_1} \tag{A.18}$$

$$+\tfrac{e^2}{2V}\quad \sum_{\mathbf{kp}}\sum_{\lambda_1\lambda_2}\frac{4\pi}{\mu^2}a^\dagger_{\mathbf{k},\lambda_1}a^\dagger_{\mathbf{p}\lambda_2}a_{\mathbf{p}\lambda_2}a_{\mathbf{k}\lambda_1} \tag{A.19}$$

where the prime on the first summation means: omit the term $\mathbf{q} = 0$. The second summation may be written with the anitcomuumation relation as:

$$\frac{e^2}{2V}\frac{4\pi}{\mu^2}\sum_{\mathbf{k}}\sum_{\lambda_1}\sum_{\mathbf{p}\lambda_2}a^\dagger_{\mathbf{k}\lambda_1}a_{\mathbf{k}\lambda_1}(a^\dagger_{\mathbf{p}\lambda_2}a_{\mathbf{p}\lambda_2} - \delta_{\mathbf{kp}}\delta_{\lambda_1\lambda_2}) = \frac{e^2}{2V}\frac{4\pi}{\kappa^2}(\hat{N}^2-\hat{N}) \tag{A.20}$$

And because we are dealing with states of fixed N, the operator $\hat{N}$ may be replaced by its eigenvalue N:

$$\frac{e^2}{2}\frac{N^2}{V}\frac{4\pi}{\kappa^2} - \frac{e^2}{2}\frac{N}{V}\frac{4\pi}{\kappa^3} \tag{A.21}$$

The first term og Eq. (A.21) cancels with the first term of Eq. (A.17). The second term vanish in the limit $L \to \infty$ and $\kappa \to 0$. We therefore obtain the final hamiltonian for a bulk electron gas in a uniform positive background.

$$\hat{H} = \sum_{\mathbf{k},\lambda}\frac{\hbar^2k^2}{2m}a^\dagger_{\mathbf{k}\lambda}a_{\mathbf{k}\lambda} + \frac{e^2}{2V}{\sum_{\mathbf{kpq}}}'\sum_{\lambda_1\lambda_2}\frac{4\pi}{q^2}a^\dagger_{\mathbf{k}-\mathbf{q},\lambda_1}a^\dagger_{\mathbf{p}-\mathbf{q},\lambda_2}a_{\mathbf{p}\lambda_2}a_{\mathbf{k}\lambda_1} \tag{A.22}$$

$$\frac{E}{N} \underset{r_s \to \infty}{=} \frac{e^2}{2a_0}\left[\frac{2.21}{r_s^2} - \frac{0.916}{r_s} + ...\right] \tag{A.23}$$

Note that the energy per particle is finite, which shows that the total energy is an extensive quantity. The first term in Eq. (A.22) is simply the kinetic energy of the Fermi gas of electrons; it becomes the dominant term as $r_s \to 0$, that is, in the limit of very high densities. The second term is known as the exchange energy and is negative. As we have seen, the direct term arises from the $\mathbf{q} = 0$ part of the interaction and serves to cancel $H_{b-b} + H_{e-b}$. This cancellation leads to the restriction $\mathbf{q} \to 0$ and reflects the electrical neutrality of the system. All that remains is the (negative) exchange energy. The remaining terms in this series (indicated by dots) are called the correlation energy.

B. DFT+U calculation using pw.x

```
&CONTROL
calculation = 'scf'
etot_conv_thr = 9.0000000000d-05
forc_conv_thr = 1.0000000000d-04
outdir = './tmp'
prefix = 'C2chu'
pseudo_dir = '/mnt/beegfs/users/mqueiros/workdir/praseodymium'
tprnfor = .true.
tstress = .true.
verbosity = 'high'
/
&SYSTEM
degauss = 0.01
ecutwfc = 116
ecutrho = 696
ibrav = 0
nat = 18
nosym = .false.
nspin = 2
ntyp = 3
occupations = 'smearing'
smearing = 'mv'
starting_magnetization(1) = 5.3846153846d-01
/
&ELECTRONS
conv_thr = 1.8000000000d-8
electron_maxstep = 900
mixing_beta = 0.3
/
&ions
ion_dynamics = 'bfgs'
```

/

&CELL

cell_dynamics='bfgs'

/

ATOMIC_SPECIES

Pr 140.90765 Pr.pbe-spdfn-kjpaw_psl.1.0.0.UPF

O 15.9994 O.pbe-n-kjpaw_psl.1.0.0.UPF

S 32.065 S.pbe-n-kjpaw_psl.1.0.0.UPF

ATOMIC_POSITIONS crystal

Pr 0.3241800000 0.6647800000 0.4164200000

Pr 0.6594000000 0.3352200000 0.0835800000

Pr 0.6758200000 0.3352200000 0.5835800000

Pr 0.3406000000 0.6647800000 0.9164200000

O 0.2324200000 0.4931400000 0.1231400000

O 0.7392800000 0.5068600000 0.3768600000

O 0.7675800000 0.5068600000 0.8768600000

O 0.2607200000 0.4931400000 0.6231400000

O 0.2634400000 0.0023200000 0.3950900000

O 0.2611200000 0.9976800000 0.1049100000

O 0.7365600000 0.9976800000 0.6049100000

O 0.7388800000 0.0023200000 0.8950900000

O 0.7741800000 0.8197000000 0.2062800000

O 0.9544800000 0.1803000000 0.2937200000

O 0.2258200000 0.1803000000 0.7937200000

O 0.0455200000 0.8197000000 0.7062800000

S 0.9427600000 0.0000000000 0.7500000000

S 0.0572400000 -0.0000000000 0.2500000000

K_POINTS automatic

8 8 6 0 0 0

CELL_PARAMETERS angstrom

-0.0000000000 -4.2651711672 -0.0000000000

-6.7392576825 2.1325855836 2.1029457675

0.0000000000 0.0000000000 -8.3044370000

K_POINTS automatic

8 8 6 0 0 0

ATOMIC_SPECIES

Pr 140.90765 Pr.pbe-spdfn-kjpawpsl.1.0.0.UPF

S 32.06500 S.pbe-n-kjpawpsl.1.0.0.UPF

O 15.99940 O.pbe-n-kjpawpsl.1.0.0.UPF

CELL_PARAMETERS angstrom

13.298390393 -4.021019317 -0.015463664

13.298390393 4.021019317 -0.015463664

-4.664264287 0.000000000 14.986363508

ATOMIC_POSITIONS crystal

Pr 0.6626166451 0.6761214521 0.5844699348

Pr 0.3373833549 0.3238785479 0.4155300652

Pr 0.3238785479 0.3373833549 0.9155300652

Pr 0.6761214521 0.6626166451 0.0844699348

S 0.0567257200 0.9432742800 0.7500000000

S 0.9432742800 0.0567257200 0.2500000000

O 0.7385426807 0.7690716073 0.8768191119

O 0.2614573193 0.2309283927 0.1231808881

O 0.2309283927 0.2614573193 0.6231808881

O 0.7690716073 0.7385426807 0.3768191119

O 0.2632003794 0.7348701337 0.6027490305

O 0.7367996206 0.2651298663 0.3972509695

O 0.2651298663 0.7367996206 0.8972509695

O 0.7348701337 0.2632003794 0.1027490305

O 0.9524784280 0.2315472245 0.7949526859

O 0.0475215720 0.7684527755 0.2050473141

O 0.7684527755 0.0475215720 0.7050473141

O 0.2315472245 0.9524784280 0.2949526859

HUBBARD (ortho-atomic)

U Pr-4f 2.1013

C. Birch Murnaghan's equation of state

Important additional structural information can be obtained by studying the variation of the ground-state energy with the volume of the unit cell, whose numerical results can be used to fit an equation of state from which an elastic property, the bulk modulus, B_0, can be derived. We implemented such procedure by varying the lattice parameter in steps of 0.2 Å, in order to obtain the parameters of the following equation of state:

$$E(V) = E_0 + \frac{9V_0B_0}{16}\left\{\left[\left(\frac{V_0}{V}\right)^{2/3} - 1\right]^3 B_0' + \left[\left(\frac{V_0}{V}\right)^{2/3} - 1\right]^2\left[6 - 4\left(\frac{V_0}{V}\right)^{2/3}\right]\right\} \quad \text{(C.1)}$$

$$P(V) = \frac{3B_0}{2}\left[\left(\frac{V_0}{V}\right)^{7/3} - \left(\frac{V_0}{V}\right)^{5/3}\right]\left\{1 + \frac{3}{4}(B_0' - 4)\left[\left(\frac{V_0}{V}\right)^{2/3} - 1\right]\right\} \quad \text{(C.2)}$$

$$B_0 = -V\left(\frac{\partial P}{\partial V}\right)_{P=0} \quad \text{(C.3)}$$

The calculated energies are fitted to the third order Birch-Murnaghan equation of state (EOS EOS) to obtain the pressure–volume relation as shown in Fig. (C.1). The bulk modulus B_0 is calculated using the relation in Eq. (C.1) and compared with available results in the literature [18]. The calculated equilibrium volume and the bulk modulus for tetragonal structure are 134.61 $Å^3$ and 30.5 GPa, respectively. This study can also be made for the monoclinic structure and for Pr_2O_2S, but since it is a time demanding task because of all the calulations needed to be made, it was only possible to do for this structure.

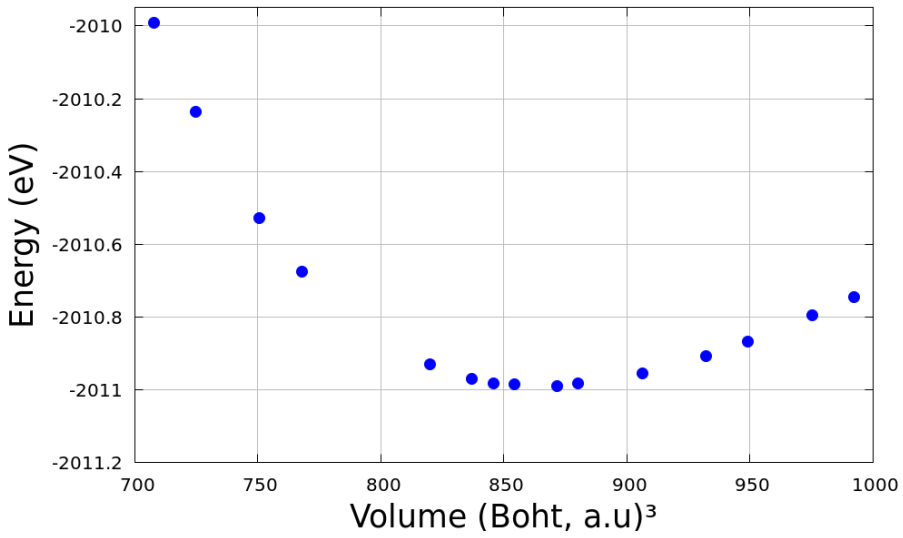

Figure C.1: Relation between the energy of the tetragonal structure, $I\bar{4}2m$ (#121) of $Pr_2O_2SO_4$ and the respective volume obtained using the function ev .x from QE that fits our values to a Birch Murnagham equation of state in order to obtain the volume that minimizes the energy.